Experimental Investigation of the Flow Generated by a Flexible, Flapping Membrane based on a Soft Electromagnetic Actuator

Michael-Anthony Mastroianni

A Thesis

in the Department of

Mechanical, Industrial and Aerospace Engineering

Presented in partial fulfillment of the requirements for the degree

Master's of Applied Sciences (Mechanical Engineering)

Concordia University

Montreal, Quebec, Canada

August 2025

CONCORDIA UNIVERSITY
School of Graduate Studies

This is to certify that the thesis prepared

By: Michael-Anthony Mastroianni

Entitled: Experimental Investigation of the Flow Generated by a Flexible, Flapping Membrane based on a Soft Electromagnetic Actuator

and submitted in partial fulfillment of the requirements for the degree of

Master of Applied Sciences (Mechanical Engineering)

complies with the regulations of the University and meets the accepted standards with respect to originality and quality.

Signed by the final examining committee:

______________________________ Chair
Dr. Jerin John

______________________________ Examiner
Dr. Jerin John

______________________________ Examiner
Dr. Hoi Dick Ng

______________________________ Thesis Supervisor(s)
Dr. Lyes Kadem

______________________________ Thesis Supervisor(s)
Dr. Sampada Bodkhe

Approved by ______________________________
Dr. Lyes Kadem, MASc. Program Director

September 2025 ______________________________
Dr. Mourad Debbabi, Dean
Gina Cody School of Engineering and Computer Science

Abstract

Experimental Investigation of the Flow Generated by a Flexible, Flapping Membrane based on a Soft Electromagnetic Actuator

By Michael-Anthony Mastroianni

Smart actuators combine soft robotic components and stimuli-responsive materials known as smart materials. Smart actuators have innovated fluid pumps and implemented mostly for micro-scale delivery. Fluid pumping at larger scales has been possible due to novel devices such as the CorWave™ heart pump. This device utilizes soft robot elements based on the flapping motion of fish. Aquatic locomotion mechanisms have been well understood via the study of mechanical foils; flow characteristics in their wake are the important link. There remains limited understanding in the wake characteristics generated by the CorWave and flapping foil pumps. We aim in this fundamental study to uncover the flow physics generated by a fully flexible, flapping membrane inspired by the CorWave. We selected a soft electromagnetic actuator (SEMA), enabled by liquid metal, and integrate it in our design inspired from an original prototype. A 2D-DPIV investigation examined the flow generated by the flapping membrane in an open channel flow when placed at the free surface of a quiescent fluid. Velocity, streamwise components and vorticity are extracted from the wake in experiments defined by actuation current, actuation frequency and channel width. A custom fabrication process yields a SEMA membrane with an electrical resistance of $R = 0.248\ \Omega$ and a <10% deviation across all test combinations. The wake's behaviour yields three types of flows classified as: i) propagating, ii) non-propagating and iii) reverse. Their relationship with the actuation frequency and channel width indicated a reverse flow coinciding at $f = 3$ Hz and suggested a flow regime transition at $f = 2$ Hz.

Acknowledgments

The day has finally come. This thesis embodies a workpiece that I look upon with pride but also marks the end of an unforgettable journey. This day conjures up a mixture of emotions: on one hand I am overjoyed to have succeeded even when faced with fear, uncertainty and doubt, but on the other hand I also feel sadness knowing that I will be leaving behind the pond that is grad school and diving into a new one. The journey in my Master's degree has been turbulent: the lows of failed experiments and stagnant progress followed by the highs of discovery and success. My work has constantly adapted and evolved, and like it so have I. As I reflect more on my time here, as I will in 5, 10, 35 years, I will not take with me the negative feelings as those are merely temporary. Instead, I will take the important lessons and fond memories that have shaped me into the person I am. One of these lessons is that your own worst enemy is yourself; you will criticize yourself many times even when others show appreciation. There will be many times where you will be alone working on a composition or calculations, and it is in these moments that you must lift yourself up. I will carry this lesson for the rest of my life and hopefully this message will be useful for future, aspiring researchers. This thesis along with its accomplishments are truly a gift and a gift this special deserves to be shared.

First of all, I would like to thank my supervisor, who likes to be referred to as my advisor, Dr. Lyes Kadem for accepting me as a suitable candidate for this project. Our work together began as early as in my undergraduate studies where I was a research assistant at LCFD. Thank you for your consistent guidance, wisdom and support throughout my work and personal challenges. I will always cherish the passionate discussions about medical innovations where I can hopefully make an impact one day. I would also like to thank my co-supervisor, Dr. Sampada Bodkhe, to whom I thank tremendously for the opportunity to conduct my experiments at Polytechnique Montreal. Your expertise was integral to this project's success. I was one of your first students and our discussions inspired me to be self-sufficient and resourceful. Like Lyes, you have also helped me to overcome my struggles and celebrate the victories. Thank you for giving me that chance. I am also grateful for both yours and Lyes' commitment to fuel the minds of your students. I would also like to acknowledge the great colleagues and friends I made along the way such as Alban Morali, Reza Damansabz, Arijit Mandal, Chethan Girish, Hariharan R, Dr. Giuseppe Di Labbio and Ghassan Maraouch to name a few. It has truly been an honour and a privilege to connect with all of you.

Second of all, I will take this moment to say a few words about those that are not directly related to my work but are the invisible forces at play: my family and loved ones. For my father, Antonio, I cannot thank you enough for teaching me dedication and sacrifice. You have imparted on me your ideas thanks to your engineering background and we have strengthened our bond through our mutual love for science. For my mother, Rosetta, I thank you for teaching me kindness and resilience. You have shown me that a spiritual mind is just as important as an intellectual one and keeping faith in times of uncertainty is crucial to attaining your goals. For my brother, Emmanuel, I thank you for your wisdom and friendship. You are wise beyond your years and you have always been present during times of deep internal conflict. You have lent me your ear and helped me realize my true potential. Last but definitely not least, to my partner Eliana, I thank you for your strength and love. We have both worked together to achieve this goal; this achievement is yours as much as it is mine. I know you have mentioned that it is I who has done the harder part, but your encouragement and support throughout times of hardship is an equally difficult task. You have not only instilled confidence within me but have given your time to ensure my success.

Finally, again to all those mentioned above and others like friends and extended family that unfortunately could not all fit here, I thank you all for believing in me especially at times when I did not believe in myself. I am forever proud of this degree and grateful for the numerous paths it will open for me!

TABLE OF CONTENTS

LIST OF FIGURES

LIST OF TABLES

LIST OF SYMBOLS

E	Young’s modulus [kPa]
γ_{ult}	Ultimate elongation [%]
Γ	Toughness [J/m^3]
U_r	Modulus of resilience [J/m^3]
$\vec{E}$	Electrical field vector
$\vec{B}$	Magnetic field vector
$\vec{I}$	Electrical current vector
$\vec{F}$	Lorentz (i.e. electromagnetic) force vector
Re	Reynold’s number [-]
St	Strouhal’s number [-]
k	Reduced frequency number [-]
vK	von-Karman
rvK	reverse von-Karman
C_T	Thrust coefficient [-]
C_P	Input power coefficient [-]
COT	Cost of transport [J/kg·m]
Fr	Froude number
μ	Surface tension [N/m]
σ	Electrical conductivity [S/m]
B_R	Radial magnetic field strength [mT]
B_Z	Vertical magnetic field strength [mT]

B_Y	Y-component of magnetic field strength [mT]
d	Channel width [mm]
I_{DC}	DC supply current [A]
I_{OUT}	Output current [A]
I	SEMA actuation current [A]
f	SEMA actuation frequency [Hz]
N	Total number of frames
Δt	Time interval between frames [s]
ρ_f	Fluid density [kg/m^3]
ρ_p	Seeding particle density [kg/m^3]
τ_p	Seeding particle response time [s]
τ_s	Characteristic time of flow [s]
St	Stoke’s number [-]
d_p	Seeding particle diameter [m]
μ	Fluid dynamic viscosity [mPa·s]
t_{int}	Time interval in DPIV experiment [s]
$\vec{\omega}_z$	Spanwise vorticity vector [1/s]
$\vec{v}$	Resultant velocity vector [mm/s]
$\vec{u}$	Streamwise (x-component) velocity vector [mm/s]
$\langle\vec{v}\rangle$	Phase-averaged resultant velocity vector [mm/s]
$\overline{\vec{v}}$	Time-averaged resultant velocity vector [mm/s]
$\langle\vec{u}\rangle$	Phase-averaged streamwise velocity vector [mm/s]

$\overline{\vec{u}}_p$	Time-averaged streamwise velocity vector [mm/s]
$\left\|\langle\vec{u}_p\rangle\right\|_{avg}$	Mean magnitude of phase-averaged streamwise velocity vector [mm/s]
$\left\|\overline{\vec{u}}_p\right\|_{avg}$	Mean magnitude of time-averaged streamwise velocity vector [mm/s]
t_{int}	Duration of time interval [s]
t_{end}	Duration of experiment [s]
t^*	Ratio of elapsed time to characteristic time scale (flapping period) [-]
y_s	SEMA flap tip position [mm]

NOMENCLATURE

DOF	Degrees of Freedom
AM	Additive Manufacturing
FDM	Fused Deposition Modelling
DIW	Direct Ink Writing
SLA	Stereolithography
SLS	Selective Laser Sintering
UV	Ultraviolet
SMA	Shape Memory Alloy
SMP	Shape Memory Polymer
DE	Dielectric Elastomer
ME	Magnetic Elastomer
SEMA	Soft Electromagnetic Actuator
LM	Liquid Metal
AC	Alternating Current
LVAD	Left Ventricular Assist Device
HF	Heart Failure
LEV	Leading-Edge Vortices
TEV	Trailing-Edge Vortices
PDMS	Polydimethylsiloxane
PLA	Polylactic Acid
ABS	Acrylonitrile Butadiene Styrene

NdFeB	Neodymium/Neodymium-Iron-Boron
PWM	Pulse Width Modulation
DAQ	Data Acquisition
FFT	Fast-Fourier Transform
DPIV	Digital Particle Image Velocimetry
ROI	Region Of Interest
CMOS	Complementary Metal-Oxide Semiconductor
FOV	Field Of View
PCC	Phantom Camera Control
MOSFET	Metal-Oxide Semiconductor Field-Effect Transistor
GUI	Graphic User Interface
CLAHE	Contrast Limited Adaptive Histogram Equalization
DFT	Discrete Fourier Transform
VDP	Valid Detection Probability

1 INTRODUCTION

1.1 An Overview of Soft Robotics

There have been constant needs to increase autonomy, task complexity and collaboration in the field of robotics. These needs remain challenges for conventional robots due to their inherently low material compliance and limited dexterity. On the other hand, soft robotics rival conventional designs by minimizing the use of interconnected rigid links and joints. Instead, soft robots integrate a soft continuum body that is programmed by external systems responsible for their actuation and sensing. This technology grants soft robots higher degrees of freedom (DOF) and flexibility to achieve precise elastic deformations. The development of soft robotics has led the innovation in many engineering designs by inspiring from or mimicking the functions of biological systems, referred to as bio-inspiration and bio-mimetism respectively. A canonical example of bio-inspiration is a tactile gripper mechanism (Figure 1.1) replicating the movement of invertebrate animals [1]. These design features are in large part due to the presence of compliant materials. Furthermore, their material properties show great compatibility with many fabrication techniques, most notably those based on additive manufacturing (AM) which has been recently popularized. The following section discusses the types of compliant materials and AM processes with their role in soft robotics.

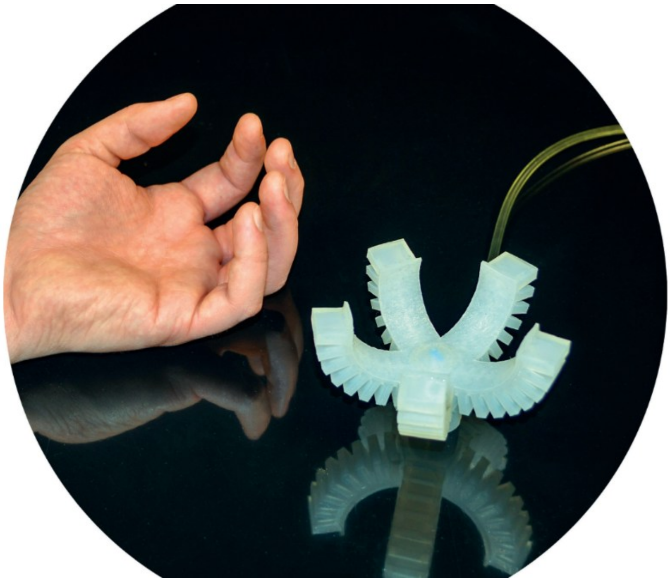

Figure 1.1 Side-by-side illustration of a robotic gripper and human hand. Adapted from [1].

1.2 Additive Manufacturing in Soft Robotics

The most essential material properties that are required for the design of soft robots are low Young's modulus ($E < 10$ MPa) for low resistance to deformation, as well as high ultimate elongation (γ_{ult}), toughness (Γ) and modulus of resilience (U_r) to withstand and restore its structure even at elevated stresses. Polymers such as silicone elastomers, polyurethanes and hydrogels satisfy these requirements. The distinctions of these polymers primarily lie in the composition and density of their crosslinks. The adoption of 3D printing techniques, a class of AM, has permitted low-cost alternatives, fine part resolution and rapid prototyping in soft robotics. 3D printing is a technique that creates 3D objects by the addition of consecutive material layers. The 3D printing technologies utilized in soft robotics are replica moulding, extrusion-based printing such as Fused Deposition Modelling (FDM) and Direct Ink Writing (DIW) and light-based printing such as SLA, SLS and inkjet printing (see Figure 1.2). Of the ones mentioned, the approaches most compatible with the candidate materials are replica moulding and extrusion-based printing. Both these approaches exploit a material's polymerization process. Replica moulding involves liquid-to-solid phase transition of the polymer, where the prepolymer is cast into/onto a thermoplastic, 3D printed mold and cured using heat or UV light. On the other hand, DIW printing methods precisely control the phase transitions so that the polymer can flow through a nozzle, be deposited and quickly solidified upon reaching the target surface [2, 3]. The design for soft robots has also demanded a reduction in size, therefore microfluidic-based techniques such as soft lithography are implemented to create miniaturized devices [4]. Further advancement in soft robotics has moved towards the incorporation of active materials within their design. In this manner, fabrication approaches based on 3D printing have evolved to accommodate multiple materials including active and matrix materials in a continuous process [2]. 3D printing has made a significant contribution to the design considerations involving active materials. These active materials are known as smart materials.

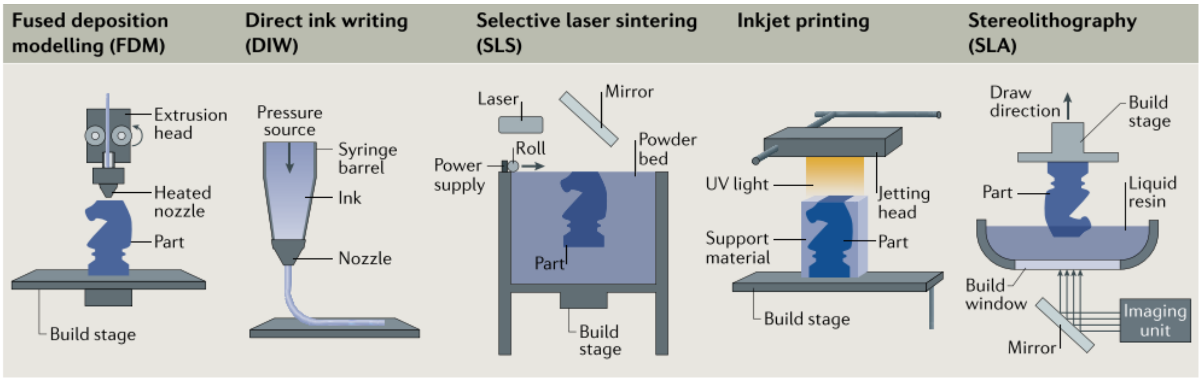

Figure 1.2 Summary of the additive manufacturing techniques for soft robotic designs. Adapted from [2].

1.3 *Smart Materials in Soft Robotics*

Smart materials, sometimes referred to as “intelligent” or “advanced” materials, are generally described as those capable of undergoing reversible modifications and transformations when subjected to various stimuli such as mechanical, chemical, photonic and thermal. They are different than traditional materials in the way that their intrinsic properties grant them responsive behaviour in dynamic, ambient conditions [5]. Smart materials can be combined with non-smart materials (e.g., polymers) to form ‘active’ structures. A smart material serves as the ‘active’ component, while a non-smart material encapsulates the ‘active’ component and functions as the ‘passive’ component.

Smart materials demonstrate capabilities for sensing and actuation by adapting and controlling their behaviour. As mentioned previously, the structural characteristics (low moduli and high deformation strains) of soft robots have made them great hosts for smart materials. They enhance the existing capabilities of soft robots by embedding smart sensors and actuators to provide these intrinsic functions [5]. Combining these elements forms a highly integrated, organized system that resembles closely the hierarchy of biological systems [1]. The tissue layers of the human arm can be used as an analogy to illustrate this point. The muscle tissues represent the limb’s actuators, while skin and nervous tissues represent the compliant material and its internal sensors. Smart material-based soft robots demonstrate the potential to accomplish very complex tasks such as untethered navigation, shape reconfiguration and self-healing [5]. The following discussion explores the current knowledge surrounding smart actuators.

1.4 Smart Actuators

Smart material-based actuators, a subset in the study of soft actuators, convert their input stimulus energy to mechanical energy and exert forces on coupled systems. Their classification is based on their input stimulus. Those primarily reported are shape memory alloy (SMA) and shape memory polymer (SMP)-based actuators responding to temperature, light, moisture, humidity gradients, piezoelectric and DE-based actuators responding to electrical fields and magnetic elastomer (ME)-based actuators responding to magnetic fields (see Figure 1.3). Others, not based on smart materials, include fluidic-based actuators responding to hydraulic or pneumatic pressure gradients. These soft actuators in addition to other examples are presented in Table 1.1. This table is by no means a complete list, rather it summarizes the types of actuators most prevalent in the literature. Electromagnetically responsive actuators are a recent class of smart actuators that has emerged, specifically soft electromagnetic actuators (SEMA)s [6-8]. They are based on a smart material that has received increasing attention in the last few years: liquid metal (LM).

Table 1.1 Examples of smart material-based and fluidic-based actuators classified by their input stimulus. Compiled from review publications [5-12].

Smart Materials					**Other**
Thermally responsive actuators	**Photon responsive actuators**	**Electrically responsive actuators**	**Magnetically responsive actuators**	**Electro-magnetically responsive actuators**	**Fluidic responsive actuators**
• Shape Memory Polymers • Shape Memory Alloys • Liquid Crystal Elastomers	• Liquid Crystal Elastomers	• Piezoelectric • Dielectric Elastomers • Ionic Polymer-Metal Composites	Magnetic Elastomers: • Ferrite/Non-Ferrite particles • Magnetic Rheological Fluids	• SEMAs	• Pneumatic (PneuNets) • Hydraulic

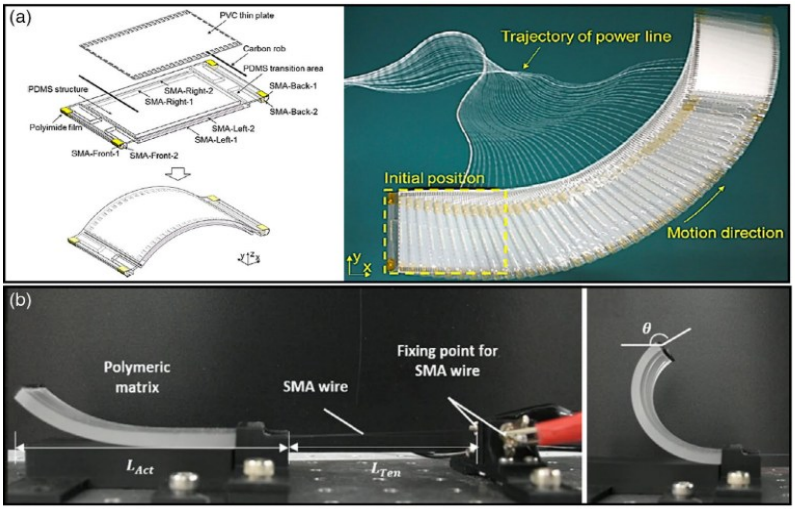

A

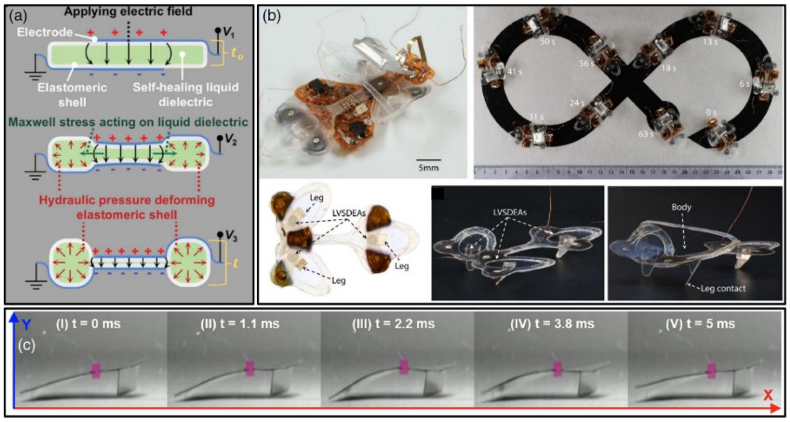

B

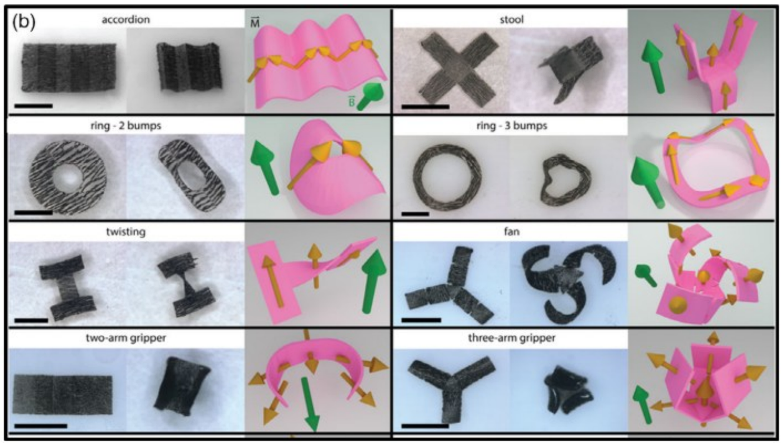

C

Figure 1.3 Applications of A. thermally responsive, B. electrically responsive and C. magnetically responsive actuators. Adapted from [11].

1.5 Liquid Metal-Based Actuators

Modern LMs encompass a set of Gallium (Ga)-based alloys that remain in a stable, liquid state at or near room temperature [13]. This is possible as Ga can be combined with other elements to form a eutectic mixture, effectively lowering its melting point between ~11-26°C [13, 14]. These mixtures exist in many compositions; the most commercially available are those containing Indium (In) and Tin (Sn) such as EGaIn and Galinstan (GaInSn). Ga-based LMs possess the defining traits of both liquids and metals, including high electrical conductivity, high density and low viscosity (~2x that of water). Additionally, their vapor pressure is negligible at ambient conditions making them nontoxic and biocompatible unlike traditional LMs (e.g., Mercury (Hg)). Another unique trait is that it maintains a high surface tension (~10x that of water). This is due to its passivating oxide layer forming a shell around the material when in contact with an oxygen-rich environment. Meanwhile, the resistance of the LM increases as the oxide layer grows to a few nanometers thick. Nevertheless, LM attributes allow easy shape manipulation and strong surface adhesion, facilitating their implementation in engineering designs [13-15]. LMs can respond to various stimuli, such as electricity, magnetism and mechanical stress, allowing multifunctionality. This has been and continues to be explored in research demonstrating its growing potential in many technological areas, some of which include flexible circuitry such as loudspeakers [16], antennas [17] and wireless powering [18], sensors for wearable and implantable health monitoring [19], and finally energy harvesting applications [20-23].

A remarkable function of LM-based devices is their ability to deform in the presence of electromagnetic fields. According to electromagnetic theory, an electromagnetic field is characterized by the superposition of electrical ($\vec{E}$) and magnetic fields ($\vec{B}$) that can exert forces on a moving point charge or charged element. A charged element refers to a current-carrying element ($\vec{I}$) that is subjected to a resultant electromagnetic force ($\vec{F}$), also known as a Lorentz force, which is proportional to $\vec{I}$ and $\vec{B}$ integrated over the element's length [24, 25]. This derivation considers the force contributions solely from $\vec{B}$ as is the case with $\vec{B} \neq 0$ and $\vec{E} = 0$. The solution of Lorentz forces is further simplified in the case of planar and axisymmetric wires of finite length. LM behaves like a wire when patterned into planar, continuous structures. Once a current is applied to the LM wire, it generates its own magnetic field following Ampère's law [26]. The wire's magnetic field and its direction result in its attraction or repulsion to an external magnetic field like two magnets. This interaction results in the device experiencing deformations, those of which can be explained by quantifying Lorentz forces. This is the working principle of SEMAs and is illustrated in Figure 1.4A. Despite them sharing some similarities with MEs with regards to stimulus sources, MEs are clearly distinct in their material components and method of actuation. Magnetic particles are dispersed in a polymer matrix or carrier fluid to fabricate MEs. The embedded particles tend to align their magnetic domains to external magnetic fields. This behaviour induces a magnetic moment, which in turn generates forces, resulting in actuation [8, 12]. Nevertheless, a $\vec{B}$ field source is necessary for both actuators, which can be time-dependent and independent in nature. Electromagnets generate time-dependent magnetic fields which are induced by a flowing current varying with time [8, 12 & references therein]. In contrast, permanent magnets produce constant magnetic fields due to their materials' intrinsic properties [7, 8]. Now that we have contextualized LM-based actuators, we move on to discussing the research on SEMAs.

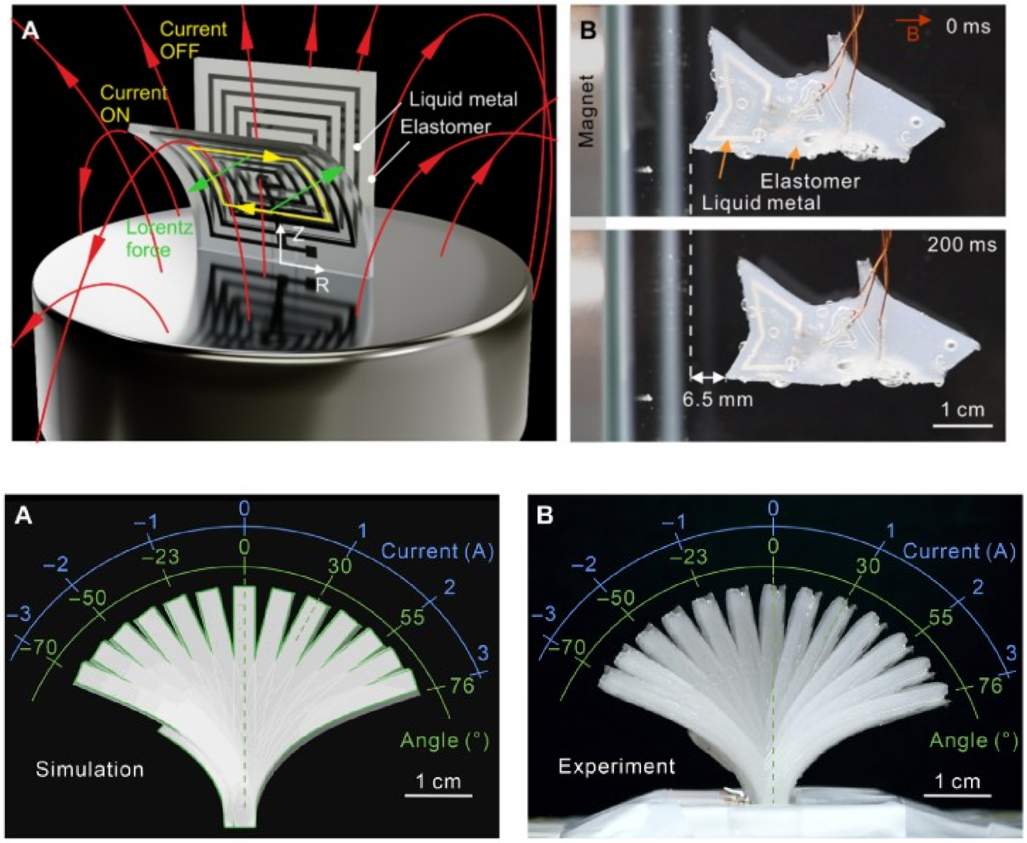

Figure 1.4 Illustration of working principle and achievable deformations for SEMAs. Adapted from [7].

Guo et al. (2018) were the first to propose a soft, electromagnetic actuator enabled by an LM-based coil design. The study discussed its working principle and some mechanical and electrical tests were conducted. Finally, its feasibility was evaluated in many engineering designs. Similarly in 2020, a SEMA prototype was successfully achieved by Mao et al. and reported a complete design. An LM coil pattern is encapsulated in an elastomeric shell (see Figure 1.4). The LM coil was carrying an electrical current supplied by an AC power source while also being subjected to a constant, magnetic field from a permanent magnet. The SEMA's mechanical response was observed in accordance with the AC current signals supplied to it. The prototype was extensively tested for a detailed thermal, electrical and mechanical analysis. This served as a benchmark for devices proposed by [7] and potentially future ones implementing SEMAs. This study was a significant contribution to the research on SEMAs, whereby deformations can be programmed by manipulating Lorentz forces [6, 7].

To summarize *Sections 1.1* and *1.3*, soft actuator designs that draw inspiration from nature and are equipped with smart materials present new approaches to existing solutions and open new avenues for research. Some examples include advancements in industrial automation, terrestrial and aquatic expeditions, human prosthetics and drug delivery [5, 9-11]. Apart from these, soft fluid pumps present a particularly fascinating demonstration of nature's influence in engineering.

1.6 Smart Materials in Fluid Pumps

1.6.1 Principles

There are several examples of nature's evolutionary designs for fluid flow: the jet-based propulsion of jellyfish, a bird's wings generating lift to keep itself hovering in air, an animal's digestive tract and the locomotion of bacteria using its flagellum [27]. Whether it is to transport a body or the fluid surrounding it, there are underlying mechanisms of motion responsible for the flow gradient. Researchers have studied these systems found frequently in nature and have adopted their mechanisms to circumvent the limitations of traditional pumps. The use of traditional designs, such as reciprocating piston-chamber, axial and radial pumps, poses some challenges: high rigidity, larger size and low durability caused by significant friction and wear while in operation. The solution to these design challenges focused on nature's inherently high material compliance and integration of pump components. Consequently, novel devices have been conceptualized and led to the development of partially flexible and fully flexible pumps. These soft pumps are capable of miniaturization, delivering small to large-scale flows using valve-based or valveless designs. As it was mentioned earlier, fluid pumping can be described by the pump's working mechanism. It is also possible to classify fluid pumps according to their principles of motion: positive displacement and fluid dynamics.

1.6.2 Engineering Solutions

Positive displacement pumps are prominent in both nature and engineering; they commonly employ peristaltic and diaphragmatic motion. These mechanisms rely on the elasticity of one or multiple deformable segments to transmit energy into the fluid. Positive displacement pumps generally utilize static fluid forces, whereas fluid dynamic pumps utilize fluid dynamic forces [27]. The integration of smart materials in flexible pumps has shown great potential. Commonly reported smart materials implemented in flexible pumps include SMAs, DEs, Ionic Polymer-Metal Composites (IPMCs) and piezoelectrics which have been formed into sheets, membranes and cantilevers. These designs have been useful in microfluidic, drug delivery, lab-on-a-chip and heart prosthesis applications [28-30]. In addition to the prevalence of peristaltic and diaphragm pumps, their soft-based designs primarily embed smart materials that conform externally to a flexible wall or chamber (see Figure 1.5A). Aside from this, dynamic fluid pumps in engineering are currently implemented as propeller-based designs such as axial and radial pumps. Researchers sought to advance the technology of fluid dynamic pumps by closely matching those in nature, leading their attention to the propulsion of birds and fish. The flapping motion of a bird's wings or fish's tail propels the animal and consequently expels energy into the surrounding fluid. In the case of aquatic species, researchers have discovered that the fish's mechanism for motion shows potential for a novel propeller design. This begs the question: can a soft pump achieve fluid flow with a design based on the flapping motion of a fish's tail?

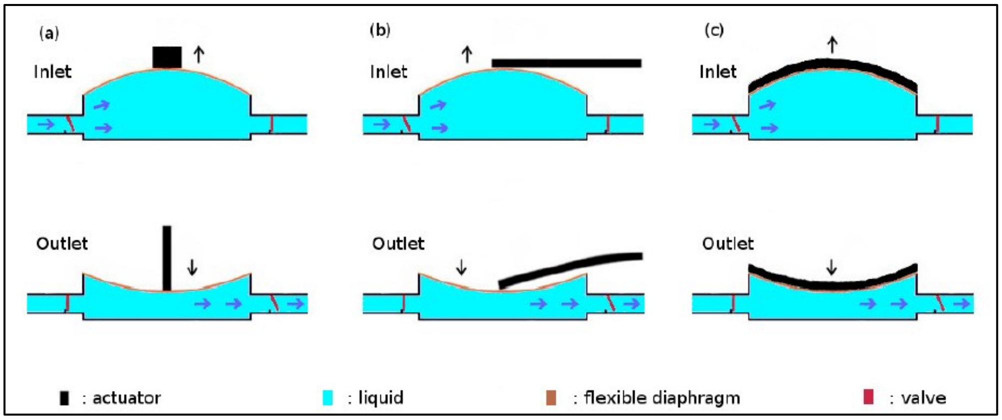

A

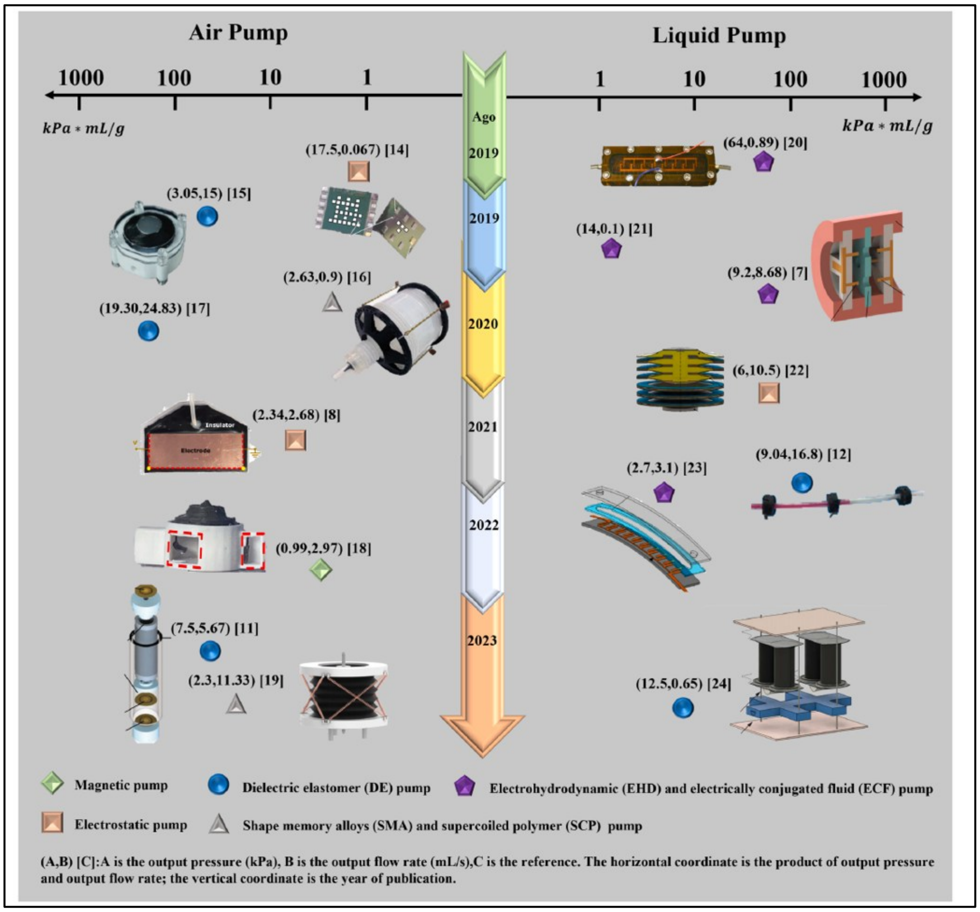

B

Figure 1.5 A. Common designs for pumps implementing diaphragm motion with smart material actuators. Adapted from [29]; B. Overview of the development of smart material-based fluid pumps in recent years. Adapted from [28].

1.7 Smart Material in Fluid Pumps: Applications

This is addressed with CorWave's innovative Left Ventricular Assist Device (LVAD) prototype based on a flapping membrane. An LVAD is an implantable, prosthetic pump used to rehabilitate post-heart failure (HF) patients (see Figure 1.6A) [31]. HF is a cardiovascular disease that arises when heart muscles can no longer reliably deliver blood and oxygen to vital organs in the body [32]. The LVAD is attached to the circulatory system and amplifies the ventricle's flow rate, thereby achieving sufficient cardiac output [33].

The pump actuator's working principle consists of an annular metal ring generating reciprocal motion, once energized by the activation of electromagnets, and then transfers this motion to an annular elastomeric membrane (see Figure 1.6B). This is subsequently stored as elastic energy and transferred to the fluid (in this case blood), where these interactions result in wave-like deformations propagated along the membrane. This pump design is referred to as a 'wave membrane' pump while 'flapping' refers to the periodic, wave-like motion. More specifically, this type of flapping is known as undulation and mimics the locomotory movement of eels and manta rays (see Figure 1.6C) [31]. CorWave claims that this device outperforms previous iterations of LVAD pumps because it minimizes an ongoing disadvantage: high magnitude forces generated from current pump components increase viscous shear stresses which is strongly linked to hemolysis [34]. The device's control system modulates the membrane's undulation frequency to automatically synchronize with the cardiovascular phases. Owing to this feature, CorWave also claims to restore the LV output flow rates to optimal, healthy conditions while minimizing the risk of blood damage [35]. These claims are based on evidence from limited pre-clinical and computational studies, mostly led by the manufacturer, that have evaluated the pump's feasibility and performance [31, 34-37]. CorWave has shown that a pump based on fluid-membrane interactions replicating fish swimming is possible, however there is a limited understanding of the pump's mechanism(s) for flow generation. Therefore, the study of aquatic locomotion remains critical to uncover the fundamental physics governing these mechanisms. This represents the main area of investigation in this thesis.

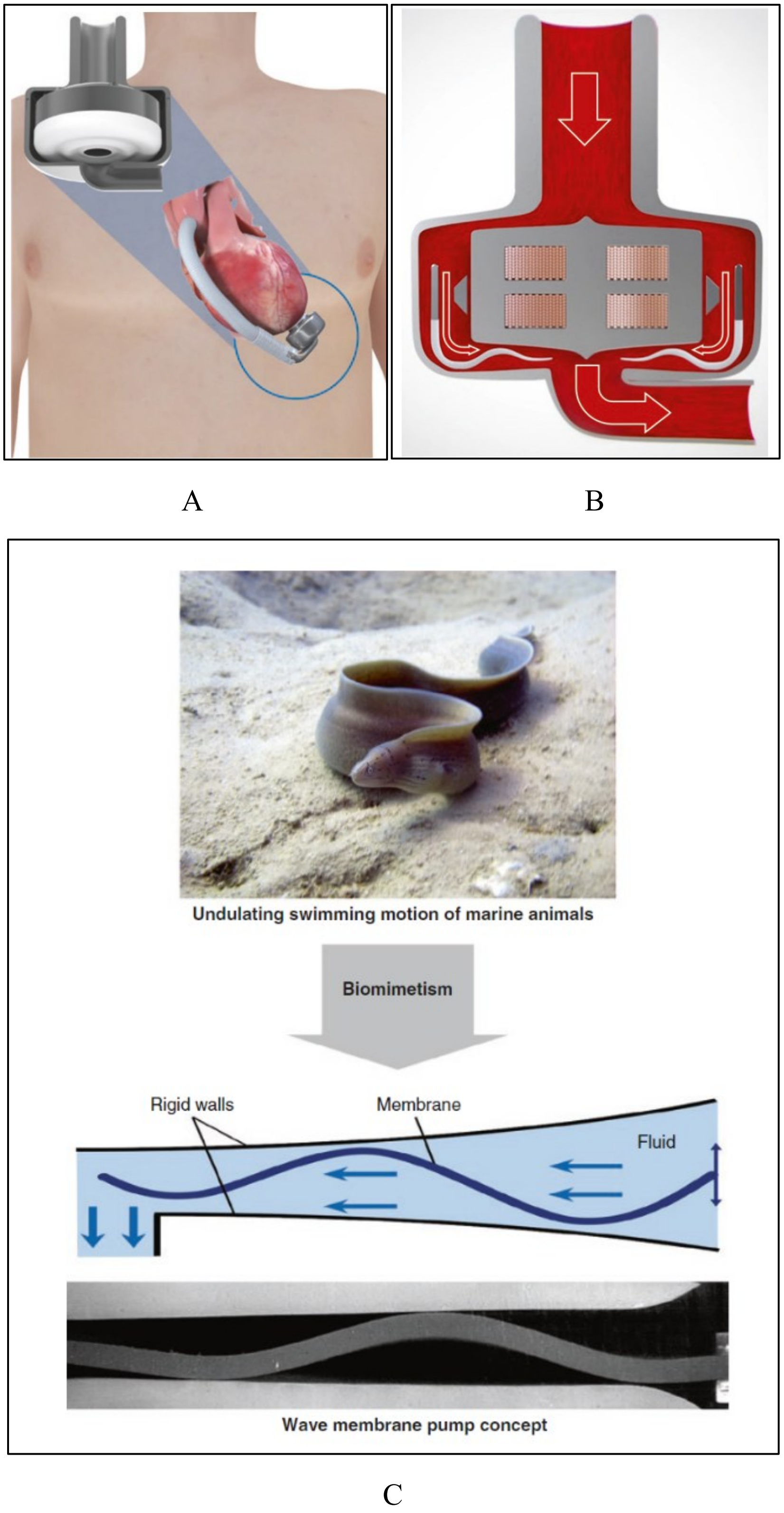

Figure 1.6 A. Schematic of a CorWave LVAD implanted in a human patient. B. The LVAD in operation and the blood flow pathway indicated by arrows. C. Swimming motion of eel and bio-inspired wave membrane design. Adapted from [31].

2 LITERATURE REVIEW

A strong fundamental understanding of the flow induced by flexible flapping membranes necessitates exploring several research topics. We begin here by summarizing the principles and theories of aquatic locomotion that are widely accepted for common species. This is followed by presenting a qualitative overview of swimming kinematics as well as the hydrodynamics and energetics involved in fluid-swimmer interactions. Secondly, we examine those interactions considering mechanical imitations as swimmers and their connections to those in nature. These mechanical imitations are often referred to in literature as flapping foils. Thirdly, the use of smart material (SM)-based and non-SM-based flapping foils in several applications along with critical work on flapping foil-based pumps are discussed. Later, we justify the motivation of this study based on the identified research gaps in flapping foils and smart materials for pumping applications. The CorWave design is then revisited to underline to significance of fundamental studies for flow physics. Lastly, a smart actuator is appropriately selected in order to satisfy the design requirements. The scope and objectives of this thesis are then stated.

2.1 Aquatic Locomotion

A large biodiversity exists in aquatic ecosystems, however most species can be classified according to four primary swimming styles: oscillatory, undulatory, pulsatile and drag-based. Tuna and eels are archetypes of oscillatory and undulatory swimming styles respectively, also called modes. On the other hand, mollusks and ducks are examples of pulsatile and drag swimmers. Oscillatory and undulatory motion are characterized by sinusoidally periodic movements of the animal’s body and appendages about its midline. Pulsatile and drag swimming species exhibit periodic motion based on different physical principles [38]. We therefore restrict the rest of our discussion to oscillation and undulation modes.

2.1.1 Swimming Mechanisms

The diversity in oscillatory and undulatory swimmers is evident in their various body morphologies; as a result pure oscillations, pure undulations or a combination of both motions are produced across different species [38]. These physical attributes alone do not provide a clear distinction between each swimming mode. In fact, early developments in aquatic locomotion kinematics have helped establish a defining criterion for the swimming modes: the ratio of the travelling wave's amplitude along their body length with respect to their body length. Oscillatory species produce large amplitude deformations using their high-aspect-ratio caudal fin which results in a ratio greater than 1. Conversely, undulatory species generate travelling waves at small amplitudes along their elongated bodies resulting in a ratio less than 1. The prescribed motions of these species propel them in a fluid by producing thrust; oscillatory and undulatory motions are referred to as thrust-generating mechanisms. As alluded to earlier, tuna and eels are classified as species displaying pure oscillatory and undulatory motion respectively. Each species can be described according to its associated amplitude ratio and shape profile as shown in Figure 2.1. However, a kinematic analysis alone will not provide a sufficient understanding of aquatic locomotion. Its study is more complex, involving not only the deformations in the body's structure but the deformations in the surrounding fluid as well that change over time.

Let us assume that a fish is freely swimming at constant velocity in a freestream. While the fish is navigating, its movements impart energy into the fluid. The freestream fluid absorbs and then transmits a portion of this energy onto the fish, within which is absorbed and another portion of energy is transferred into the fluid, thereby renewing the cycle. This locomotive condition results in periodic interactions; more specifically periodic exchanges of energy and momentum between the fish's body and surrounding fluid [39]. A fish can actively and passively control the freestream flow by utilizing its inherent flexibility. Muscular activation and coordination influence the energy transferred into the fluid, while body morphology passively directs flow along its curvature [40].

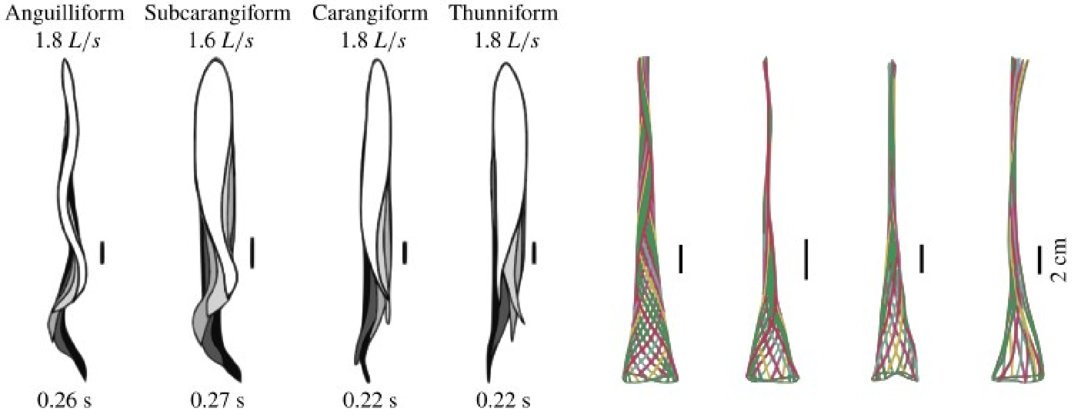

Figure 2.1 The shape and kinematic profiles of undulatory and oscillatory species. Adapted from [38].

2.1.2 Methods of Study

The fish and the surrounding fluid both demonstrate independent motion but significantly influence one another. The underlying physics of their interactions are coupled in order to establish mathematical relations. This is accomplished by combining the principles of fluid and solid body dynamics; this is the central focus of a particular area of study known as fluid-structure interactions. Approaches in this field are used to investigate the energy-momentum exchange at the solid-fluid boundary and the surrounding region in quantitative detail [38, 39]. In the case of aquatic locomotion, some general assumptions of the fluid-structure conditions are described in most studies. The fluid is assumed to be incompressible and Newtonian while the flow is assumed to be inviscid. This greatly simplifies the Navier-Stokes (N.-S.) equations. The fish is assumed to have a homogenous and elastic body that steadily and freely swims, also known as cruising. These simplifications allow the study to ultimately involve the fluid inertial forces, fluid pressure forces and the body's inertial-elastic forces. Researchers employ numerical and experimental methods. Numerical methods consist of developing computational simulations for either exact solutions, through iterations of N.-S. equations, or approximate solutions from derived analytical expressions. In contrast, experimental methods infer data from the interactions by measuring fluid flow characteristics using visualization techniques. These studies are crucial for identifying significant conditions for efficient propulsion in swimming. Such conditions reveal certain patterns that are manifested in many ways, one of which is in the flow downstream from the fish's tail called the wake. Patterns in the wake are particularly important as they are a consequence of swimming behaviour and provide information about the locomotion performance.

2.1.3 Wake Structure

Wake structure is governed by hydrodynamic principles that are characterized by Reynolds number (Re), Strouhal's number (St), reduced frequency (k) and dimensionless amplitude of motion [38]. St and k numbers are similar in such a way that both quantities represent dimensionless frequencies relating the actuation to swimming speed, however their formulations are different. St is dependent on the actuation amplitude, whereas k is dependent on a characteristic length such as the chord to body length. Both parameters are used interchangeably to characterize hydrodynamic frequency, however St is very meaningful in nature. It describes the spatial growth of the wake in relation to the magnitude of the streamwise flow. As the tail-beat amplitude and frequency increase, a threshold is encountered such that the spatial growth is large enough to generate unstable velocity profiles in the wake. At this point, a unique wake pattern is observed and is characterized by a specific arrangement of vortices [41]. This is known as the reverse von-Karman (rvK) vortex street. Two counter-rotating vortices are shed per cycle symmetrically about the body's midline, unlike the von-Karman (vK) vortex street that is well documented in classical FSI studies. This arrangement is clearly visible in a 2D cross-sectional view as the fish's wake is highly 3-dimensional [38] (see Figure 2.2). The rvK street also coincided with a specific range of St values: $0.25 < St < 0.35$. In this range, an energetically favourable condition for swimming was discovered and yielded high propulsive efficiency. These findings implied the existence of hydrodynamic characteristics in the wake that are associated with efficient propulsion [42]. This was supported by evidence in later studies. Drucker et al. (2001) also observed the rvK street and reported a 2S wake structure in some conditions for oscillatory species, whereas Tytell et al. (2004) observed only a 2P wake structure for an eel swimming. A 2S wake structure refers to two vortices shed in a cycle, meanwhile 2P refers to two pairs of vortices in a cycle. These differences can be attributed to the thrust-generating mechanisms as discussed earlier. In the case of undulatory swimmers, the wake vortices are organized in such a way that they are correlated with the pressure gradients along the body's travelling wave segments.

2.1.4 Measures of Performance

The swimming performance can indeed be quantified apart from qualitative assessments of performance from patterns in the wake. For a steady swimmer, the force contributions of thrust must balance the force contributions of drag for efficient locomotion [38]. The measurement of this efficiency is based on certain criteria, most notably the thrust coefficient (C_T), input power coefficient (C_P) and the cost of transport (CoT). CoT is the ratio of the thrust to input power coefficient and its value represents the swimmer's propulsive efficiency. Drag contributions are often difficult to measure experimentally and numerically due to the strong FSI coupling, therefore it is sometimes estimated from the offset of experimental C_P compared to inviscid flow theory (i.e., negligible fluid frictional forces). The thrust-generating mechanisms discussed in *Section 2.1.1* specifically produce thrust by overcoming the fluid's added-mass forces, which are the added inertia exerted on the fish's body due to the surrounding fluid displacing with it.

We now turn to the development of bio-inspired, mechanical models of undulatory/oscillatory species and how their fluid-structure interactions reflect the characteristics of nature.

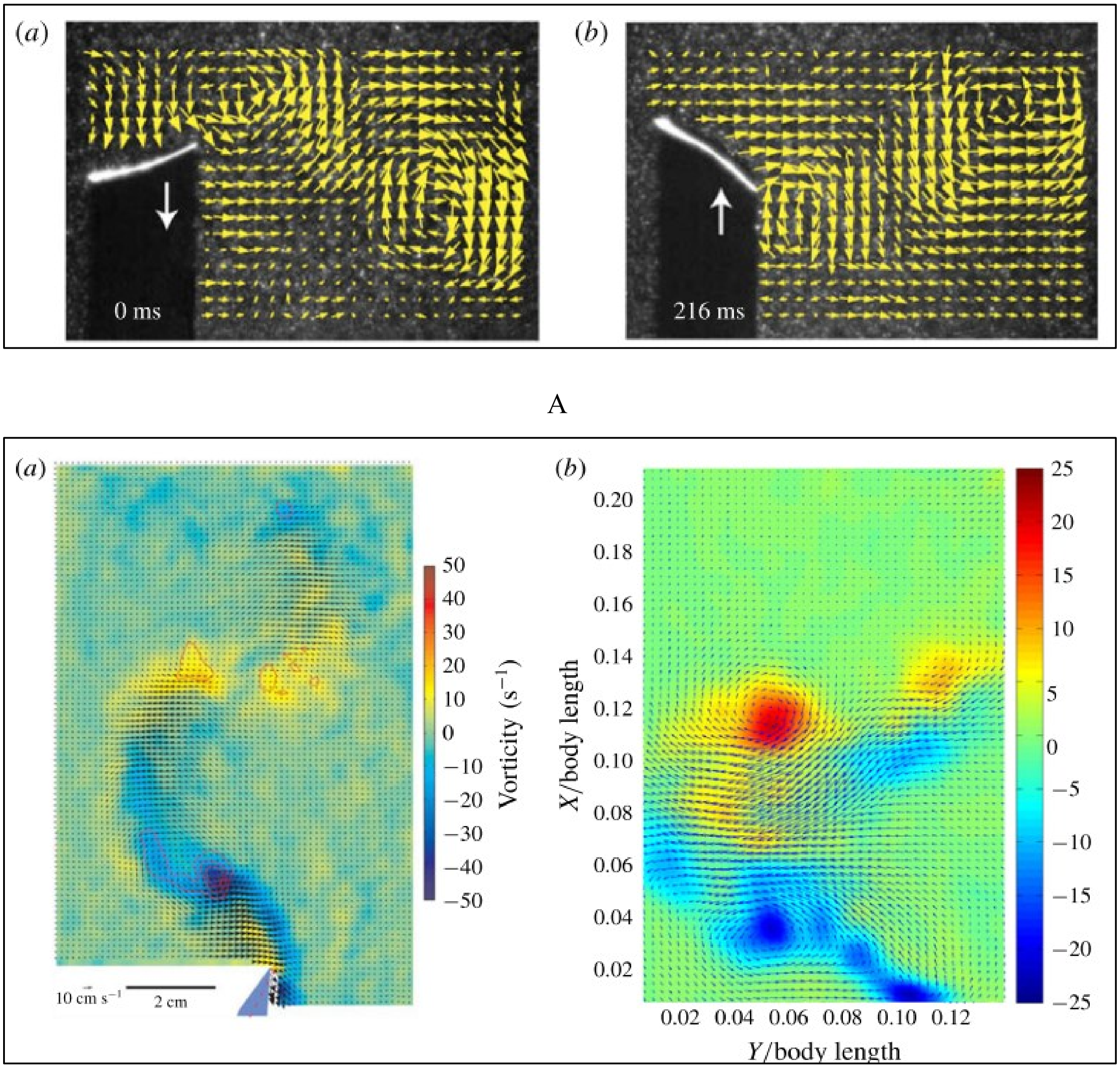

Figure 2.2 Wake structures observed in A. an oscillatory swimmer and B. an undulatory swimmer. Adapted from [38].

2.2 *Foils: Imitation of Swimmers*

Researchers have focused on simplified models to imitate the body structure and thrust-generating mechanisms of fish. In doing so, they have isolated the caudal fin or elongated body-fin to conceptualize a propulsor [38]. Their designs are based on rigid, mechanical components featuring simple geometries to facilitate computational and experimental studies and simulations, and can be modified for parametric studies. The implemented designs that are the most documented are streamlined foils as their geometric features closely resemble that of a fish's aft body (see Figure 2.3). Other designs are modelled as finite plates, panels and membranes where these terms are sometimes used interchangeably. These designs are prescribed motion, either in simulation or in experiment using stepper motors, and perform actuation.

2.2.1 Modelling of Propulsors

In the case of experimental fluid-structure interactions, the conditions in foils and fish are fundamentally different as foils actuate about an anchored point. This results in kinematically constrained motion that is either towed or tethered by a stepper motor shaft, unlike in natural free swimming. In this manner, the models are kinematically constrained unlike in natural free swimming. More specifically, fluctuations in pressure and velocity in the flow are absent, but these characteristics have negligible effects on the swimmer's performance and wake structure [43]. Foils in experimental studies are conventionally fixed and actuated about their span axis, where the flow measurements are performed in a 2D view parallel to their chord length.

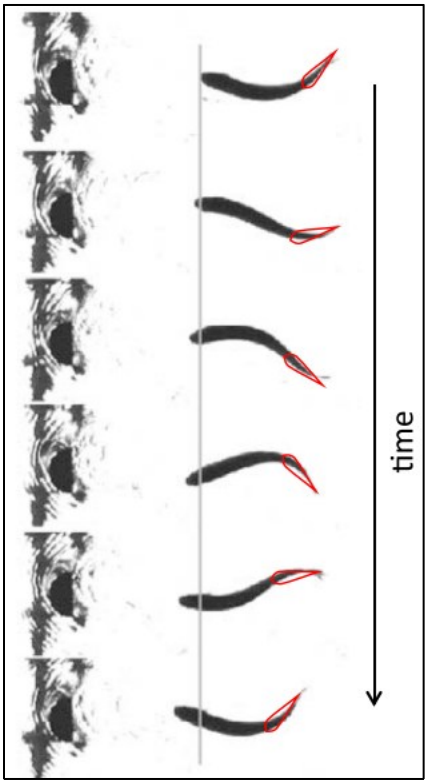

Figure 2.3 Imitation of a fish's aft body with a streamline foil. Adapted from [44].

2.2.2 Thrust-Generating Mechanisms

Foils are prescribed periodic, sinusoidal motion symmetric about their chord length which imitates the kinematics of aquatic locomotion. Additionally, thrust production in foils is classified according to their thrust-generating mechanisms which have been reported as pitching, heaving and flapping, which is a combination of both pitching and heaving (see Figure 2.4). Flapping motion, by definition, is more closely related to oscillatory swimming; some studies represent this term to describe both oscillatory and undulatory motion [44]. We acknowledge these efforts but, like in [44], we will explicitly refer to flapping and oscillatory motions as equivalents. Mechanisms employed by foils generate distinct forces, where pitching motion is predominantly characterized by streamwise forces and heave motion by transverse lift forces [38, 44]. After reviewing the thrust-generating mechanisms of foils, the following discussion focuses on their resulting wake characteristics.

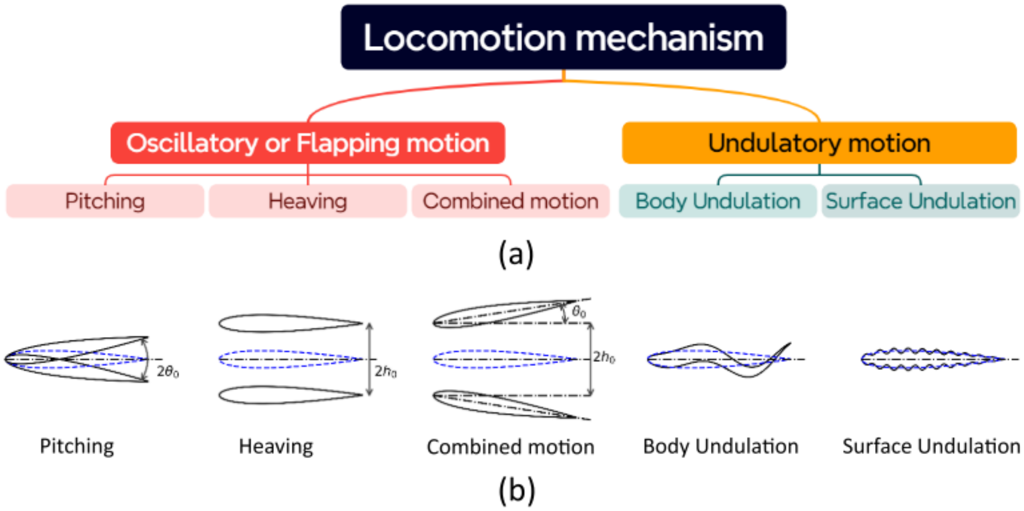

Figure 2.4 Classification of thrust-generating mechanisms in foils. Adapted from [44].

2.2.3 Pitching Foils

Pioneering studies have investigated the sinusoidal pitching of a rigid airfoil and the effects of pitching frequency, amplitude and waveform and on the vortical patterns in the wake. Koochesfahani et al. (1989) reported that the most important parameter that dictates the wake pattern is k, resembling drag-producing (vK) and thrust-producing (rvK) wakes at specific k values. It was also found that the corresponding wake velocity profiles increase in magnitude linearly with pitching frequency and amplitude. Triantafyllou et al. (1993) later supported the emergence of these wake patterns and went further to uncover conditions of peak efficiency. As stated in the beginning of *Section 2.2,* vital connections in the foil wake patterns and efficiency to those in aquatic locomotion were made. The St values at peak foil efficiency coincided with those for peak swimming efficiency, while the associated vortex arrangement was reminiscent of fish producing thrust. The time-averaged wake profile in this regime was described as an axial jet. These studies put forth the widely accepted hypothesis that a thrust-generating wake is associated with high propulsive efficiency. Researchers focused on the wake patterns of pitching foils to categorize them in distinct flow regimes (see Figure 2.5). It was found that when increasing the pitching frequency, a critical point was reached where the drag-producing wake transitions to one that is thrust-producing. This transition in the wake types was associated with the vK to rvK transition but they both do not occur simultaneously [45, 46]. In fact, there existed various other wake patterns corresponding to a dimensionless amplitude and St number. A certain $St-$A combination in the vicinity of $St \geq 0.4$ would yield an asymmetric wake, sometimes referred to as deflected wake, in the rvK regime [47]. Godoy-Diana et al. (2009) had investigated this phenomenon in greater detail. They theorized that the onset of wake deflection is caused by a dipole pair of counter-rotating vortices convecting at a velocity large enough to separate from the existing vortex street, leading to symmetry breaking.

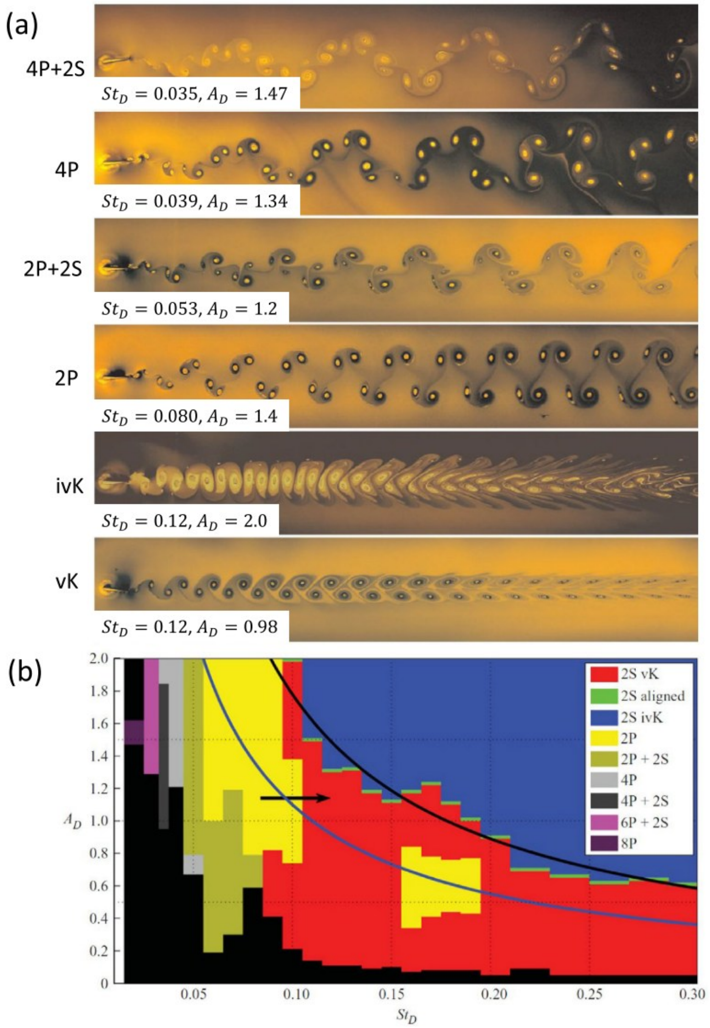

Figure 2.5 Wake structures observed in pitching foils by Schnapper et al. (2019). Adapted from [44].

2.2.4 *Heaving Foils*

Vortical patterns have been correlated to drag, neutral and thrust wakes in heaving similar to pitching foils. In the case of heaving foils, a dimensionless heave velocity, related to heave frequency and amplitude, is the defining parameter influencing the patterns in the wake [48]. An increase in its propulsive efficiency was found to be caused by an increasing heaving frequency at constant St number [49]. Andersen et al. (2017) conducted numerical simulations to qualitatively compare wake patterns in pure pitching and heaving airfoils using a unified St-A map (see Figure 2.6). Distinctions in the wake patterns for heaving foils were evident; the drag-thrust transition progresses from $vK \rightarrow 2P \rightarrow rvK$ wake regimes. Additionally, other vortex structures such as $2P + 2S$, referring to two pairs and oppositely-signed vortices, and deflected wakes are observed in both pitching and heaving foils at sufficiently high St numbers. Whereas at lower St numbers, wake profiles in heave resemble dual symmetric jets about the foil's chord. The reported wake profiles in pitching foils are characterized by a single, centered jet as in [42].

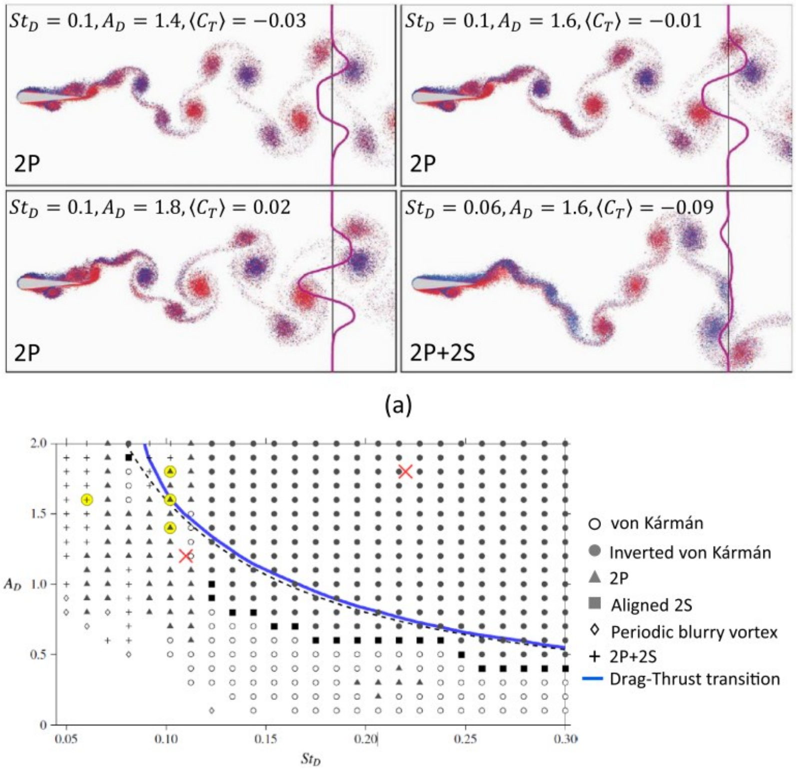

(a)

(b)

Figure 2.6 Wake structures and associated velocity profiles in heaving foils observed by Andersen et al. (2017). Adapted from [44].

2.2.5 Flapping Foils

Flapping motion combines both pitching and heaving motions where each of their contributions, either active or passive, affects the wake characteristics. Anderson et al. (1998) explored the case of an actively flapping airfoil, classifying the kinematic parameters in terms of wake regimes. Both prescribed heaving and pitching motions are sinusoidal, therefore a sufficient phase difference was identified and yielded optimal efficiency. At this same limit, wake patterns corresponded to the most favourable arrangement of leading-edge vortices (LEVs) and trailing-edge vortices (TEVs). Later experimental work by Letink et al. (2008) reported wake structures that deviated slightly from those observed in pure pitch and pure heave called *wavy vK* (see Figure 2.7). Recently, Verma et al. (2022) performed numerical simulations to study the effects of varying heave and pitching contributions on the resulting wake structures. One of the main findings was the emergence of bifurcations in the vortex street when the flapping foil's motion transitions from one dominated by pitch to heave. Analytical investigations of performance by Buren et al. (2018a) deduced that a foil incorporating a heave component will significantly enhance its efficiency in comparison to a pure pitching foil.

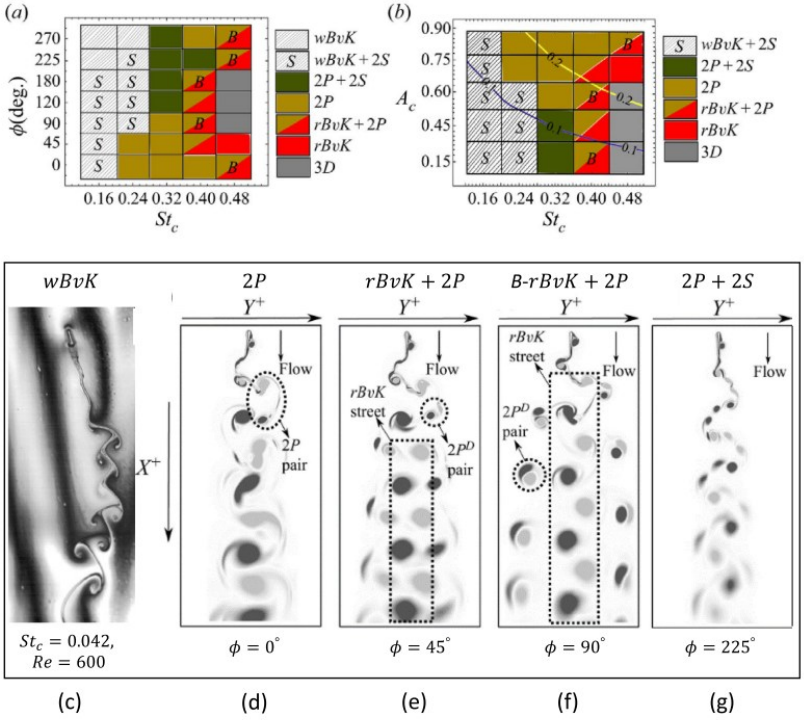

Figure 2.7 Classification of wake structures in combined-motion (flapping) foils by Letink et al. (2008). Adapted from [44].

2.2.6 Undulating Foils

Gupta et al. (2021) have identified eight different wake patterns, all of which capture the drag wakes, drag-thrust transition, thrust and deflected wakes resembling those in pitching foils. However, the deflected wake regime yields the highest propulsive efficiency in the case of undulatory foils. Although the vortex patterns are similar pitching foils, the formation and convection of the vortices are fundamentally different [44] (see Figure 2.8). This has been investigated by Thekkethil et al. (2018), where they organized a study analyzing the evolution of vortices in the vicinity of the foil's trailing edge in an undulatory and pitching foil. The convective direction of the wake in undulatory motion is aligned with the foil's centerline, whereas the vortices convect at an angle to the foil's centerline in pitching motion. In this manner, the spatial distribution of vortices is significantly larger for a pitching foil. The group also concluded the presence of secondary vortices in undulatory motion along the body's travelling waves as it has been reported in [38].

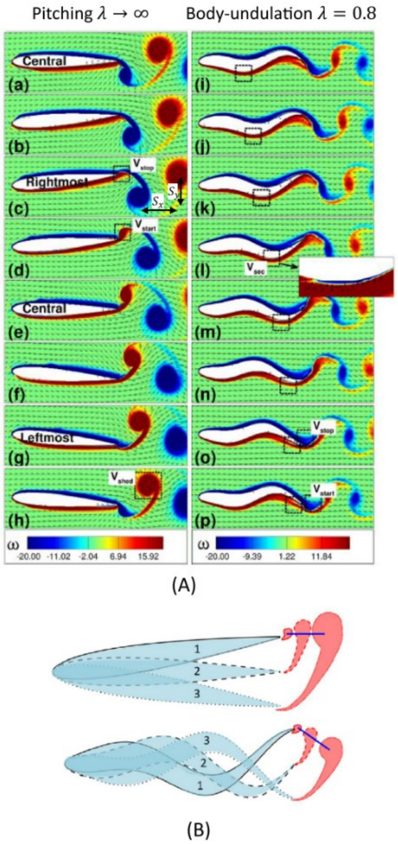

Figure 2.8 The effects of undulatory motion as opposed to pitching motion on the wake vortices as reported by Thekkethil et al. (2018). Adapted from [44].

It is evident that the thrust-generating mechanisms of foils have a profound impact on the wake characteristics. Additionally, there are other factors influencing patterns in the wake such as structural flexibility, freestream flow and environmental boundaries. This is the subject of the following discussion.

2.3 *Role of Flexibility*

Flapping foils can be constructed with elastic materials modifying them to be fully or partially flexible; this grants them passive flexibility about their chord length. Flexibility in flapping foils leads to different results in terms of propulsive efficiency and wake structure compared to their rigid counterparts. The FSI framework changes as well since not only the foil's actuation but the fluid forces also determine the foil's structural response [38]. A fundamental study by Marais et al. (2012) observed that a fully flexible foil inhibits the asymmetry that would be present for a rigid foil and stabilizes the wake for a wider range of St numbers (see Figure 2.9). Furthermore, performance metrics estimated from velocity field data demonstrate that a flexible foil generates nearly 3x as much thrust than a rigid foil. Dewey et al. (2013) and Quinn et al. (2015) extended this work through analytical studies relating the thrust production to structural frequencies. Both studies agreed that optimal conditions coincide yet again in the efficient St range and when the foil is operating at or near its natural frequencies. Researchers can exploit the foil's harmonics for establishing various optimal states, such is shown in [50] for heaving foils. Multiple peak efficiencies have also been reported for flexible, pitching foils as well, where David et al. (2017) reported two peak efficiencies which were characterized by the mode shape, k and a dimensionless rigidity parameter R^*, relating structural rigidity to added-mass forces.

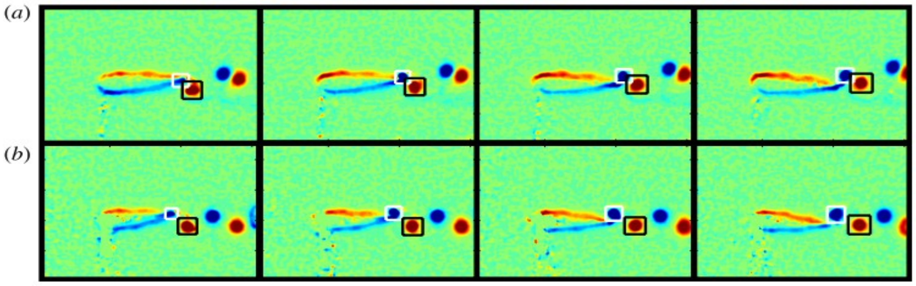

Figure 2.9 The stabilization of the wake vortices for the b) flexible foil unlike the a) rigid foil. Adapted from [51].

2.3.1 *Role of Freestream Conditions*

All the flapping foil studies described above were conducted in a fluid with a constant freestream velocity. Some studies examined cases in the absence of a freestream and the foil is actuated in a quiescent (i.e., still) fluid. This corresponds to a singularity where the FSI is highly unsteady; the momentum and energy in the wake are generated solely by the flapping foil. This is further characterized by $Re \rightarrow 0$ and $St \rightarrow \infty$, which in theory means that the wake growth is tending towards immeasurable instability. Nevertheless, key findings from Heathcote et al. (2007) for a rigid heaving foil and Arakeri et al. (2013) for a rigid pitching foil report interesting observations. A meandering jet in the wake is present, where the wake deflections are either quasi-periodic or random. Jet meandering has been completely suppressed with a flexible foil tuned to a narrow range of dimensionless rigidity values and resulted in a coherent, axial jet as reported in [52] (see Figure 2.10). This inspired later studies to examine the effects of kinematics [53], hydrodynamics and energetics [54, 55] in the wake characteristics in a quiescent fluid. Specifically in the works of Shinde et al., detailed investigations of the momentum and energy additions during the foil's flapping cycle demonstrate that their waveforms coincide well with the phases in the flapping cycle. Thrust production was achieved in certain kinematic conditions which is explained by the favourable direction of the pressure gradients due to the flexible flap deformations. This shows evidence that the thrust generation in a quiescent fluid is solely achieved by a periodically pitching foil.

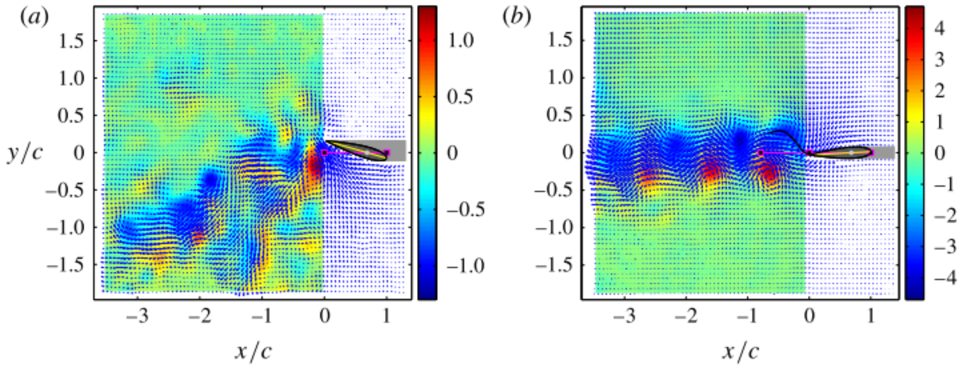

Figure 2.10 The stabilization and centering of the time-averaged wake in a quiescent fluid for the b) flexible foil unlike the a) rigid foil. Adapted from [52].

2.3.2 Role of Boundary Interactions

A foil's performance and characteristics in its wake are also influenced by interactions with a boundary, whether that would be a wall, ground or free surface. Quinn et al. (2014) had numerically investigated a solid boundary's effect on a pitching airfoil by varying their distance between each other. The propulsive efficiency, vorticity and time-averaged wakes were measured, and interesting behaviour occurred at a distance close enough to the boundary region. It was found that transverse lift forces were significantly large in this condition that either pulled or pushed the foil in relation to the boundary; the behaviour depended on the resultant direction of the lift forces. In either scenario, the wake patterns were modified, and overall thrust was reduced. In the case where the foil is sufficiently close to the boundary, the wake vortices will collide with it and alter their trajectory (see Figure 2.11). The time-averaged wake will demonstrate a jet that is deflected away from the boundary. A foil operating near a free surface also exhibits similar behaviours, whereby a sufficient distance from a free surface will induce a 'virtual' solid boundary effect. In this manner, the wake energy propagated to the free surface is not large enough to overcome the fluid's surface tension, therefore it can either be deflected downstream or converted into weak surface waves. As the foil approaches the free surface, wake patterns are increasingly chaotic. Significantly high energy is propagated downstream and the free surface in the form of strong wave deformations. The stability in the free surface is often characterized by the Froude number (Fr). [56-58]

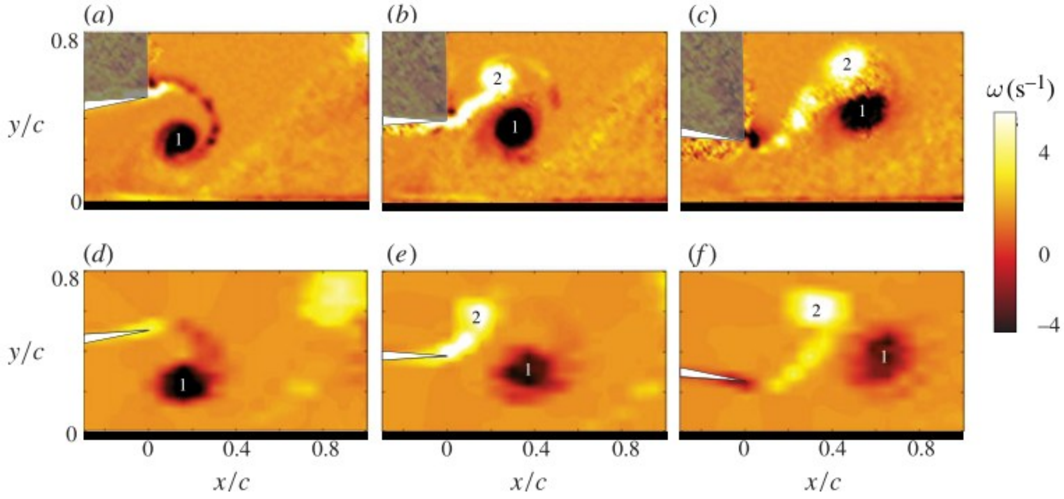

Figure 2.11 The wake dynamics of a flapping foil in the vicinity of a solid boundary. Adapted from [59].

2.4 Applications of Flapping Foils

2.4.1 Energy Harvesting and Biomimetic Fish

A widely used application for flapping foils is energy harvesting, whereby the foil is either submerged or placed at the free surface harnessing the energy from the freestream flow. Once again, flexibility is utilized to achieve passive pitching and/or heaving which dramatically affects the harvesting efficiency [60]. An experimental study by Su et al. (2019) observed the effects of solid boundary confinement (i.e., walls) on the harvesting efficiency of a pitching foil. It was found that for varying pitching frequency and amplitudes, a heave component and confinement achieved efficiencies close to 50%. An example of implementing a flapping foil in cardiovascular research is the design of a cantilever resonator by Secord et al. (2019), who numerically investigate its efficiency in extracting energy from cardiac motion to supply pacemakers. As mentioned earlier in Section 2.1, flapping foils are models for isolated propulsors that can be implemented for novel underwater vehicles and biomimetic fish designs. Biomimetic fish tails employ either rigid or flexible foils and other elastic components to enable tuned flexibility which is observed in natural fish [61]. Biomimetic soft robots have undeniably incorporated smart materials in their designs, such as electromagnetic and piezoelectric responsive actuators [62, 63].

2.4.2 Fluid Pumps

Flapping foils implemented as fluid pumps would be considered valveless designs according to the principles highlighted in *Section 1.7*. The studies that were reviewed earlier primarily focus on the fundamental interactions with the surrounding fluid; they do not explore its potential as a fluid pump. Some studies do however and by this notion we revisit the CorWave’s wave membrane. The recent numerical studies by Martinolli et al. pertain to the optimization of the FSI while facing challenges in boundary contact. These studies assess the optimization techniques by evaluating the criteria measuring pump performance such as output flow rate and pressure. Reviews by Botterbusch et al. also comment on the pump’s performance, feasibility and working principles. These studies briefly report the velocity fields in numerical simulations but do not elaborate on the wake structures. In the case of smart materials, De Lima et al. had developed a piezoelectric-based pump and reported the pump’s performance. They had also reported velocity fields at a given excitation voltage and frequency, but like others did not discuss wake dynamics. On the other hand, an electromagnetic responsive actuator was used in an actuating joint in water to observe the symmetry-breaking mechanisms in the flow [64]. Vorticity and velocity distribution were reported and demonstrated the onset of symmetry breaking in the flow; viscous energy dissipation was measured as well to extract information on the joint's propulsive performance. The wake dynamics for a smart material-based actuator are reported, however the study is focused more on the joint's dynamics rather than its effect on the flow.

2.5 Motivation

2.5.1 Research Gaps

It is apparent that there is a lack of knowledge surrounding the fundamental flow physics of a smart material-based actuator and its capability to generate flow. This knowledge is indeed significant as soft robot designs are increasingly present in cardiovascular research, where their implementation shows great potential for compatibility and long durability as is seen in the CorWave. We have seen that smart materials such as electromagnetic and piezoelectric actuators are used to operate fluid pumps, however flapping foil designs utilizing them are scarce. There is indeed a gap in the research for smart material actuators and fluid pumps, specifically investigating the flow generated from an actuator. Accomplishing this would contribute to a better understanding of flapping foil-based pumps, like the CorWave, as the flow information may indicate interesting patterns. In this manner, we inspire ourselves from the CorWave to develop a similar prototype for this experimental study. We utilize the already established flow visualization techniques for experimental fluid-structure interactions to quantify the flow in the wake. Our selection for the actuator prototype is important, where we are left with two suitable options: a piezoelectric-based actuator or a SEMA actuator. We select a SEMA for our study, but why a SEMA?

2.5.2 Selection of Smart Actuator

The selection for a smart actuator depends ultimately on the application, where in this case deformation magnitude and actuation power are the defining criteria. Piezoelectric actuators provide good frequency bandwidth (~kHz) and good deformation (~220 – 2500 μm) [65], however they require elevated actuation voltages (~kV). This presents major challenges in using additive manufacturing-friendly materials as this voltage level can cause dielectric breakdown, rendering very limited usability [5, 66]. In the case of a SEMA a lower frequency bandwidth (~Hz) but higher deformation range (~cm) [7] is achievable, however it does require actuation currents in the order of Amps (~A). This would require efficient cooling as considerable heat would dissipate from electrical components, therefore its design is sometimes not feasible for certain applications. Despite the advantages of piezoelectric actuators, actuation requirements would necessitate more costly electrical equipment whereas SEMAs can operate using commercially available power supplies. SEMAs are also very compatible with many additive manufacturing techniques. 3D printing can be combined with soft lithography techniques to pattern liquid metal in flexible substrates.

2.5.3 Thesis Objectives

In this study, we aim to:

1. Bridge the concepts of flapping foil pumps and smart material-based actuators by conceiving a smart material-based membrane design inspired from that of the CorWave's LVAD.
2. Replicate a reliable and robust SEMA based on an original prototype's design [7] by implementing a custom fabrication process aided soft lithography and additive manufacturing techniques.
3. Create a 'SEMA membrane' prototype and implement it in a fluid environment to qualitatively examine the flow characteristics generated in the wake, using a flow visualization technique, and connect it to those of flapping foils.

3 METHODOLOGY

In this section, we begin with a discussion on the SEMA pump membrane that focuses on the important aspects and components of its design. This is then followed by the proposed fabrication process. Next, the experimental setup is described and highlights the main assemblies. Validation tests are performed on the assemblies responsible for programming the SEMA to ensure proper implementation. The input variables are then clearly defined and represent the experimental parameters for the complete system. We then continue our discussion on the assembly which is manufactured for flow visualization. The principles and workflow of this assembly are reviewed based on the selected flow visualization technique. We then conclude this chapter by outlining the extracted quantities from flow visualization that will be necessary for further analysis.

3.1 SEMA Components

3.1.1 Materials

The proposed SEMA design as in [7] consists of three essential components: liquid metal material, polymer matrix material and magnetic field source. In this study, the LM used is Galinstan (68.5% Ga, 21.5% In, 10.5% Sn; 50 g) (Roto Metals; CA, USA) and the matrix material used is a silicone elastomer known as EcoFlex 00-30 (Smooth-On; Texas, USA), as selected by [7]. Galinstan is an appropriate choice for a few notable reasons: its high surface tension ($\mu = 0.718\ \mathrm{N/m}$) offers a high degree of wettability, its chemical composition yields high electrical conductivity ($\sigma = 3.46\ x\ 10^{6}\ \mathrm{S/m}$) and low melting point (≈ -19°C) grants stability in different environments. As for the matrix material, EcoFlex 00-30 is a Pt-catalyzed silicone rubber and is a good candidate as it has a relatively low density ($1.07\ \mathrm{g/cm^{3}}$), low curing time (≈ 4 hr @ 20°C) and a low shore hardness relative to other LM-embedded substrates such as PDMS ($00 - 30 < 40 - 58\ Shore\ A$) [67]. The Galinstan serves as the conductive element and the matrix material as the SEMA's encapsulating shell. Sn-plated Cu wires (0.51-mm diameter, 24 AWG; Newark, Canada) are used as electrodes to transfer electrical current from the external circuit. The wires are inserted in the substrate and the LM coats the wires as they come into contact. The magnetic field source is chosen to be a Neodymium (NdFeB), N52 grade Ni-plated permanent disc magnet (7.62 cm diameter x 2.54 cm thickness, Mc-Master Carr, USA) with a surface flux density of $B_{surf} = 5820$ G. This magnet is similar but not identical to the one used in Mao et al.'s study only due to regional availability of products [7]. There are however similarities in both magnet's material, shape and magnetization direction, in this case through thickness, which ultimately affects the spatial distribution of their magnetic field. Meanwhile, there are differences in magnetization grade which is directly related to the remaining magnetic flux density after manufacturing (i.e., remanence magnetization), which in turn influence the magnetic field's strength. It is difficult to accurately measure the discrepancies in both magnet's field strength without prior knowledge of their manufacturing processes. Nevertheless, our selection is still a suitable alternative with regards to this study's scope which prioritizes the direction and distribution of the magnet's field over its strength. It is primarily for this reason that a numerical magnetostatic analysis is not necessary for our magnet; it has already been performed in [7]. Although, experimental characterization of the magnet is conducted to estimate the field strengths. This is done using a Hall effect sensor (ALS31313, ±500 Gauss sensitivity; Allegro Microsystems, NH, USA) to probe the magnet in a 2D predefined grid and incrementally increasing in height from 2 mm to 110 mm from the magnet's surface. The measurements are possible by attaching the sensor to the gantry of a modified FDM 3D-printer (*See Section A1*). The results highlight important characteristics of a permanent disc magnet: 1) the uniformity and symmetry of the radial and vertical magnetic fields (B_R and B_Z respectively), 2) the negligible effect of the magnetic field strength in the y-direction (B_Y) and 3) the approximately linear decay of B_Z with increasing distance from the magnet's surface Z. This behaviour correlates very well to that reported in [7] so we expect the generated Lorentz forces to behave similarly.

3.1.2 Fabrication Techniques

The elastomeric shell must encapsulate the LM safely and effectively to ensure optimal compliance matching. A form of soft lithography called replica moulding is used in this work and in [7] along with several others [6, 16, 17, 68-70]. This technique is used to duplicate the geometry of the SEMA's shell and internal networks. FDM-based 3D printing is used to manufacture the master moulds of both components with desired geometries [4, 71]. The SEMA's shell is fabricated using an FDM-printed master (Polylactic Acid (PLA) 1.75 ± 0.03 mm black, Eryone; Shenzhen, China) with embossed features and is used as a core during the casting of the Ecoflex prepolymer. Specifically in [7], an additional thin layer is cured and bonded onto the Ecoflex stamp. This process, similar to that used in microfluidic devices, results in the creation of sealed networks to contain the LM. The bulk LM is then introduced into these networks, hereafter referred to as channels, via syringe injection.

In this study, we adopt the investment casting method to fabricate channels within EcoFlex 00-30. Investment casting, which is conventionally used for metal forming, is similar to replica moulding but the master serves as a sacrificial template or scaffold. The polymer encapsulates the master and it is later removed by the application of heat or chemical solvent. Finally, internal networks remain within a continuous elastomeric shell [2]. This technique has been possible with inks and waxes [72], but recently this has been extended to commercially available solutions such as FDM printers and thermoplastics made possible by [73, 74]. Saggiomo et al. exploited Acrylonitrile Butadiene Styrene (ABS) which can be dissolved in an organic solvent such as acetone [73]. After prolonged exposure (~12 hrs), the solvent breaks down the polymer chains and forms a slurry; this allows it to be easily sacrificed or 'purged' from the formed channels. This ensures a monolithic device that reduces additional handling steps. However, there is a well-documented adverse effect when an organic solvent comes into contact with an elastomer: solvent-induced swelling. Studies have shown that organic solvents like acetone can diffuse into the porous networks and alter the dimensions of parts and channels, but these considerable effects have been observed for more volatile solvents such as toluene and DCM [75-79]. Acetone solvent is considered mild in terms of solvent compatibility (SR ~ 1.07) and these changes are reversible when left to evaporate in ambient air or elevated temperatures [80]. These effects are reported primarily for PDMS but not EcoFlex 00-30. Regardless, both elastomers have a similar chemical backbone so we assume negligible changes in the SEMA's elastomeric shell. The channel structure is therefore 3D-printed in ABS material (Polylite ABS 1.75 ± 0.03 mm, Polymaker; Changshu, China) using an Ender 3 V2 (±0.1 mm precision FDM 3D-printer, Creality; Shenzhen, China). Additionally, a 12-hr oven drying period is applied following solvent exposure as a post-treatment method to ensure deswelling of the EcoFlex 00-30.

3.2 SEMA Design

The SEMA's complete design encompasses its encapsulating shell and channels as specified by [7]. The shell's geometry consists of a square, flat substrate (45 mm x 45 mm x 3.5 mm). The channel design consists of a continuous, equidistant square spiral (see Figure 3.1). The channel and shell geometries are similar to those in [7], but some modifications are made. Filleted corners of 0.5-mm radii are used in the square spiral pattern to promote the flow of liquid metal during syringe injection. The channel profile depth is increased to 0.55 mm as it yielded the most stable and consistent 3D printing results. The depth of the 3D-printed shell mold is increased to 3.5 mm to accommodate the increased MC profile depth and channel extension height. The channel terminals are enlarged to square containers (2.5 mm x 2.5 mm), referred to here as basins, to help accommodate the electrode wires during insertion. Contrary to [7], the channel scaffold begins its loop at the outer edge basin and terminates at an elevated height coincident to the inner edge basin. The square spiral is characterized by horizontal and vertical segments (L1→L11 and H1→H11) separated equidistantly by $\Delta H = 3.75$ mm. The printing settings used for the channel design were optimized to yield the most reliable results (see *Appendix A2*). An appendage is designed to extend the length of the SEMA membrane; this serves as the flap. The flap dimensions are equal to those on the actuator side (see Figure 3.2A).

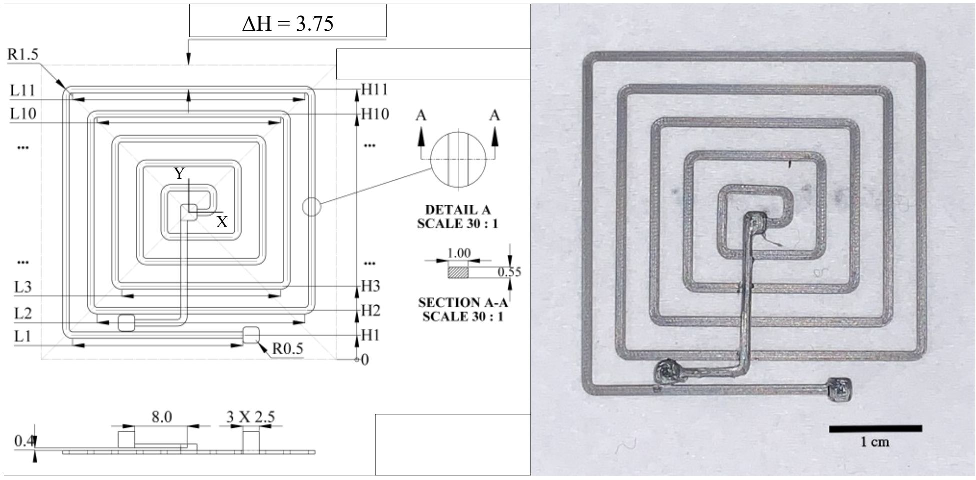

A B

Figure 3.1 A. CAD schematic illustrating important aspects of channel design and the B. FDM 3D-printed part in ABS. All dimensions annotated in the schematic are in mm.

3.3 SEMA Fabrication Process

Below summarizes the modified fabrication process for the SEMA prototype used in this study. The result of this is a prototype that is fixed along the actuator side's base and free to rotate at its flap side (see Figure 3.2E). The NdFeB magnet is positioned on the actuator side and where they are both coincident and parallel. This configuration is consistent with that used in [7] where a dynamic force analysis is conducted to estimate Lorentz forces and deformations at all channel segments. Mao et al. have simplified this analysis by treating the resultant Lorentz force as a point load exerted on the SEMA as an ideal Euler-Bernoulli beam [7]. The study reported force magnitudes on the order of milliNewtons (mN) derived from mathematical relations. Similarly here, B_Z is estimated at all height locations for the channel segments from the linear approximation and these values are then used to estimate the resultant Lorentz forces at different SEMA currents (see $Appendix\ A3$). We also report similar orders of magnitude for Lorentz forces (e.g. at $I = 3\ A; 0.014\ \text{mN} < 0.04\ \text{mN}$ [7]). The use of computational methods for performing a detailed force analysis as well as others (e.g. thermal) are out of this study's scope. It has however been thoroughly covered in [6, 7].

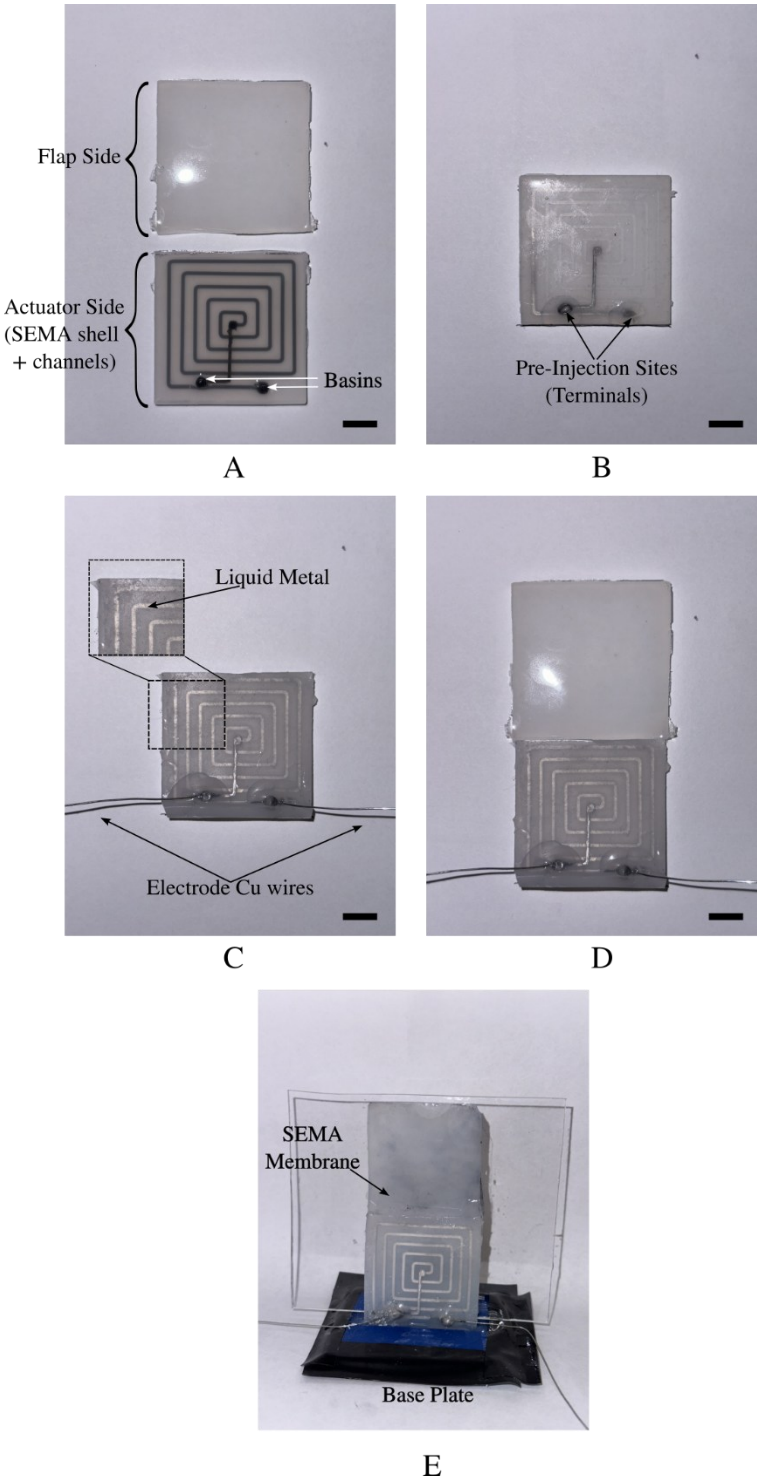

Figure 3.2 Overview of the fabrication process for the SEMA membrane. This consists of a) SEMA shell and channel moulding, b) scaffold dissolving, shell drying and liquid metal pre-injection, c) liquid metal full injection and electrode wire insertion, d) flap reattachment and finally e) base plate bonding. The transparent glass sheet displayed in e) is kept in this image for better clarity of the design details. All scale bars are equal to 1 cm.

3.3.1 SEMA Shell and Channel Moulding

(See Figure 3.2A) The estimated mass of the SEMA's 1st layer is determined by the material's density and calculated volume corresponding to half its thickness. EcoFlex 00-30 Part A (i.e., the pre-polymer) and Part B (i.e., the crosslinker) are added in equal parts (1:1 ratio) by mass and transferred into a petri dish measured on an electronic balance (Symmetry PA120, Cole-Parmer, USA) to achieve the total mass. The two-part solution is mixed thoroughly for 5 mins using a wooden craft stick procured from a local convenience store. Then, the petri dish is rested on a flat surface for approximately 1-2 mins to allow the breakdown of entrapped air bubbles at the mixture-ambient air interface that were introduced during mixing. As per the manufacturer's guidelines, the solution is poured approximately at the mould's center. An excess of EcoFlex solution equal to 5% of the desired mass is added to the mix to accommodate for the small amounts unable to be retrieved from the petri dish. Lastly, the solution is left to cure for 4 hours in ambient conditions, meanwhile the remainder of the air bubbles permeate to the mould's surface.

The channel structure is deposited by hand, using its center as the anchoring point, on the previously cured EcoFlex layer. The structure is placed on the layer's center as precisely as possible assisted by guide markers on the shell mould. The outer edges of the outermost channels are aligned with the inner edges of the ellipse-shaped markers. The rest of the structure is further inspected for any misalignments in adjacent channels and proper levelling. Following this, the channels are encapsulated within the 2nd EcoFlex layer, which is identical in mass and size to the 1st layer. The SEMA shell is now complete and is easily detached from the mould; no demoulding agent was required for this step. Finally, an Exacto knife is used to separate the flap from the actuator side following a drawn line connecting the notches. The flap is then set aside for the following stages in the fabrication process.

3.3.2 Scaffold Dissolution, Shell Drying and LM Pre-Injection

The acetone immersion bath is prepared to begin the scaffold dissolving process. The SEMA structure is placed at the bottom of a small glass container similar in appearance to the ones used in food packaging. The acetone solution (Sigma-Aldrich, USA) is then poured until the solvent's surface is flush with the height of the terminals. The SEMA structure is inspected to ensure it remains at the container's depth. Lastly, the container is placed in a chemical fume hood and securely sealed with a cap to minimize the solvent's evaporation during the exposure. Upon completion of the 12-hr exposure, the sample is removed from the acetone bath and pat dry using a disposable cloth (KimTech wipes, Mc-Master Carr) to remove any excess solvent on its surface. The channels contain an ABS-acetone slurry mixture and no defects in the mould were observed. A 10-mL plastic syringe barrel was filled with pristine acetone solvent and injected at the inlet terminal using a precision tip nozzle (.023-in diameter, Nordson EFD, USA) to purge the remaining slurry mixture within the channels. This process was repeated 3 times whereby the channel contents changed from a dark opaque color to transparent, indicating that the purging was successful. Next, the remaining acetone solution is to be removed to obtain completely hollow channels. A 3-mL plastic syringe barrel with a mounted precision tip nozzle, the same size as mentioned previously, and rubber tube assembly are attached to the facility's vacuum line. The nozzle's tip is placed within the outer edge basin and the vacuum line is then opened to evacuate the remaining acetone solution. This process lasted 10-15 seconds. The SEMA structure is dried in a vacuum oven at T = 80 ºC for a 12-hour period with the channel terminals facing up and SEMA lying flat. This is done to increase the rate of solvent evaporation through the open channel terminals and permeate through the elastomer pores. After the drying period, the LM pre-injection begins. Approximately 0.1 mL of a 1 mL syringe (25-gauge (0.515 mm diameter) tip, Expesumas; China) is filled with the liquid metal by extracting from its reservoir. The syringe is inspected for any voids or empty spaces which indicate entrapped air; it is carefully removed by lightly tapping on the syringe barrel. Then, a slight pressure is applied at the piston to minimize dead volume and extrude one liquid metal droplet. The SEMA structure is raised above the table's surface using a rectangular support to prepare it for injection; this is to ensure that the angle at which the syringe is introduced into the channel is as shallow as possible. Once the 0.5-mm diameter nozzle is inserted into the inner and outer edge basins, a steady pressure is applied to extrude enough LM so that it fills majority of the basin volume. A uniform coating of EcoFlex is deposited at both terminals to obtain proper isolation. This cannot be accomplished with pristine EcoFlex mixture as it would spread too thin once deposited due to its low viscosity. The desired effect was to maintain a droplet shape similar to that of liquid metal when deposited. The approach proposed here accomplishes this by allowing it to cure partially within the petri dish which increases the mixture's viscosity. It was observed that approximately 30-35 mins, along with intermittent mixing every 5 mins, was sufficient to let the polymerization pathway change the mixture's viscosity from a liquid to a semi-gelatinous state. As soon as the latter was obtained in consistency, one droplet for each terminal was deposited and cured for the remainder of the 4-hr period. The result of the pre-injection step is shown in Figure 3.2B.

3.3.3 LM Full Injection and Electrode Wire Insertion

A new 1 mL syringe is filled with approximately 0.5-0.6 mL of Galinstan and again inspected before use. The SEMA structure is again supported at a height above the table's surface. The LM-filled syringe is located at the outer edge basin and a luer-lock nozzle is located at the inner edge basin where both tips puncture the respective encapsulated sites. This establishes one continuous path for the escape of entrapped air from positive pressure. A steady, positive pressure is applied by hand and the liquid metal slowly fills the contents of the channels. The injection is sometimes interrupted by the sudden ballooning of the outlet encapsulated site which indicates a concentrated pressure area; this is mitigated by moving the outlet nozzle slightly to expand the punctured orifice. The channels have been filled with liquid metal once a growing droplet is observed at the outlet nozzle. The syringe extrudes a very small volume to fill the outer edge basin while slowly retracting from the punctured site. Cu-wires are inserted into the channels approximately 5 mm with respect to the terminals to get a sufficient LM coating. Encapsulation at the terminal sites is performed again with partial EcoFlex curing (see *Section 3.4.3*) to finally seal the LM-filled channels and electrode wires. The results of both steps are shown in Figure 3.2C.

3.3.4 Flap Reattachment and Base Plate Moulding

The flap set aside earlier is then reattached to the actuator side by bonding both components using Ecoflex 00-30 compound. We make sure to use this sparingly to minimize the effect on the sample's total mass (see Figure 3.2D). As shown in Figure 3.2E, the actuator+flap structure is then bonded along the actuator's width to a 3D-printed base plate using PLA material. The depth of the base plate is chosen so that it does not obstruct the electrode wires nor channel terminals. A resting wall is used to ensure perpendicularity during elastomer curing.

The result of this fabrication process yields a fully functional SEMA pump membrane.

3.4 Experimental Setup

The experimental apparatus designed for this study is shown below in Figure 3.3 and highlights the SEMA pump, control system and flow visualization assemblies. A typical experiment begins by activating the camera and light source (out of frame) to produce a live feed on the personal computer (PC). The PC is used to manipulate the image settings and trigger the camera. Upon visual confirmation of the live feed, the direct current (DC) power supply is turned on and activates the control system. This control system transmits a programmed signal to the liquid metal coil in the circuit. A current waveform is produced and transferred to the coil, where it interacts with the NdFeB permanent magnet and in turn initiates the SEMA's deformation response. At this moment, the camera can be used to capture and record the fluid-membrane interactions for several seconds. The recording is stopped by triggering the camera again from the PC and the power supply is then turned off once sufficient data has been collected according to the user. The SEMA experiences self-sustained oscillations for 1-3 seconds then rapidly decays until it reaches its initial, undeformed state. The overall workspace dimensions are approximately L = 210 cm x W = 20 cm x H = 90 cm. The following sections will discuss the assemblies and their essential components in more detail.

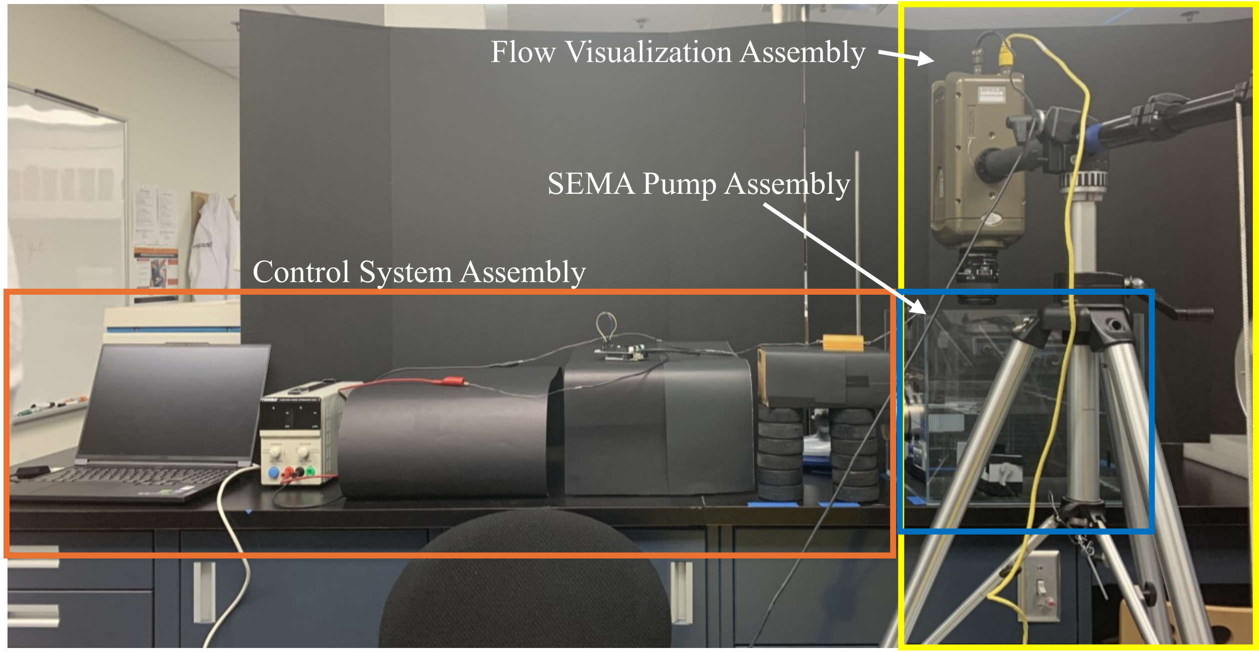

Figure 3.3 Illustration of the complete experimental setup and segmented according to the three main assemblies (see annotations in figure).

3.4.1 SEMA Pump Assembly

The SEMA membrane pump is positioned in an acrylic water tank (50.8 cm x 26.4 cm x 30.5 cm, Laqual, USA) at a height of 14.2 cm measured from the tank's bottom and centered about the tank's width. The SEMA is then oriented so that the chord axis is parallel to the tank's length (see Figure 3.4a). The electrode wires connected to the SEMA are bent so that they can reach the outside of the tank and connect to the control system. The tank is filled with distilled water up until the level at which the SEMA membrane's chord partially breaks the surface. The NdFeB magnet is positioned externally from the tank flush to its wall and the magnet's center coincides with that of the base plate. The magnet is then fixed in place using a metal rod stand and adjustable jaw clamp.

The channel walls are constructed using thin, transparent acrylic sheets (2.1-mm thick) that are cut to approximately 9.5 cm x 7 cm. The channel width is adjusted by designing a double-threaded rod mechanism whose overall length spans the width of the acrylic tank (see Figure 3.4b). The design consists of a 3D-printed double threaded rod with right-handed (RH) and left-handed (LH) threads. Two sliders are then 3D-printed, containing internal LH and RH handed threads separately, and mate with the double-threaded rod. Due to the opposing threads, one full revolution of the rod results in an equal and opposite linear translation of the sliders. This allows for the sliders to move symmetrically about the rod's midpoint. This design can achieve the largest possible channel width of 35 mm (corresponding to the threads' endpoints), a smallest possible channel width of 5 mm (corresponding to the point at which both sliders contact) and a resolution of 2 mm per revolution (equal to the thread pitch). These design features define the parameter space for the channel width denoted as d.

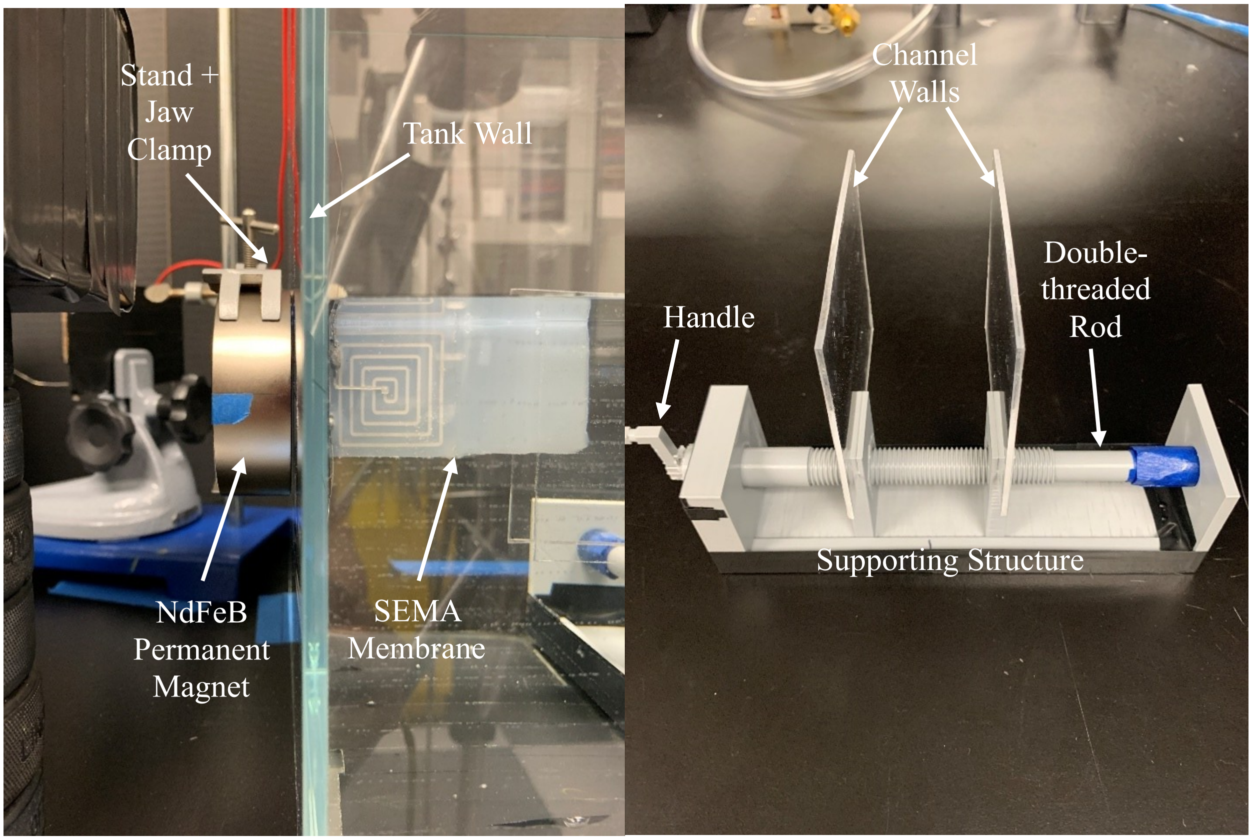

a) b)

Figure 3.4 Illustration of the primary components of the SEMA pump assembly such as the a) SEMA membrane with the permanent magnet and the b) channel wall mechanism.

3.4.2 Control System Assembly

Open-loop controllers are popularly used in soft actuators and current drivers are essential for the operation of SEMAs [7]. Mao et al.'s control system design included a waveform generated to produce a periodic input signal delivered to a 'custom voltage-to-current converter' [7]. Despite the lack of elaboration thereafter, it is likely the controller design used operational amplifiers along with additional electrical components for noise reduction and signal stability. A simple voltage-to-current converter uses an op-amp to regulate the input signal's voltage to a stable output current. Therefore, the external circuit from the SEMA's reference frame can be interpreted as an equivalent current source. Primarily, the input signal from the waveform generator (~mA) must be significantly amplified to meet the load requirements (SEMA current ~ A), which in turn also amplifies the signal's noise [81]. Secondly, most waveform generators are designed with 50-ohm output impedance, therefore supplying current to low resistive loads (e.g. $R_{SEMA} \sim 10^{-1}\ \Omega$) will result in electrical power inefficiency due to impedance mismatching. These challenges require a design balancing high output current and signal reliability. Although this has been achieved in [7], circuit design and validation are complex based on aforementioned reasons.

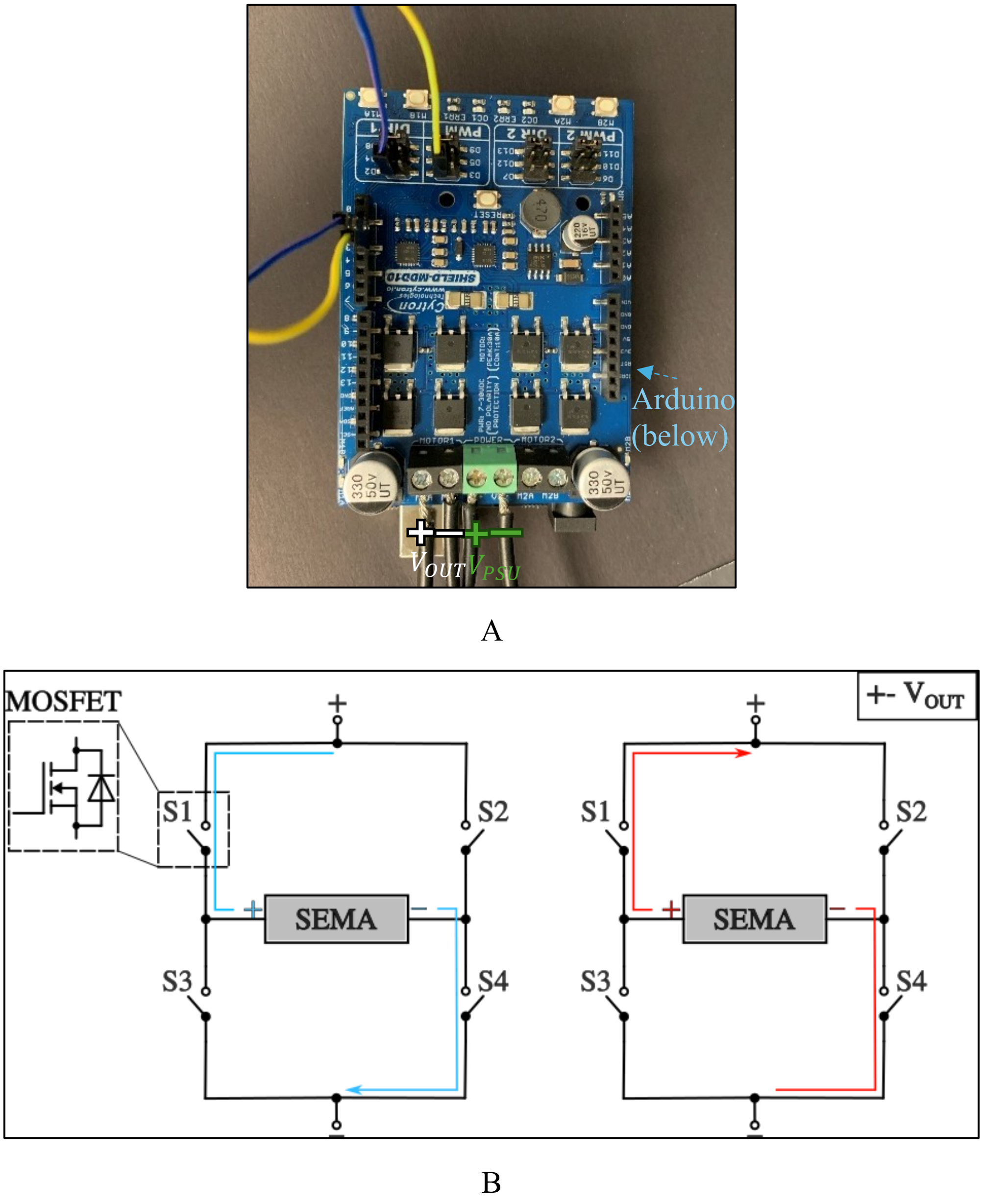

Figure 3.5 Illustration of the primary component of the control system assembly which includes the A. Arduino microcontroller and Cytron motor driver fitted atop as well as the B. simplified schematic of the H-bridge arrangement within the driver's circuit. 18-gauge Cu wires are used to connect driver terminals to the PSU and SEMA respectively. The blue and yellow DIO pin connectors are used to communicate with the Arduino UNO that rests below the motor driver. Switch symbols (Sx) are used to represent the n-channel MOSFETS and their working principle. A typical schematic of an n-channel MOSFET is shown in the inset diagram. The red and blue paths demonstrate the alternating polarity of the DC signal originating from motor driver output.

For the sake of simplicity, we turn to commercially available integrated circuits as an alternative solution, specifically H-bridge drivers for large gear motors. The drivers deliver current to inductive loads, and the H-bridge configuration allows for bidirectional motion. This is indeed a suitable controller for the smart actuator. The selected H-bridge driver (Cytron MD10C, Cytron.io, Malaysia) can deliver a maximum of 10 A and is programmed with an Arduino (Arduino UNO rev3, Arduino.io, Italy) microcontroller (see Figure 3.5A). Its working principle can be understood by analyzing the simplified circuit (see Figure 3.5b). The circuit consists of an arrangement of four n-channel MOSFETs surrounding the load in the form of the letter 'H'. MOSFETs function as gate switches: current flows through (ON) the component if the supplied voltage exceeds its threshold voltage and current flow stops (OFF) if the supplied voltage falls below the threshold. Therefore, the logical states of the MOSFET dictates the current flow and its direction in relation to the load. For example, setting the high-side S1 and the low-side S3 both ON will enable current to flow in the forward polarity across the load. Conversely, setting the high-side S2 and low-side S4 will allow current to flow in the reverse polarity across the load. The SEMA will be excited by a DC signal of alternating polarity, thereby enabling bidirectional deformation. A 1-Ohm shunt (i.e., current sensing) resistor is placed in the circuit in series to collect voltage measurements for circuit validation. This is covered in more detail in the next section. The protruding pinouts from the Cytron board are matched and inserted into the female ends on the UNO microcontroller. The DC power supply is connected to the Cytron board's terminals, effectively providing power to both Arduino and Cytron boards.

3.4.3 Circuit and Frequency Validation

The Arduino UNO board controls the Cytron board's duty cycle using a PWM signal, in turn dictating the magnitude of the output current. A simple control algorithm was written in Arduino IDE 1.8.2 and utilizes the Cytron motor driver library functions to transmit commands to the motor driver (See *Section A4*). The sequence of the commands are as follows: set the driver's duty cycle with a value ranging from 0 to 255, set a delay time equal to half of the actuation period, set the driver's duty cycle with a value ranging from -255 to 0 and finally set another delay time equal to the other half of the actuation period. This will enable the circuit output current (I_{OUT}) to be a proportion of the DC supply current (I_{DC}). The DC power supply unit supplies 7 V to the circuit and constant duty cycle values are chosen: 20%, 40% and 65%. These are deduced from a simple Kirchoff law analysis in order to achieve the desired values for actuation current (1 A, 2 A and 3

A). This corresponded to PWM values of 55, 110 and 165. A DAQ (NI-9239, National Instruments) was attached to the shunt resistor in parallel to measure its voltage potential. These measurements across a known resistance are used to infer about the actuation current flowing in series with the SEMA. The supply voltage from the DC source was adjusted until desirable and consistent readings from the DAQ were achieved considering variations in frequency. Adjustments in the supply voltage were expected as LM-based devices experience fluctuations in resistance due to deformation and LM contact with wires.

The DAQ readings were transmitted to a local desktop computer and plotted in real-time using a custom MATLAB script for approximately 15-20 seconds (see Figure 3.6). The raw data was then extracted, and a Fast-Fourier Transform (FFT) analysis was performed to evaluate the frequency content of the signal. The result was a detection of two prominent peaks when plotting the dimensionless signal amplitude and the one-sided frequency range (positive values only): the largest peak corresponded to the actuation frequency programmed in the control circuit and the next prominent peak corresponds to the Arduino UNO's PWM frequency (~490 Hz) which is present by design. In order to de-noise the raw data from the DAQ signal, a digital lowpass filter was applied to attenuate the high frequencies. A cut-off frequency of 30 Hz was used for all (current: I , frequency: f) combinations which balanced noise rejection and signal preservation. The filtered signal shows an alternative square wave, as expected based on the input, with clearly identifiable peaks. Finally, a peak detection algorithm developed in MATLAB, specifically for this study, was used to capture the electrical current at these peaks; this represents the actuation current (I). Electrical current values at these locations are estimated by converting the data points from the filtered voltage signal using $I\ (t) = V(t)/R$. For example, the signal shown in Figure 3.6 shows consistent peak voltages around ±1 V. The electrical current is therefore close to ±1 A knowing that $R = 1\ \Omega$. This confirms that the control system design is capable of reliably delivering the appropriate current to the SEMA and the rest of the circuit. Frequency validation tests were also performed to confirm that the controller logic is ensuring that the output signal from the Cytron driver is delivered at the selected frequency. This characteristic frequency corresponds to the actuation frequency (f). An FFT analysis, same as those done for the circuit validation tests, demonstrates that the significant frequency of the signal in Figure 3.6 is 1.003 (~ 1) Hz. This confirms that the control system design can operate on the SEMA and the rest of the circuit at the desired frequency.

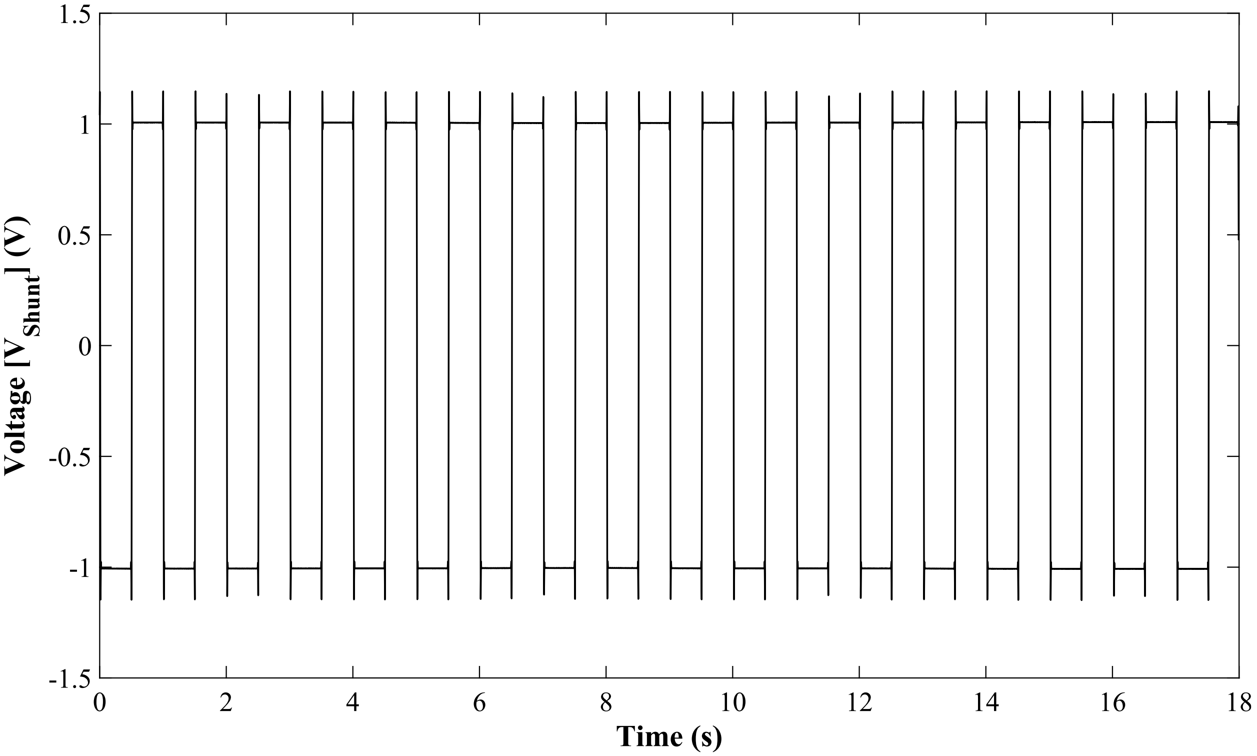

Figure 3.6 Voltage potential measurements across 1-Ohm resistor (V_{shunt}) connected in series to the control circuit at I = 1 A and f = 1 Hz. This signal is the result of the 30-Hz lowpass filter.

3.4.4 Experimental Parameters

Upon implementation of the SEMA pump and control system assemblies, we now define the input variables that represent the experimental parameters for the SEMA's operation. They are channel width (d), actuation current (I) and actuation frequency (f). Hereafter, an experimental condition can be characterized by d and/or I and f. The table below summarizes the parameter space in the context of this study.

Table 3.1 Summary of Experimental Parameters

Channel Width (d)	**Actuation Current (I)**	**Actuation Frequency (f)**
15 – 35 mm	1 – 3 A	1 – 3 Hz

3.4.5 Flow Visualization Assembly

The fluid dynamics in the membrane's wake can be investigated using flow visualization techniques. In brief, this consists of capturing flow information in a defined observation region using optical systems and performing an analysis through measurement techniques. The flow domain constructed in this study is an open channel flow in the absence of a freestream ($U_\infty = 0$, $St = \infty$). The flow is investigated using the digital particle image velocimetry (DPIV) technique, which is a quantitative method that captures digital images in a region of interest (ROI) and estimates the local velocities in the flow using microscopic particles distributed in the fluid (see Figure 3.7). These velocity measurements can later be used to reveal more information such as derivative and integral quantities like vorticity, circulation and pressure. A Complementary Metal-Oxide Semiconductor (CMOS) high-speed camera (Phantom v310, Vision Research Inc.; Wayne, NJ) with a 1280 x 800 (12-bit) frame resolution set to a capture rate of 300 Frames Per Second (FPS) is used to acquire images. A Nikon AF Micro-Nikkor 60 mm f/2.8D lens (Nikon; Tokyo, Japan) was attached to the camera to adjust image settings. Illumination is needed to optimize the contrast of images. We use a high-powered, incandescent light source with 300-W halogen bulbs (Pallite VIII, Toronto Surplus and Scientific Inc.; ON, Canada). The camera and light source are oriented in such a way to capture the flow information in the plane coincident to the SEMA membrane's thickness (i.e., chordwise) and perpendicular to its width (i.e., spanwise). This was accomplished by fastening the camera system to a perpendicular arm which was then secured to a tripod standing on the floor. The weight imbalance was then corrected by adding a 30-kg counterweight on the arm's opposite side, whose position was determined by a spirit level indicator placed at the arm's midpoint. DPIV systems can vary greatly from one investigation to the other depending on the nature of the experiment and available equipment. Nonetheless, a general workflow with acceptable guidelines is prevalent in research. A standardized approach has therefore been established, according to [82] and [83], which is covered in the experimental procedure.

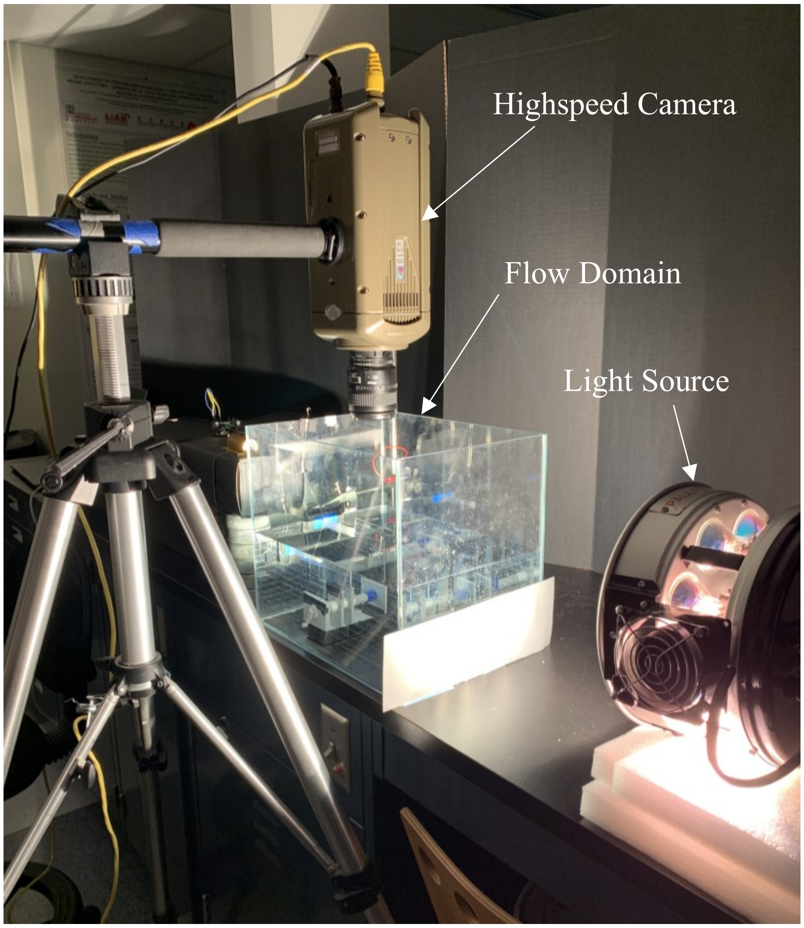

Figure 3.7 Primary components of the flow visualization assembly.

3.5 Experimental Procedure

We begin by discussing the guiding principles and general theory surrounding DPIV. Later, these principles are used to justify the approach for flow visualization used in this study. Finally, we discuss another aspect of the study which pertains to the stability in the SEMA's design based on deformation and electrical resistance.

3.5.1 DPIV Principles

The principles discussed here consider 2D (i.e., planar) DPIV; the flow is investigated in an observation plane defined by $X - Y$. Figure 3.8 summarizes the important steps in a typical DPIV investigation. A high framerate digital camera captures the observation plane in its field of view (FOV), within which contains the ROI for the fluid under study. Particles that are seeded in the fluid have neutrally buoyant ($\rho_{particle} \cong \rho_{fluid}$), electrical and chemical properties that do not alter the fluid's flow and properties. In most cases, the round particles are mixed homogeneously within the fluid's entire domain ($L\ x\ W\ x\ H$); it is therefore necessary to highlight the particles lying in the observation plane. A light source, typically a high-powered continuous wave (CW) or double-pulsed laser and optical stage, is used to illuminate the observation plane by converting a collimated, monochromatic beam to a rectangular sheet of light. The incident light hits the round particles and produces uniform light scattering. The camera is oriented perpendicularly to the light source to capture the high intensity signals from the illuminated particles compared to the out-of-plane particles and other background components. Image acquisition is then performed by capturing N successive frames coordinated with the activation of the light source; each frame represents a snapshot of the flow at an instant in time. This is then followed by image evaluation, which begins by sorting N frames into pairs. For each image pair (Img A and Img B), the positions of particles are displayed at two instances in time, separated by a short time interval Δt. Image evaluation is sometimes preceded by image pre-processing, which consists of applying computer-based filters to enhance image contrast and minimize digital artifacts. Image evaluation employs a statistical method to correlate the particles' signals from image A to B using the cross-correlation algorithm. This process begins by partitioning the image dimensions into equally smaller areas called interrogation areas or windows. An FFT-based approach is used to analyze the signal frequencies in the same interrogation area between both images. A peak is then detected which corresponds to a high pixel intensity; this is identified as the position of a particle. The detected peaks in both images are correlated with each other to determine the likelihood of the particle’s real position. This is characterized by the cross-correlation coefficient; a value closer to 0 means it is less likely while a value closer to 1 means it is more likely. The change in position of both correlation peaks is used to estimate the particle’s displacement. Advanced image processing techniques can be used to determine the positions with sub-pixel level precision. A proper selection for interrogation window size ensures good particle image density (~8-10 particles/ interrogation window). Additionally, a good window size and selected temporal resolution ($= \Delta t$) ensure that a particle’s displacement does not exceed ¼ of the window’s linear dimension between two frames. This is known as the ¼ rule and is used to minimize the loss of particle pairs in the observation plane. The summarized process above is performed on all particles in all interrogation areas for both frames; it can also be repeatedly executed until it converges to a value of high statistical significance. Finally, using the estimated displacements for a known time interval Δt, the velocity vectors can be calculated. Some velocity estimates may be deemed inaccurate or erroneous, either from intuition or visual inspection. For example, this is present in flow discontinuities such as in regions near solid boundaries and edges. These velocity vectors are labelled as ‘spurious’. A post-processing stage is therefore important to validate the velocity vectors with respect to certain criteria, identify, discard and replace spurious vectors by interpolation. Validation criteria can be established using various filter-based algorithms. A local median filter is commonly applied in validation, among many others, and is considered a robust outlier detection method. Following this, spurious vectors are replaced with acceptable ones which are calculated using low to high-order interpolation schemes. This entire procedure is repeated across all frames to complete the DPIV investigation, resulting in an array of velocity vectors across equidistant grids that form velocity fields for each frame. The velocity fields can be used to reveal more information about the flow by obtaining derivative and integral quantities via discretized equations; examples of such quantities are vorticity and circulation respectively. An in-depth background of DPIV concepts along with a detailed explanation and implementation of algorithms is not covered in this thesis; this has been extensively covered in [82] and [83].

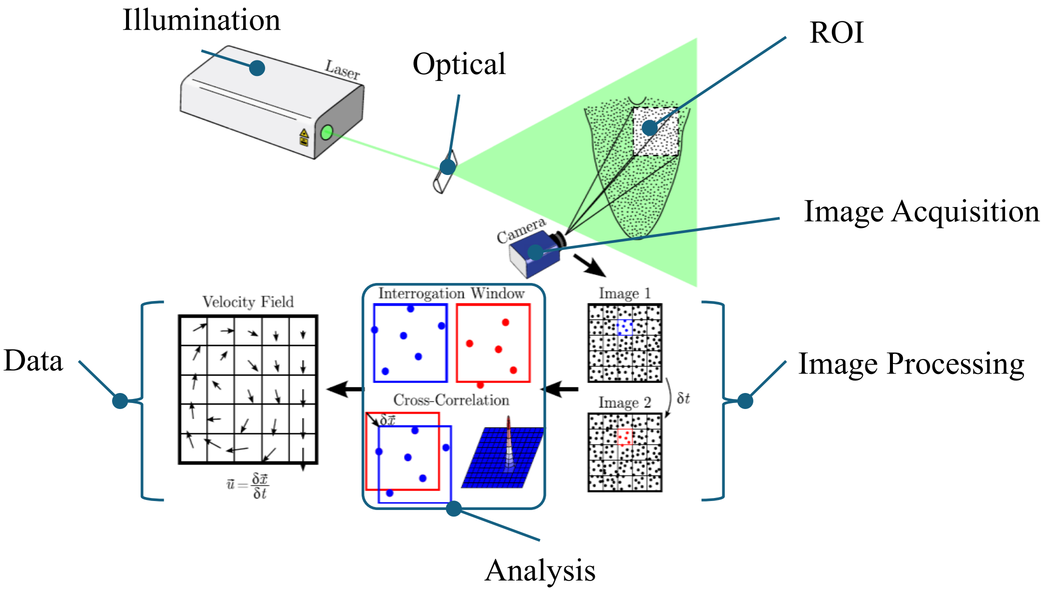

Figure 3.8 Overview of the DPIV principles. Adapted from [84].

3.5.2 *Seeding Particles*

An appropriate selection of seeding particles considers important factors such as the working fluid, particle size, refractive index and light scattering for compatibility in DPIV optics. Additionally, the ability for particles to exhibit flow fidelity is crucial, which refers to their ability to reliably trace as much as complex flow patterns with minimal delay. This can be quantified by the particle's response time (τ_p) which considers the dynamic effects of fluid viscosity and gravity. τ_p must then be compared to a time scale that is characteristic to the flow (τ_f) to determine the degree of fidelity; this is quantified by the dimensionless Stokes' (St) number. The τ_p and St variables are modelled as:

$$\tau_p = {d_p}^2 \frac{\rho_p}{18\mu}$$

$$St = \frac{\tau_p}{\tau_f}$$

where d_p is the particle's diameter, ρ_p is the particle's density and μ is the fluid's dynamic viscosity. A particle is considered to exhibit good flow fidelity if $St < 10^{-1}$. [83] The selected seeding particles for this study are 50 ± 20 µm Polyamide-12 particles (Dantec Dynamics, Denmark). The particle's response time can be calculated knowing the particle's density ($\rho_p = 1030\ \mathrm{kg/m^3}$) and approximating the working fluid's dynamic viscosity to be equal to that of water at ambient conditions ($\mu = 1.0016\ \mathrm{mPa \cdot s}$ @ $20°\mathrm{C}$). Following this, an appropriate τ_f is chosen to be half of the SEMA's flapping period at $f = 3$ Hz. When the SEMA reaches half of its flapping period, it is the point at which it is travelling at its highest instant acceleration in its cycle. If the particle can reliably follow the flow at these instances for the shortest half-cycle duration in experiment, it is also assumed to be reliable for longer time scales corresponding to lower actuation frequencies. Finally, St is calculated to be $8.57\ x\ 10^{-4}$ and the particles are therefore considered to have good flow fidelity by satisfying the condition mentioned above.

3.5.3 DPIV Parameters

In this study, each experimental condition is simulated for approximately 15 seconds. Continuous recordings for each condition are acquired using the Phantom v310 with the Nikon lens. The Pallite VIII illuminates the selected observation plane. Conventional DPIV setups implement high-powered lasers to form thin light sheets, however this was unfortunately not used in this study due to the limited availability of laser equipment. We acknowledge that utilizing incandescent light sources presents some disadvantages particularly low efficiency, low light intensity due to high divergence and difficulty using optical arrangements that can cause undesirable light dispersion due to carrying the full color spectrum [85]. Although the selection of light source is sub-optimal, we try our best to adhere to the guidelines and standards of DPIV as discussed in *Section 3.6.1.* The acquisition mode used is a single frame/single exposure mode in which successive frames are captured with a continuous exposure of light. This means that successive frames are separated by a time interval equal to the acquisition period during which the camera's lens remains exposed. In this manner, the temporal resolution $\Delta t = 3.\overline{3}$ ms is governed by the camera's capture rate. These settings along with triggering the recording are controlled manually in the Phantom Camera Control (PCC) software. The distance between the lens and the free surface was adjusted so that the SEMA's flap, fluid confined by the channel walls and the outlet are captured in FOV. We partially excluded the inlet and the remaining portion of the SEMA as we are more interested in the fluid behaviour downstream. The light source is oriented so that the incident light is directed parallel to the flow. A black, rectangular sheet was attached to the side of the tank facing the light source and used to minimize the illumination of out-of-plane particles and background. The distance between the light source and tank wall along with the lens aperture were adjusted until the image had good light intensity, scattering and focus; the resulting aperture (f-number) is 5.8 and the depth of field is 30 cm. An example of a raw DPIV showing the FOV is shown in Figure 3.9. This is then followed by spatial-image calibration which consists of mapping the image to the real-world frame of reference. This procedure is essential for displacement and velocity estimations, therefore a L x W calibration target with equidistant 4-mm holes is 3D-printed and placed in the FOV. Using image processing software, three different holes are measured several times which resulted in an average calibration scale of 0.05857 mm/px. In this manner, the resulting FOV is 74.97 mm x 46.86 mm. All the PIV parameters mentioned in this section remain constant across all experimental conditions.

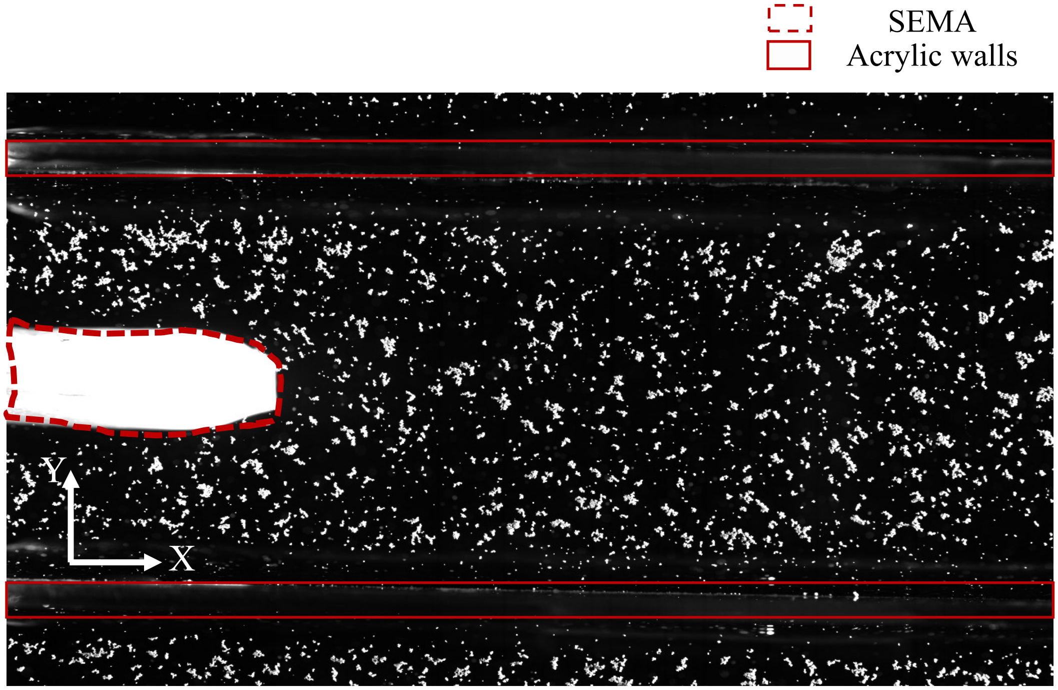

Figure 3.9 Raw DPIV image illustrating this study's field of view for flow investigation. The flow information is defined by the coordinate system displayed in the left corner. The SEMA membrane and channel walls are identified using the legend in the top right.

3.5.4 PIV Pre-Processing

The following stages of the DPIV workflow are conducted offline using an open-source, GUI-based software tool in MATLAB called PIVLab (v.3.01). This tool is a free alternative to other commercial solutions that can conduct a complete DPIV investigation with relatively great performance and accuracy [86, 87]. The complete DPIV workflow along with algorithms implemented in PIVLab are shown in Figure 3.10. In this study, the acquired images are imported into PIVLab and are then pre-processed. Despite the efforts made to optimize the DPIV images in the experiment, image contrast enhancement was essential. Initially, a dynamic mask from a custom algorithm was created for the SEMA and imported into PIVLab for the purpose of excluding it from the rest of the computation[1]. Next, background removal is performed which reduces intensities for background pixels by calculating the mean of all input images and subtracting this result from them. Next, Contrast Limited Adaptive Histogram Equalization (CLAHE) is enabled for all images. This is a modification to the histogram equalization technique which consists of 'stretching' an image's intensity histogram so that it reaches the full extent of the image's intensity scale (e.g. 0 to 255). In this case, CLAHE performs this technique in smaller partitions in the image called tiles. This allows for local adjustments for high and low-intensity regions and is reported to increase probability of valid vector detection by 4.7 ± 3.2% [87]. As per the developer's recommendations, the selected tile size used for this study is 64 px. An intensity highpass filter (48 px size) followed by an intensity capping algorithm was enabled. Intensity capping applies an upper limit to the pixel intensity values which replaces any value that exceeds this limit with itself. This reportedly reduces correlation bias and improves the detection probability by 5.2 ± 2.5%. Global min/max intensities are set for all images which yielded good intensity distribution. PIVLab then conducts image evaluation by applying a discrete Fourier transform (DFT) and window deformation technique. Window deformation transforms the interrogation areas according to the displacement estimation and, coupled with area overlapping, yields a transformation matrix for all edge points. The interrogation area is resampled using bilinear interpolation to estimate the transformation for all embedded pixels. Window deformation is an advanced approach that considers large velocity and shear gradients [86]. The selected approach for the image evaluation is a multi-pass, coarse-to-fine interrogation approach. This means that the algorithm computes the displacements for multiple evaluation passes in which the interrogation areas are progressively reduced at each pass. Therefore, a total of four passes is used

---

[1] Custom MATLAB scripts for SEMA oscillation tracking, dynamic masking and DPIV data visualization are all available on: https://github.com/ma-mastroianni/exp-investigation-ofthe-flow-generated-bya-flex-flapping-membrane-based-ona-soft-EM-actuator

in this study: 72 px x 72 px, 54 px x 54 px and 40 px x 40 px (repeated in the final pass) interrogation windows with 50% overlap. These window sizes are chosen to ensure good particle density and obey the ¼ rule. The spatial resolution of the velocity fields is dictated by the final pass size and refined due to the 50% overlap: 1.2 mm x 1.2 mm (20 px x 20 px). The 2x3 point fit is selected as the correlation peak finding method for sub-pixel estimation.

3.5.5 DPIV Post-Processing

The post-processing stage in PIVLab is separated into two steps: image validation and vector validation. A contrast threshold filter is applied for image validation which discards vectors that have an associated peak intensity lower than the specified threshold. This is to help reduce any image artifacts that have persisted after pre-processing. As for vector validation, PIVLab initially performs local median and standard deviation filters between each pass but not at the final pass. This threshold corresponds to the value at which no vector must exceed the median within the neighborhood by a difference of n. On the other hand, the standard deviation filter verifies if a vector lies within n standard deviations from the mean with respect to the instantaneous velocity field. The discarded vectors are then replaced by a boundary value solver interpolator and smoothed by a penalized least-squares method with a smoothing strength of $S = 0.9$ [86, 87]. The local median filter consists of a 2D, 3x3 neighbourhood with a $n = 1.5$ deviation threshold. The standard deviation filter applies a $n = 4$ standard deviation threshold. Following this, additional validation is optional and performed here. An interactive filter is applied which sets lower/upper limits to the velocities according to the ¼ rule; this is done by selecting the acceptable region in a u-v scatterplot. A stricter local median filter ($n = 1$) is then applied. Finally, the resulting vector fields are interpolated and smoothed ($S = 1.0$ – strongest) using the same schemes as mentioned above.

Assessment of measurement uncertainty is an important but difficult task since DPIV conditions vary greatly depending on the application. Nevertheless, it is assumed that the uncertainty of velocity estimation is conservatively ± 5 % for all test conditions. This encompasses the inherent factors of DPIV starting from image evaluation, the details of which are explained in [84].

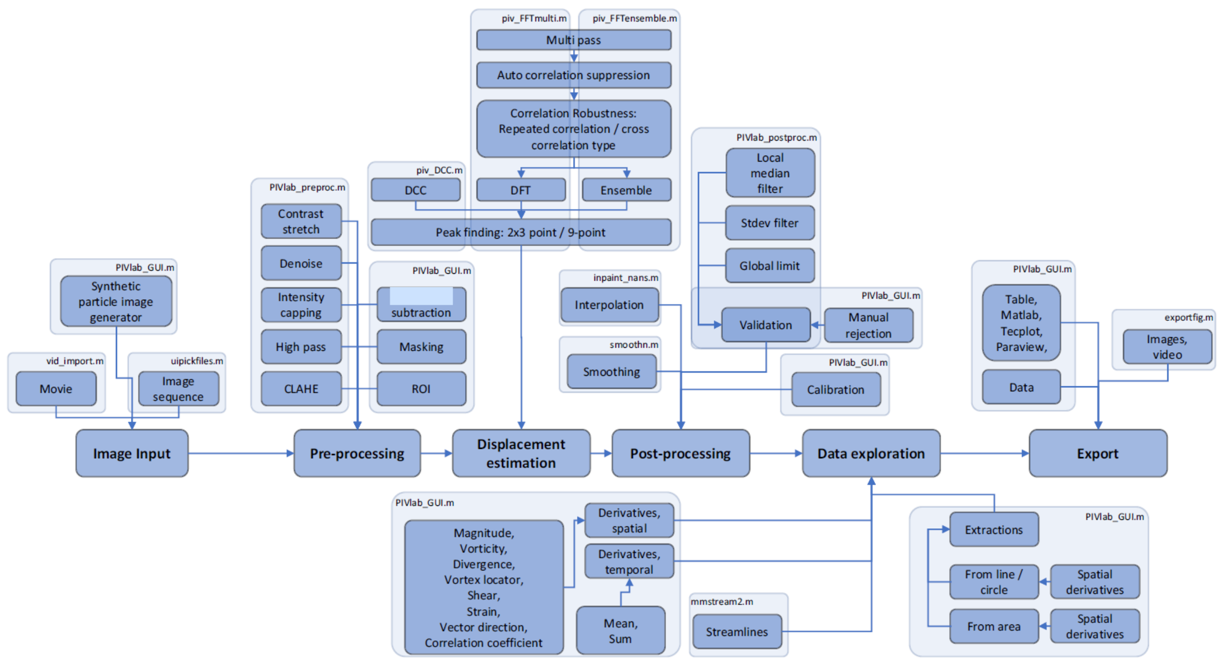

Figure 3.10 PIV processing workflow implemented by the open-source, flow visualization software (PIVLab). Adapted from [86].

3.5.6 *SEMA Deformation and Resistance*

An important metric for the SEMA's performance is the characterization of its electrical resistance with respect to its deformation. This has been done in [7], however it is necessary to investigate in this study to verify the modified design. The DAQ device, the same as the one used in the circuit validation tests, is connected in parallel to the SEMA terminals and the same MATLAB script is used to collect voltage potential measurements for a 15-second duration. Again, this is done for all I and f combinations. During the SEMA's operation, we utilize the high-speed camera to capture the SEMA's deformations characterized by I and f and measure the deformation amplitude. A black marker was drawn near the tip of the flap so that its movement can be easily tracked in the PCC software. Further processing was required after collecting these measurements to smooth the data.

3.6 Selection of PIV Data

A partial DPIV investigation, which excludes post-processing, was conducted on all test conditions outlined in Table 3.1. The purpose was to evaluate the percentage of valid vectors to the total amount of vectors in the velocity field. This metric is assigned as the valid detection probability (VDP) in PIVLab and was calculated for each instantaneous field. According to [82] and [83], a range of 5-10% of spurious vectors with respect to the vector fields is a good indication of high-quality DPIV measurements. However, this study implements sub-optimal equipment (i.e., light source) which negatively impacts the VDP. In this manner, this criterion was relaxed to VDP ≥ 85% for compensation. Any test condition whose instantaneous velocity field's VDP fell below the threshold was discarded from further analysis. This resulted in a final count of 21 experimental conditions. The duration of each experiment was approximately 15 seconds, which includes the instant the SEMA is powered on until the instant it is powered off.

3.6.1 Extracted Quantities and Data Visualization

The flow characteristics in the SEMA's wake is analyzed from the velocity ($\vec{v}$) and spanwise vorticity ($\vec{\omega}_z$) fields. We are specifically interested in the flow organization and development in the streamwise direction in time which can be obtained from the instantaneous/mean velocity fields and profiles respectively. The streamwise velocity ($\vec{u}$) is equal to the horizontal (x) component of $\vec{v}$. In this study, the velocity profiles resolve $\vec{u}$ vectors on a straight line along the transverse (y) direction. Additionally, we are interested in the flow structures in the wake in time obtained from the instantaneous/mean vorticity fields. Vorticity is the spatial derivative of velocity which quantifies the strength of the fluid's rotation and is calculated in PIVLab using MATLAB's curl() function. In this context, the term 'instantaneous' refers to the field/profile for a frame corresponding to an instant in time t, while 'mean' is simply the resulting field/profile of the arithmetic mean of the selected fields/profiles. The chosen instances for analyzing flow information corresponded to significant points in the SEMA's cycle: downstroke (start), upstroke acceleration, upstroke, downstroke acceleration and downstroke (end). In the case of the mean components, this would correspond to multiple cycles over a time interval. This time interval (t_{int}) represented 2 seconds before and after the simulation midpoint ($t_{end}/2$) which was chosen to exclude the transient power-up and power-down phases of the SEMA. A set of custom MATLAB scripts (see *Footnote 1*) was therefore developed to estimate the SEMA's flap position from binary

DPIV images, estimate displacement peaks and significant points from the measurements during the specified time interval. The corresponding time instances and frame numbers for one complete cycle and those corresponding to the beginning and end of time interval are extracted. These variables are then used in PIVLab to manually extract the equivalent $\vec{\omega}_z$ fields, $\vec{v}$ fields and $\vec{u}$ profiles. The velocity profiles are extracted from the instantaneous/mean $\vec{v}$ fields at five streamwise locations separated by approximately half-chord distance (=22.5 mm). This process is repeated for all test conditions.

Data visualization is already possible using the PIVLab tool, however the resulting data was modified in the MATLAB environment for more versatility. The experimental environment, consisting of the channel walls and SEMA mask, was essentially reconstructed into a figure using a custom MATLAB script (see *Footnote 1*). Then, the vector fields and profiles can be selected by the user and overlaid on the figure.

4 RESULTS

This chapter is dedicated to the discussion of two main components of the study: SEMA pump characterization and DPIV analysis. The SEMA pump's characterization is presented at the beginning of this chapter. Firstly, we investigate the effects of the actuation current (I) and frequency (f) on the flap's deformation amplitude. The relationship between the pump's electrical resistance and deformation amplitude is then analyzed for all possible (I, f) combinations. These tests are performed to assess the SEMA pump and control circuit's operational performance. The second part of this chapter focuses on the characteristics in the SEMA pump's wake in terms of the flow velocity and vorticity fields obtained from DPIV. The wakes are then classified based on the flow's direction and mapped according to actuation frequency (f) and channel width (d). This is done to visualize all DPIV conditions and observe any noticeable patterns.

Conditions of the fluid flow in experiment are described by the channel width (d), actuation current (I) and frequency (f). We establish a naming convention for the dataset according to the selected I, f or d, I, f values in each experiment. For example, a nominal deformation amplitude recorded at $I = 1$ A and $f = 1$ Hz is labelled as $I1, f1$ and an instantaneous vorticity field for $d = 20$ mm, $I = 3$ A and $f = 2$ Hz is labelled as $d20, I3, f2$. This naming convention is used to describe all experiments in the rest of this thesis. Furthermore, all results shown in this chapter are obtained from the respective tests performed on a single SEMA pump sample.

4.1 SEMA Pump Characterization

The electrical resistance to deformation behaviour is an important metric to evaluate the overall design and performance of smart actuators (*see Section 3.6.4*). A material's electrical resistance is proportional to its length and area through which electrical current is travelling (i.e. cross-sectional area). In LM-embedded devices, the deformations cause a change in the channel dimensions, which in turn changes its cross-sectional area, and therefore results in the deviation of its electrical resistance from that in the undeformed state [7, 88]. The deformation behaviour is better understood by examining the effects of the actuation current and frequency on the flap's kinematics. The measurements in Figure 4.1A and B demonstrate that actuation current and frequency significantly influence the deformation amplitude. For a constant actuation frequency, an increase in the actuation current results in an increase the deformation amplitude as expected due to the higher magnitude of Lorentz forces. Conversely, for a constant actuation current, the deformation amplitude decreases with increasing actuation frequency. The flap's deflection is affected by the contributions of bending forces owing to Lorentz principle and added-mass forces owing to the surrounding fluid [38]. The extent of their contributions requires further analysis that is not done here, but is covered in [38]. The linear relationship in actuation current as well as the nonlinear relationship in actuation frequency with deformation amplitude are also observed in the original SEMA's design [7]. These similarities indicate a good replication of the SEMA's dynamic behaviour. The marker tracking method for all (I, f) combinations measured in PCC software yields good accuracy (< 15% deviation). The deformation behaviour was analyzed by decoupling I and f to observe their independent contributions on the flap's deformation amplitude. Both quantities indeed affect the flap's behaviour and implies that it primarily governs the flap's kinematics.

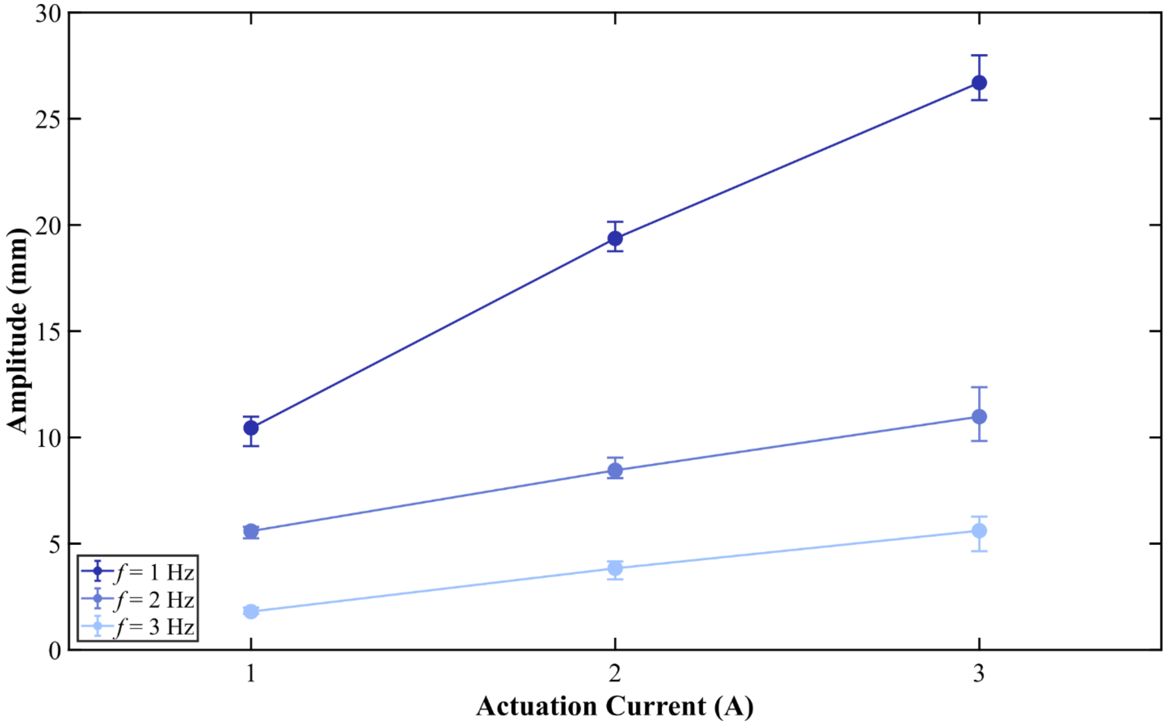

A

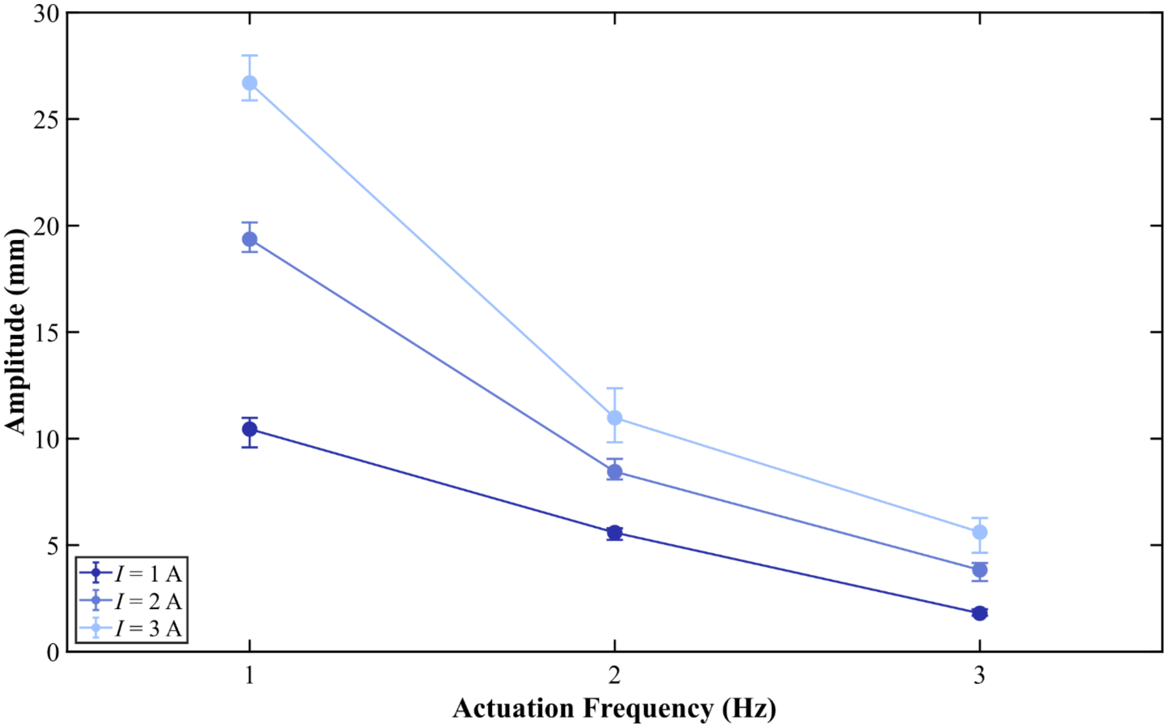

B

Figure 4.1 Flap deformation amplitude of the SEMA membrane pump as a function of A. the actuation current (I) and B. the actuation frequency (f). Mean amplitude values are represented by markers and deviations from the mean are represented by the upper and lower vertical bars.

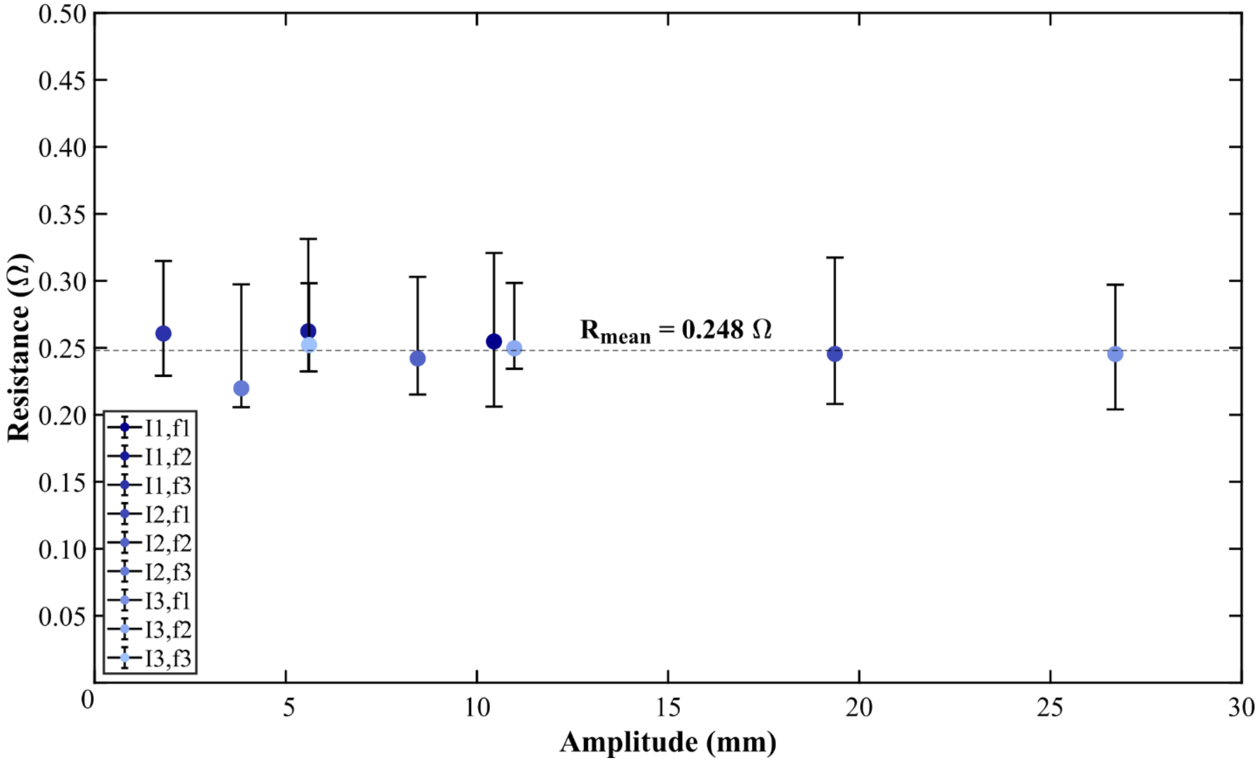

Figure 4.2 SEMA membrane pump's electrical resistance as a function of its flap deformation amplitude for all (I, f) combinations. Mean resistance values are represented by markers and deviations from the mean are represented by the upper and lower vertical bars. Only mean amplitude values are shown here for clarity. The dotted line represents the average of mean resistance values for all (I, f) combinations; its corresponding value is denoted by R_{mean}.

We proceed to assess the SEMA pump's design and performance by investigating the relationship between its electrical resistance and deformation amplitude. First, it is worth mentioning that the resistance values obtained in the experiment are expected to be higher than those obtained in theory due to the inherent properties of LM-embedded devices. Contact resistance between Galinstan and Cu wire [89] and the presence of the Ga-oxide layer (see *Introduction*) are significant factors that increase the measured LM resistance. Overall, the results yield approximately 20% variability in resistance across all conditions relative to their mean value and less than 10% deviations of the mean resistance values from the average ($R_{mean} = 0.248\ \Omega$). The former is substantially larger than that reported in [7] (5% variability) and this can be explained by the circuit's inherent design. During the high- and low-side switching of the MOSFETs, the flow of current is changing direction and a voltage spike is recorded at these instances. Similar voltage spikes are also observed in motors which represent the voltage induced by the inductance of their coil windings. Inductors generate a magnetic flux (i.e. change in magnetic field) as the flow of current changes which results in an induced voltage that is proportional to these variables. Essentially, the voltage spike opposes the direction of current which is a phenomenon known as back-EMF [90]. In the case of the SEMA, the voltage spikes also coincide with the instances of alternating current direction. This indicates that, despite the assumption that the SEMA behaves as an ideal resistor in [7] and in this study, it is possible that it has a non-negligible inductance. In this manner, the SEMA's resistance may be overestimated. The variability is also consistent across most of the experimental conditions, likely due to the voltage spikes observed at all peaks in their respective signals, which further supports the existence of an inherent characteristic in the circuit like inductance. However, confirmation of this would require further circuit analysis using other diagnostic tools. Other factors that may affect the estimated resistance, aside from those mentioned earlier, include contact resistance from the Cu wires leading to the DAQ and SEMA terminals as well as noisy artifacts in the signal that have persisted past the lowpass filter. Nevertheless, the estimated resistance for the SEMA pump prototype is relatively close to that of Mao et al.'s SEMA ($R = 0.18\,\Omega$) [7]. Apart from the inaccuracies mentioned previously, this discrepancy is primarily due to the increase in the channel's profile depth and overall length (e.g., from filleted edges and MC extension). This characterization indicates that a robust and reliable SEMA is achieved from a modified design and fabrication process. In fact, this process offers a potential workaround to the challenges associated with bonding a separate elastomer layer to an existing channel mould as done in [7]. Precautionary steps in manual handling are necessary to ensure 1) adequate use of adhesive/bonding agent to avoid undesired delamination [2] while applying sufficiently high pressures for LM syringe filling [91] and 2) adhesive bonding agent does not infiltrate and possibly obstruct channel pathways [92]. These risks have not been addressed in Mao et al.'s study, therefore the proposed method used here helps mitigate them.

4.2 Flow Analysis

The flow generated by the flapping of the SEMA pump membrane is investigated by classifying the experiments according to three types of observed flows in the wake: 1) propagating flow, 2) non-propagating flow and 3) reverse flow. From the total 21 experiments, three conditions are selected for each flow type in an attempt to best illustrate them and their characteristics. A given experimental condition is first analyzed via the $\vec{v}$ and $\vec{\omega}_z$ fields at recorded instances in one flapping cycle (numbered 1 to 5). Following this, the phase-averaged ($\langle vec \rangle$ notation) and time-averaged ($\overline{vec}$ notation) $\vec{v}/\vec{\omega}_z$ fields are shown as well. Here, a phase-averaged quantity refers to an average vector field over one flapping cycle, whereas a time-averaged quantity refers to an average field over the time interval t_{int}. The velocity vectors are normalized with respect to their magnitudes so that they are of equal length. Then, the respective phase-averaged and time-averaged $\vec{u}$ profiles are plotted. Unlike the $\vec{v}/\vec{\omega}_z$ fields, the $\vec{u}$ vectors are scaled with respect to the mean magnitude of the phase-averaged ($\left|\langle \vec{u}_p \rangle\right|_{avg}$) and time-averaged ($\left|\overline{\vec{u}}_p\right|_{avg}$) streamline velocities. The $\vec{u}$ profiles are normalized to these corresponding values and are accompanied by a reference vector which represents when $\frac{\vec{u}}{\left|\langle \vec{u}_p \rangle\right|_{avg}} = \frac{\vec{u}}{\left|\overline{\vec{u}}_p\right|_{avg}} = 1$. Every other index in the vector grid ($i = i + 1$) is skipped for all $\vec{v}$ and $\vec{u}$ fields for visual clarity. The color bar scales represent the spanwise vorticity strength for all $\vec{\omega}_z$ fields illustrated for a particular condition.

An experimental condition is classified as a propagating flow when the $\left|\langle \vec{u}_p \rangle\right|_{avg}$ and $\left|\overline{\vec{u}}_p\right|_{avg}$ are both positive and increasing in magnitude. This indicates that the flow generated in the wake is accelerating after several cycles. In the case of non-propagating flow, this pertains to a scenario where $0\ \mathrm{mm/s} \leq \left|\langle \vec{u}_p \rangle\right|_{avg} \leq 1\ \mathrm{mm/s}$ indicating that the bulk fluid is travelling at negligible velocity relative to the length of the channel. As for the case of reverse flow, this is a unique phenomenon where both $\left|\langle \vec{u}_p \rangle\right|_{avg}$ and $\left|\overline{\vec{u}}_p\right|_{avg}$ are negative and increasing in magnitude. The fluid in the wake is essentially accelerating in the streamwise but opposite direction (outlet to inlet).

4.2.1 Propagating Flow

The SEMA's flap deformations generate flow by efficient vortex production at the trailing edge and vortex convection downstream in the wake travelling from the channel's inlet to outlet. Evidence of forward streamwise flow for the experimental conditions is further supported by the velocity profiles in the time-averaged wakes. This resembles that of a coherent jet in the case shown in Figure 4.3A. After one flapping cycle, symmetric and oppositely signed vortices are evident. This vortex arrangement is also seen in both the phase-averaged and time-averaged wakes, one that is reminiscent of the von Karman vortex street. Figures 4.3B and C exhibit increasingly random and incoherent jets. This is possibly due to the vortices colliding with the rigid channel walls where they either dissipate rapidly into the fluid or detach into smaller, weaker vortices. There is also the appearance of numerous vortices within proximity of the walls (i.e., edge vortices) which suggests that these solid boundaries pose a significant effect on vortex development in the wake. Specifically in Figure 4.3B, the phase-averaged and time-averaged wakes demonstrate only a pair of symmetric, oppositely signed vortices that remain close to the flap's trailing edge. The lack of vortex convection in the flow may suggest a recirculating (or non-propagating) flow, however the corresponding velocity profiles showing a uniform and steady jet suggest otherwise. One plausible explanation for this is the rapid dissipation of fluid rotation due to wall or vortex-vortex interactions; fluid rotation may still be present but too weak to display a signature. Meanwhile, this vortex arrangement and uniform velocity profile may be the reason behind a steady streamwise velocity with little acceleration. The generated flow is more incoherent in the case of Figure 4.3C. Although, it seems as though the smaller vortices tend to dissipate and larger near-body vortices remain when observing the mean wake fields. The time-averaged wake specifically demonstrates two vortex structures and stretched vorticity regions (i.e., tongues) in a staggered pattern. Favourable energy from the SEMA's flapping is transferred to the wake and consequently accelerating the flow after several cycles in the time interval. The corresponding velocity profiles now resemble a non-uniform, axisymmetric jet. It can be said for all conditions mentioned here that flow generated either remains or stabilizes to a more coherent wake. This is similar to that reported by [52] and [54] in which the foil's flexibility is the primary mechanism for stabilization in the wakes, therefore it can be deduced here that this mechanism is being utilized by the SEMA pump membrane as well. Furthermore, favourable pressure gradients along a flexible flap due to periodic deformations promote the flow in the streamwise direction [54]. This mechanism can be contributing to the flow generated by the SEMA pump membrane and resulting in a propagating flow.

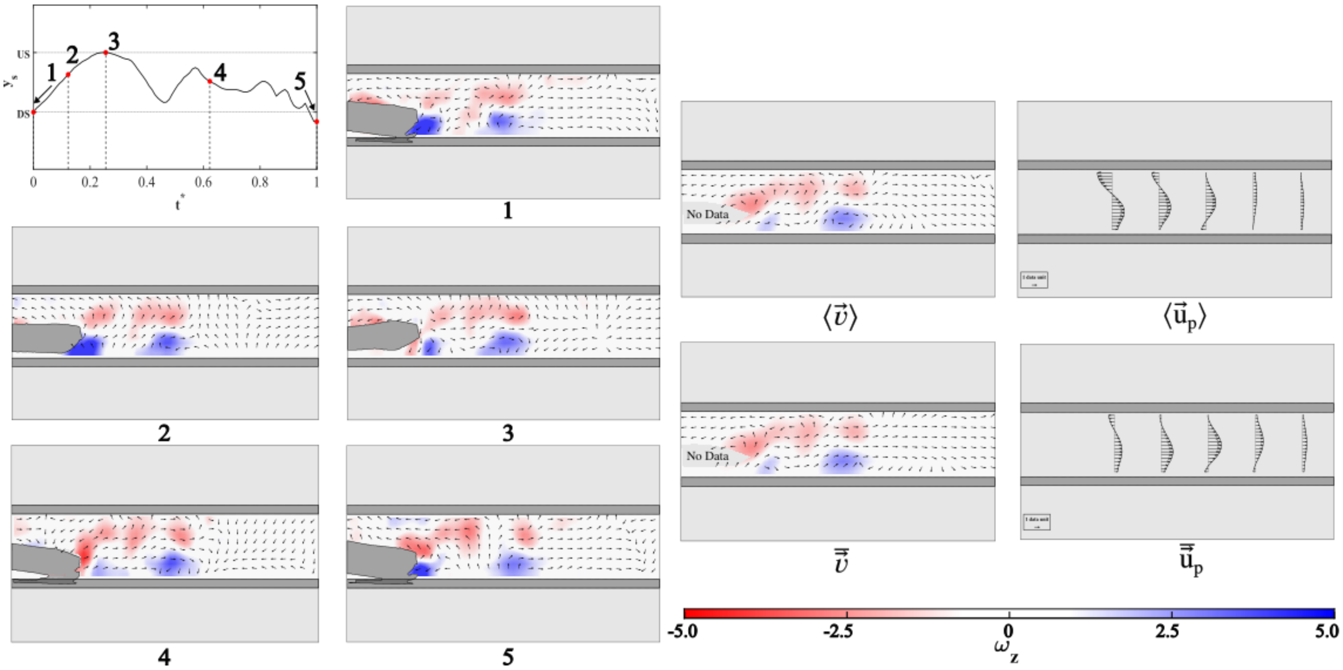

A) d15.5,I2,f3; $\left|\langle\vec{u}_p\rangle\right|_{avg} = 1.26\frac{mm}{s}, \left|\bar{\vec{u}}_p\right|_{avg} = 2.24\frac{mm}{s}$

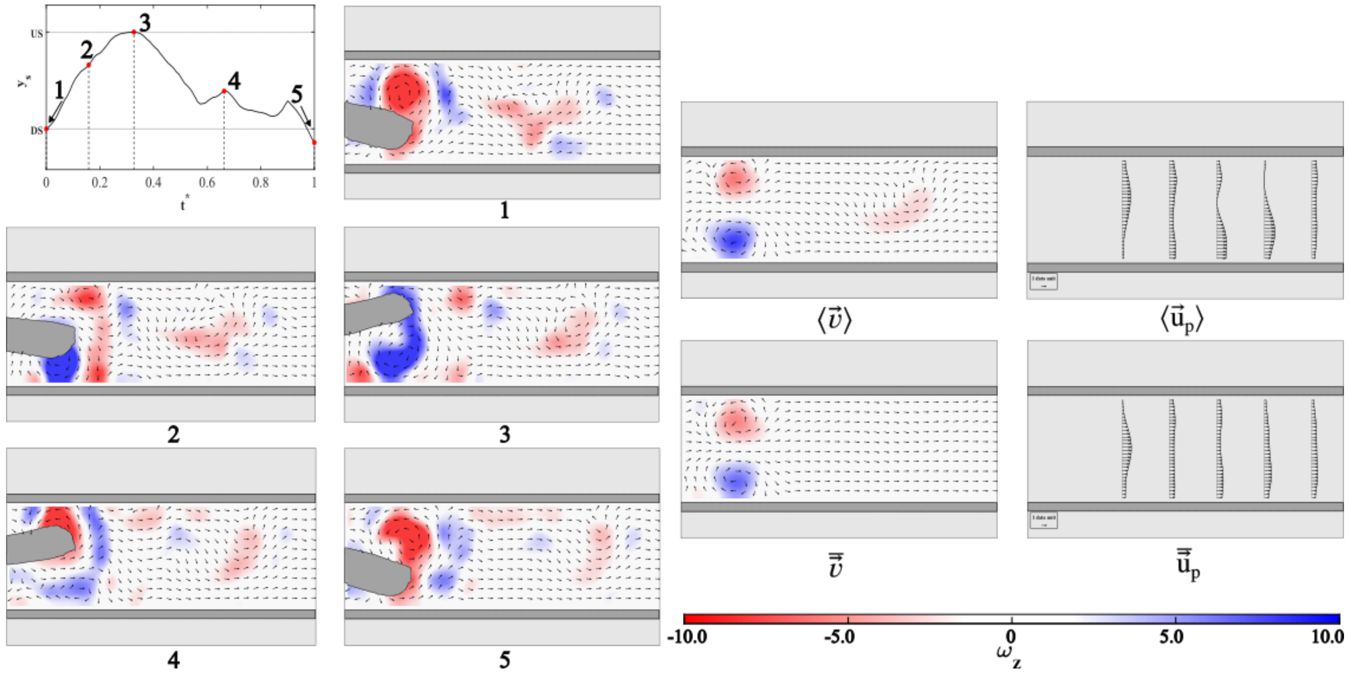

B) d25.5,I2,f1; $\left|\langle\vec{u}_p\rangle\right|_{avg} = 9.52\frac{mm}{s}, \left|\bar{\vec{u}}_p\right|_{avg} = 9.97\frac{mm}{s}$

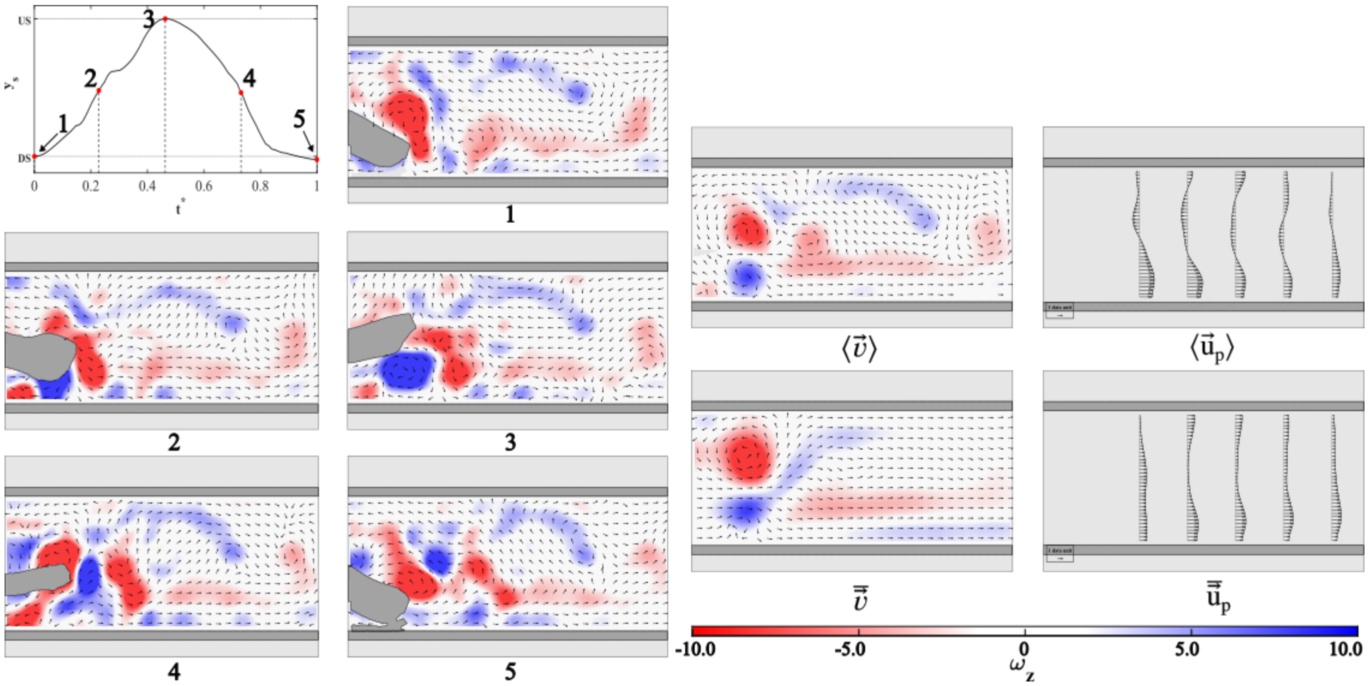

C) d31.5,I2,f2; $\left|\langle\vec{u}_p\rangle\right|_{avg} = 3.76\frac{mm}{s}$, $\left|\overline{\vec{u}}_p\right|_{avg} = 15.12\frac{mm}{s}$

Figure 4.3 Illustration of the 'propagating flow' case through selection of experimental conditions identified in A), B) and C). (Top Left) Flap tip position (y_s) as a function of dimensionless time (t^*) capturing the five significant points in one flapping cycle using the flap tip tracking in binary algorithm. The vortex and flapping dynamics are shown in the instantaneous $\vec{v}/\vec{\omega}_z$ fields at the corresponding instances (numbered 1 to 5) in the flapping cycle. The phase-averaged ($\langle\vec{v}\rangle$) and time-averaged ($\overline{\vec{v}}$) fields accompanied by their streamwise ($\vec{u}$) profiles show the flow direction and development. The reference vectors (1 data unit) located in the corner of $\vec{u}$ profile plots represent the mean magnitudes of the phase-averaged ($\left|\langle\vec{u}_p\rangle\right|_{avg}$) and time-averaged ($\left|\overline{\vec{u}}_p\right|_{avg}$) streamwise profiles respectively. The vorticity strength scale is applicable to all $\vec{\omega}_z$ colormaps.

4.2.2 Non-Propagating Flow

A prevalent observation in all experimental conditions for the non-propagating flow is the efficient vortex production but inefficient convection as a result of the SEMA's flapping. Large and strong vortices are created at each point in the cycle caused by the flap deformations and high velocity gradients in proximity to the walls. The shed vortices in a cycle are much weaker as they travel approximately one chord distance and dissipate completely past this location in the channel. This indicates a rapid decay rate of vorticity and momentum. This occurrence can be further supported by the resemblance of a 'momentumless' wake shown in the velocity profiles which is associated with drag production [93]. It is important to note that the former is reported for freely moving body in a freestream however, in the scenario of a constrained body in a quiescent fluid such as in this study, the momentumless wake is a result of the impeding flow. In the experimental conditions shown in Figure 4.4A and B, the instantaneous fields demonstrate a vortex arrangement similar to that of a von Karman vortex street which is also associated with drag production. Contrarily, Figure 4.4C shows a wake structure consisting of vortex pairs of alternating signs arranged above and below the SEMA. This same structure is observed in the time-averaged wakes of all conditions and is characterized by a CCW-CW vortex dipole closer upstream along the body followed by a CW-CCW dipole at the trailing edge. To the best of our knowledge, this structure has not been reported in the wake of flexible foils so we name this the 'mirror dipole'. The recirculating vortices of the mirror dipole likely impede the flow from convecting further downstream, therefore resulting in a non-propagating flow. Determination of the dominating factor for this flow behaviour is difficult, although it is probable that the actuation current plays a significant role as the deformation amplitudes are considerably smaller in these conditions than those in the previous case (see *Section 4.2.1*). This implies that the energy transferred to the fluid from the SEMA is not sufficient for generating a propagating flow.

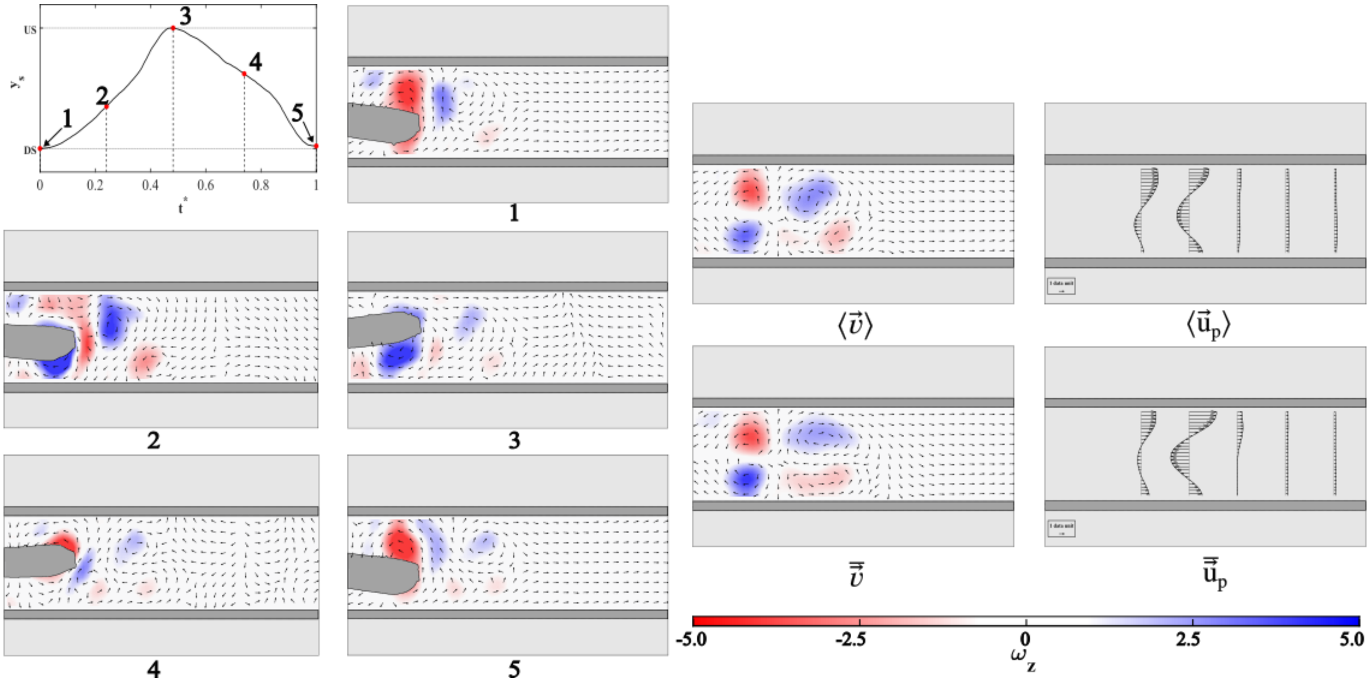

A) d22,I1,f1; $\left|\langle\vec{u}_p\rangle\right|_{avg} = 0.863\,\frac{mm}{s}, \left|\bar{\vec{u}}_p\right|_{avg} = 0.635\,\frac{mm}{s}$;

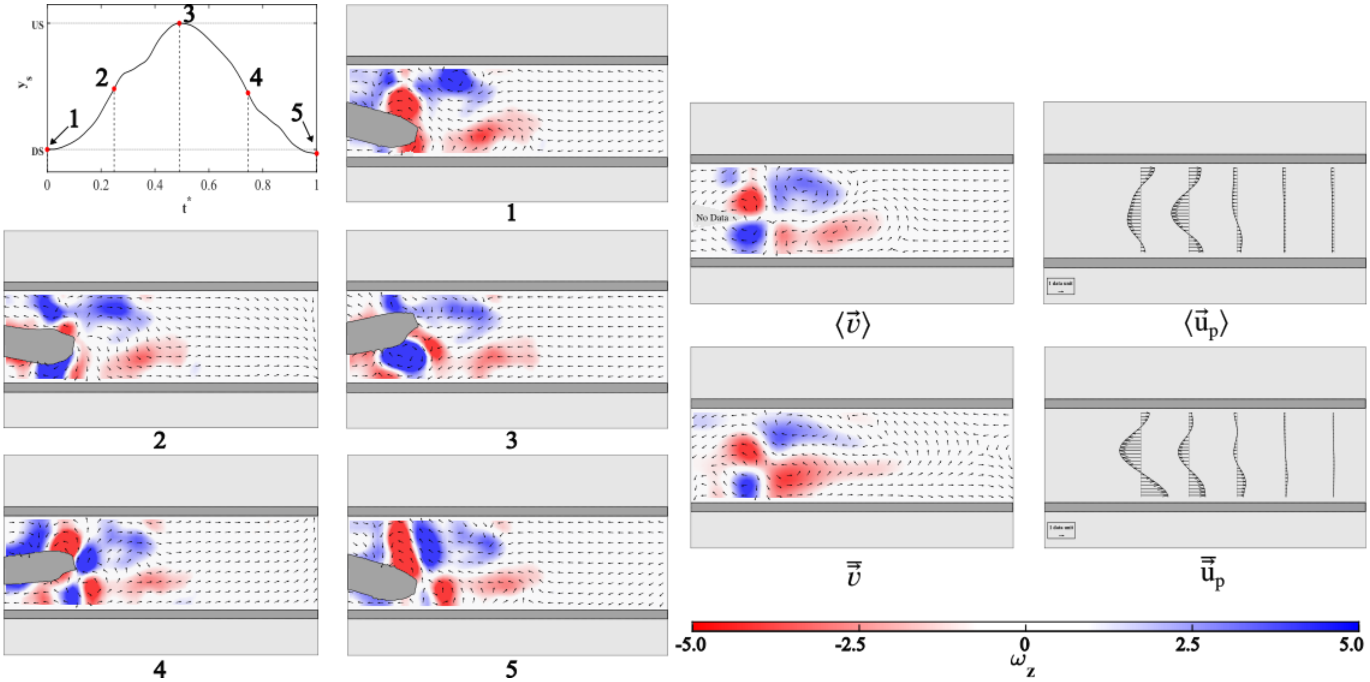

B) d22,I1,f2; $\left|\langle\vec{u}_p\rangle\right|_{avg} = -0.819\,\frac{mm}{s}, \left|\bar{\vec{u}}_p\right|_{avg} = 0.311\,\frac{mm}{s}$

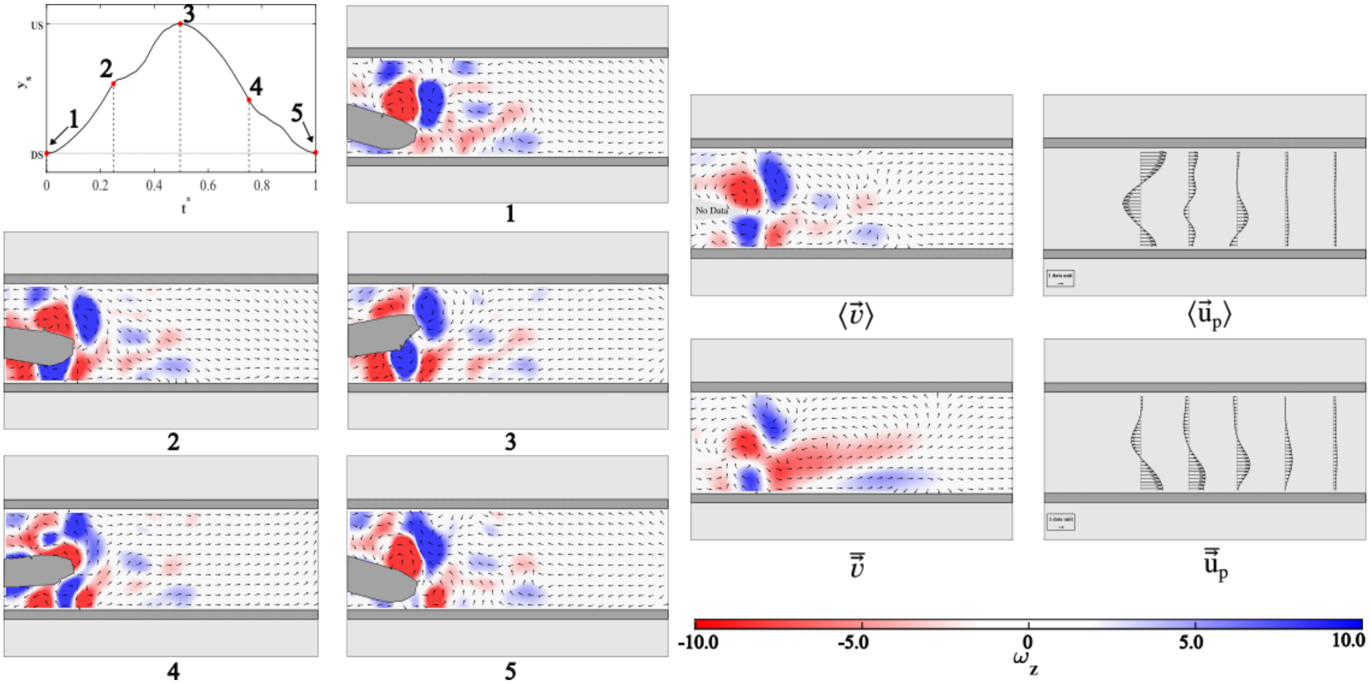

C) d24,I1,f2; $\left|\langle\vec{u}_p\rangle\right|_{avg} = 0.894\frac{mm}{s}, \left|\overline{\vec{u}}_p\right|_{avg} = 2.66\frac{mm}{s}$

Figure 4.4 Illustration of the ‘propagating flow’ case through selection of experimental conditions identified as A), B) and C). (Top Left) Flap tip position (y_s) as a function of dimensionless time (t^*) capturing the five significant points in one flapping cycle using the flap tip tracking in binary algorithm. The vortex and flapping dynamics are shown in the instantaneous $\vec{v}/\vec{\omega}_z$ fields at the corresponding instances (numbered 1 to 5) in the flapping cycle. The phase-averaged ($\langle\vec{v}\rangle$) and time-averaged ($\overline{\vec{v}}$) fields accompanied by their streamwise ($\vec{u}$) profiles show the flow direction and development. The reference vectors (1 data unit) located in the corner of $\vec{u}$ profile plots represent the mean magnitudes of the phase-averaged ($\left|\langle\vec{u}_p\rangle\right|_{avg}$) and time-averaged ($\left|\overline{\vec{u}}_p\right|_{avg}$) streamwise profiles respectively. The vorticity strength scale is applicable to all $\vec{\omega}_z$ colormaps.

4.2.3 Reverse Flow

This type of flow presents a unique behaviour that has not been previously reported. All conditions are characterized by strong vortices produced at or near the flap-fluid boundary further upstream from the trailing edge. Later in the cycle, it appears that this rotational energy is then transferred in the transverse direction to the walls where it is broken up into smaller vortices. The instantaneous $\vec{\omega}_z$ fields in Figure 4.5A to C demonstrate increasingly large vortex regions and affinity to the rigid walls. Edge vortices here are likely created due to the transverse velocity vector components fluctuating in sign from instances 1-5. Specifically in regions close to the walls high velocity gradients result in strong rotational energy, the strongest which is observed in the phase-averaged and time-averaged wakes in Figure 4.5C. Apart from edge vortices, weak and oppositely signed vortices at the trailing edge are identified in phase-averaged and time-averaged wakes with a re-appearance of a mirror dipole in the condition shown in Figure 4.5C. We postulate that this reverse flow can be explained according to the pressure gradient mechanism again by [54]. The contributions of I and f to flap kinematics, especially when f = 3 Hz, produce elevated pressures near the body as a result of the strong vortex development from SEMA deformations. Pressure accumulates in the region during the flapping cycle while the inlet and outlet are stably low-pressure regions. A pressure gradient will be formed and be directed towards the inlet as it is likely the more favourable path (i.e. shortest distance). This hypothesis is further supported by the directions of the streamwise $(-x)$ and transverse components of velocity vectors $(-y$ to $+y)$ coinciding with the direction of flapping (downstroke to upstroke) in all conditions. The flapping motion of the SEMA is essentially drawing in the fluid just downstream towards the inlet, where the pressure gradient grows and entrains the flow from fluid at the outlet location. The highly unsteady pressure regions during the cycle result in a quasi-steady pressure gradient in the averaged wakes. This likely explains the constant streamwise magnitudes and uniform velocity profiles.

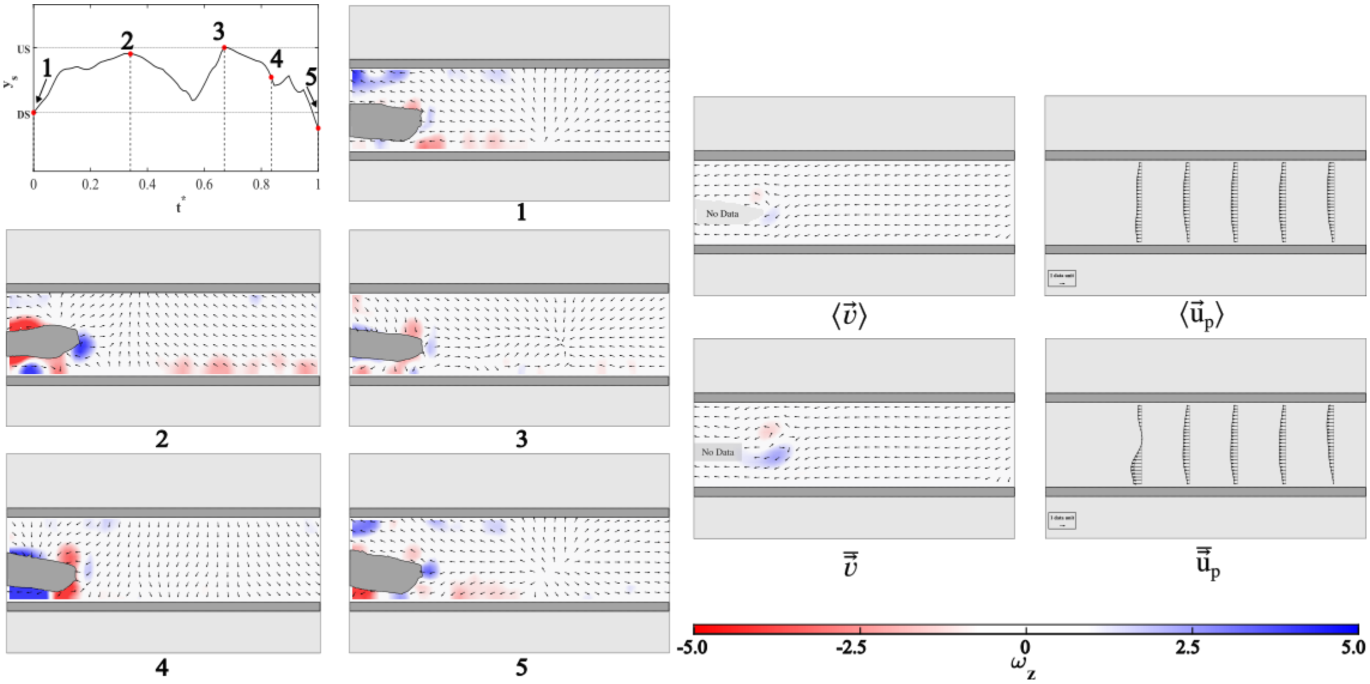

A) d20,I2,f3; $\left|\langle\vec{u}_p\rangle\right|_{avg} = -2.77\,\frac{mm}{s}, \left|\overline{\vec{u}}_p\right|_{avg} = -2.70\,\frac{mm}{s}$

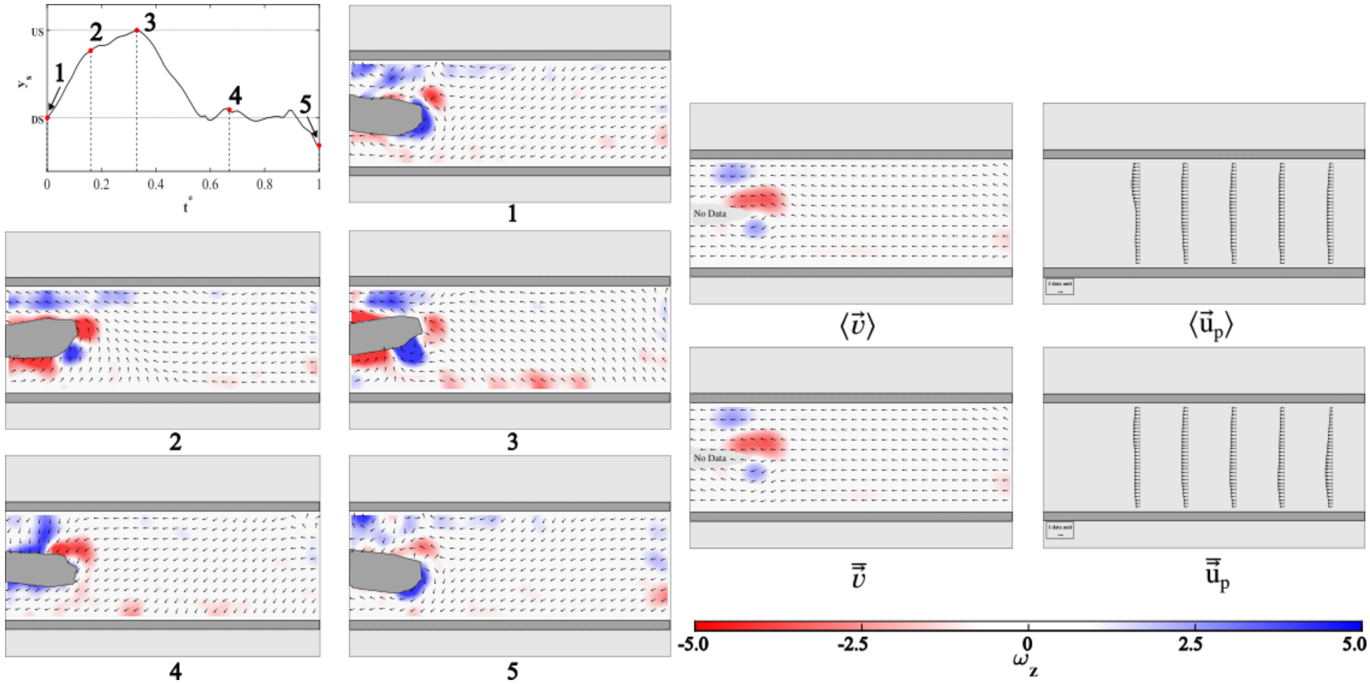

B) d25.5_I3_f3; $\left|\langle\vec{u}_p\rangle\right|_{avg} = -9.63\,\frac{mm}{s}, \left|\overline{\vec{u}}_p\right|_{avg} = -10.53\,\frac{mm}{s}$

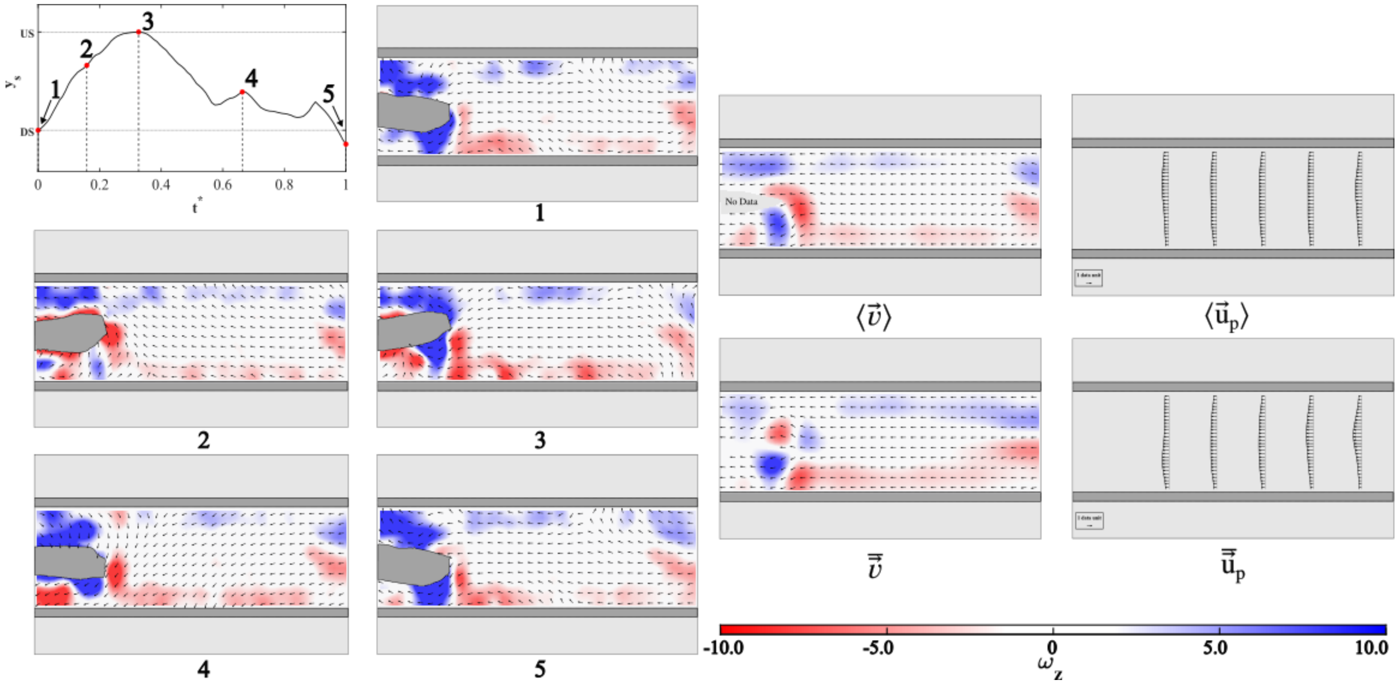

C) d24,I3,f3; $\left|\langle\vec{u}_p\rangle\right|_{avg} = -29.26\frac{mm}{s}$, $\left|\overline{\vec{u}}_p\right|_{avg} = -30.51\frac{mm}{s}$

Figure 4.5 Illustration of the 'propagating flow' case through selection of experimental conditions identified as A), B) and C). (Top Left) Flap tip position (y_s) as a function of dimensionless time (t^*) capturing the five significant points in one flapping cycle using the flap tip tracking in binary algorithm. The vortex and flapping dynamics are shown in the instantaneous $\vec{v}/\vec{\omega}_z$ fields at the corresponding instances (numbered 1 to 5) in the flapping cycle. The phase-averaged ($\langle\vec{v}\rangle$) and time-averaged ($\overline{\vec{v}}$) fields accompanied by their streamwise ($\vec{u}$) profiles show the flow direction and development. The reference vectors (1 data unit) located in the corner of $\vec{u}$ profile plots represent the mean magnitudes of the phase-averaged ($\left|\langle\vec{u}_p\rangle\right|_{avg}$) and time-averaged ($\left|\overline{\vec{u}}_p\right|_{avg}$) streamwise profiles respectively. The vorticity strength scale is applicable to all $\vec{\omega}_z$ colormaps.

4.3 General Observations

The flow generated from the flapping of a SEMA pump membrane is indeed the result of a highly unsteady fluid structure interaction, where the SEMA's flap deformations governed by *I* and *f* are solely responsible for the kinetic energy and momentum addition to the wake. These physics are closely related to the oscillating foil with flexible flap in a quiescent fluid [54]. The types of flows observed in this study are the product of the energy and momentum transfer due to the interactions. The influence of structural dynamics, freestream and solid boundaries on the overall wake is difficult to treat separately. The complex coupling of the SEMA and fluid interactions means that the variables are strongly intertwined. However, it is important to note that the reverse flow behaviour coincides well with $f = 3$ Hz. We therefore classify all 21 experimental conditions according to the three flow types observed and examine this system holistically in terms of its input variables (*d, I, f*) (see Figure 4.6). A 3D scatter plot was generated and a 2D view is shown here to evaluate the roles of actuation frequency and channel width on the wake behaviour.

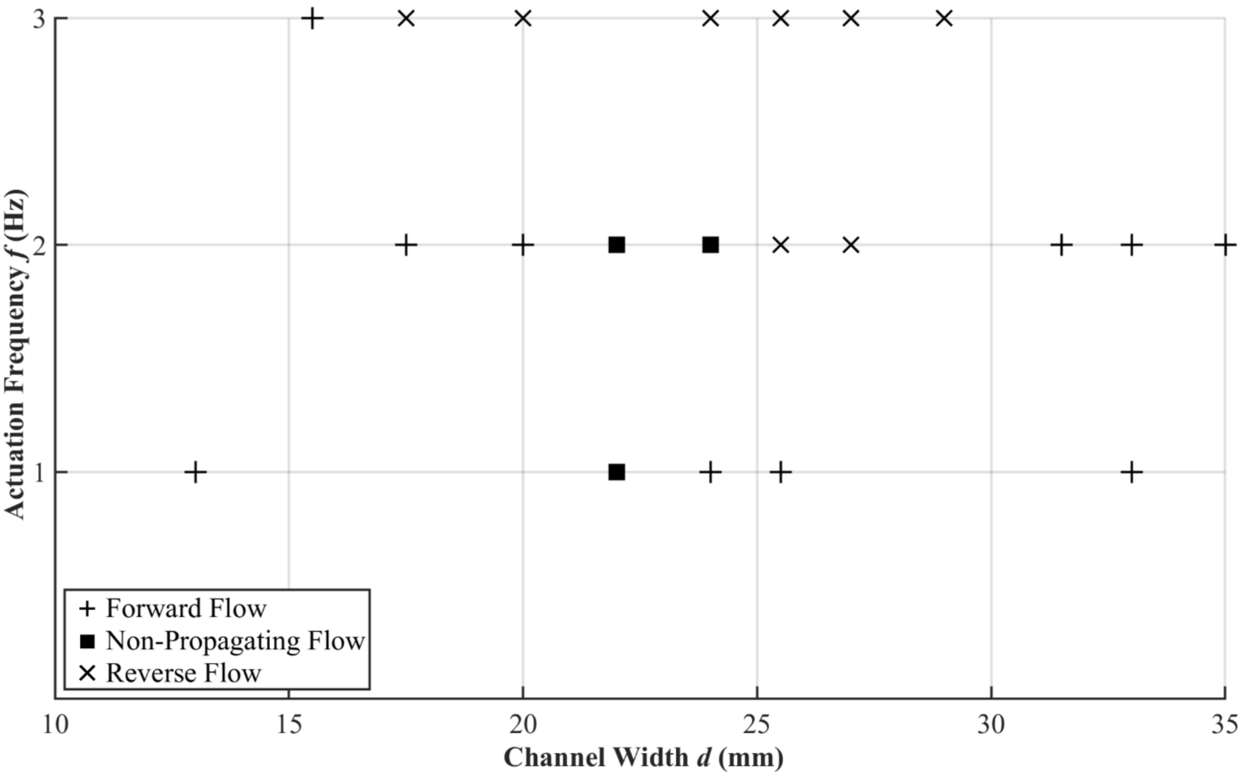

Figure 4.6 2D view of 3D scatter plot (*d* ,*I* ,*f*) illustrating the effects of actuation frequency *f* and channel width *d* on the flow behaviour.

Some noticeable patterns can be identified despite the discontinuities in the plot due to a reduced dataset. Propagating flow occurs primarily when $f \leq 2$ Hz at $d \leq 20$ mm and $d > 30$ mm and reverse flow when $f = 3$ Hz at 15 mm $< d < 30$ mm. Contrastly, non-propagating flow occurs for a narrow range of d values. It is evident from the plot that the reverse flow coincides with $f = 3$ Hz for five experimental conditions and $f = 2$ Hz for two other conditions, suggesting that actuation frequency may indeed be contributing significantly to the flow in the wake. The mechanism(s) causing this are unclear at this stage. We also observe a set of conditions for forward, non-propagating and reverse flows at $f = 2$ Hz. This indicates a possible transition to each flow regime and a 'critical state' may be occurring during this transition based on this actuation frequency. Furthermore, this may also imply the existence of more than one critical state but more data points would need to be collected to confirm this.

4.4 Limitations of Study

1) Illumination source for DPIV investigation. The implementation of an incandescent light instead of modern solutions such as high-powered lasers has some drawbacks in regard to optical precision which has been addressed in *Chapter* 3. Additionally, the intensity of light reflected from the seeding particles further upstream will not be entirely the same magnitude as those reflected downstream due to the low-powered light source. This can result in failure to detect or discard some particles as their light intensities are not satisfactory for image evaluation and validation. Reflection and dispersion of light also occurs at the SEMA flap as well, which resulted in a dilated shape and binary mask. During the flapping motion, light intensity changes and shadows are cast. It is for this reason that particles near the flap-fluid boundary led to spurious vectors. The use of high-powered lasers would yield a more uniform light scattering, FOV with negligible depth and finer spatial resolution. However, the material and flapping of the SEMA membrane would still produce undesirable lighting effects if kept the same. In this manner, some modifications are necessary if particles upstream from the flap and at the flap's boundary need to be evaluated.

2) Effect of free surface on DPIV image evaluation. The SEMA deformations not only affect the behaviour in the wake but also induce free surface deformations in the form of waves. We assume that the strength of these waves is negligible due to the low order of actuation forces (~mN), however any slight perturbation on the free surface will distort or alter the light intensity emitted from the particles. Intensity peaks may appear to be either stronger or weaker depending on the particle's elevation in relation to other neighbors which can increase correlation bias and uncertainty. The free surface also affects the distribution of seeding particles since they tend to agglomerate into bigger clusters due to surface tension [94]. This results in the need to increase the size of interrogation windows to accommodate the larger particle sizes, which in turn yields a coarser spatial resolution. These considerations are important for future studies examining the flow generated by a flapping SEMA in this configuration or alternative observations planes are to be used.

3) The wake is inherently 3-dimensional. As the header suggests, this study conducts a DPIV investigation in a 2D plane therefore the observed flow behaviour represents only a cross-section of the wake structure. Resolving the wake structure in 3 dimensions would require advanced methods such as volumetric PIV.

4) Longevity of liquid metal during operation. The duration of the experiments was relatively short (~15 seconds) when using a single SEMA pump sample as many samples were prone to failure, a phenomenon inherent in current-carrying LM coils known as electromigration.

5 CONCLUSION AND FUTURE WORKS

The study of flapping foils has been essential to the knowledge surrounding aquatic locomotion for many decades. This contribution has not only led to the discovery of distinct wake structures (e.g., von Karman and reversed von Karman) and locomotion mechanisms, but also the influence of many factors on the wake including foil flexibility, freestream and solid boundaries. Flexible flapping foils have been implemented in modern studies as they demonstrate fascinating wake behaviour that is useful in applications such as energy harvesting, biomimetic fish and pumping. The use of a flexible flapping foil as a fluid pump in literature is very scarce, in which only a few numerical studies highlighting a novel left ventricle assist device (CorWave™) based on an undulating membrane is available. Advancements in technology have also shown the potential for smart material-based actuators especially in fluid-based applications. It is therefore in this study where we attempt to bridge the gap between smart actuators and flexible flapping foils by incorporating a SEMA within a fully flexible membrane inspired by the CorWave's design. We also attempt to observe the suitability of a flexible flapping foil-generated flow in a fluid (water) by uncovering the flow physics in the wake and connecting them to those reported in the literature. Specifically, we are interested in the flow generated by a fully flexible, smart actuator-enabled flapping foil within an otherwise quiescent (no freestream) fluid. A SEMA membrane prototype was designed using a modified fabrication process relative to the original actuator [7]. In the same manner, a custom control system based on a simple microcontroller and integrated MOSFET driver was responsible for the prototype's deformations. Characterization tests were conducted to evaluate the relationship between deformation amplitude and electrical resistance. The tests yielded a stable mean resistance across all (I, f) combinations which demonstrated relatively good performance but larger fluctuations as compared to the original [7]. Analysis of the flow generated in the wake is conducted using a flow visualization assembly based on DPIV. The SEMA membrane prototype was placed in an acrylic tank at the fluid's free surface where the deformations occur along the chord's axis. A 3D-printed wall mechanism was placed symmetrically about the SEMA and used to vary the channel width (d) for an open channel flow. The SEMA and fluid interactions were captured using a high-speed camera (300 fps) with microscopic particles for different experimental conditions (d, I, f). Flow information in the wake was estimated from a complete DPIV analysis conducted in an open-source, GUI-based MATLAB tool (PIVLab v3.01). We later examine the wake behaviour according to the instantaneous, phase-averaged (one cycle) and time-averaged (time interval) $\vec{v}/\vec{\omega}_z$ fields with corresponding $\vec{u}$ velocity profiles. The DPIV investigation revealed three types of flow cases: 1) propagating, 2) non-propagating and 3) reverse flow. Similar characteristics were identified for the experimental conditions exhibiting each flow type. Efficient vortex production at the SEMA's flap and vortex convection at the trailing edge occur at the stages of the flapping cycle in the case of a propagating flow. This can be likely due to a favourable pressure gradient created by the flapping motion promotes streamwise flow like in [54]. Stability is achieved over time as shown in the phase-averaged and time-averaged wakes. Additionally, we observe some conditions in this flow type exhibiting a vortex arrangement that is similar to the reversed von Karman vortex street. In the case of non-propagating flow, all conditions demonstrate an arrangement of recirculating vortices at the trailing edge that we name the 'mirror dipole'. This effectively creates a recirculating flow that does not produce sufficient energy to travel downstream. Finally, we observe a reverse (outlet to inlet) streamwise flow which has not been reported before for a flexible foil flapping in a quiescent medium. Flow velocity fluctuates in sign transversely throughout the flapping cycle, creating edge vortices due to high velocity gradients near the rigid walls. The reverse flow behaviour can likely be explained by a pressure gradient directing the flow from the SEMA body and flap towards the inlet, allowing the flow to uniformly move in reverse. The reverse flow seems to coincide well with $f = 3$ Hz and a 2D view of a 3D plot (d , I ,f) of all test conditions supports this. The plot also shows the occurrence of all three flow types at $f = 2$ Hz, suggesting a transition in flow regimes and the possible existence of one or more 'critical' states.

The three types of flows generated by a SEMA-enabled flapping membrane and the underlying physics are revealed in the wake characteristics. Future studies can expand on the knowledge obtained in this study, specifically in determining the contributions of the SEMA dynamics and environmental factors (i.e., freestream and solid boundaries). A larger dataset would need to be constructed with finer resolution of data points (e.g., $\Delta f = 0.5\text{ Hz}, \Delta I = 0.5\text{ A}$) for a better qualitative assessment. In terms of a quantitative assessment, a possible approach may be a thorough structural analysis of the SEMA pump membrane. A numerical and/or experimental study of the deformations over a wide frequency spectrum can help identify natural frequencies and harmonics. Additionally, the effects of the actuation frequencies and currents on the deformation profiles may uncover detailed flapping characteristics (e.g., nonlinear, periodic, chaotic, bimodal, etc.). These observations can help establish possible links to instantaneous/averaged flow fields and address particular structures in the wake. These approaches show the potential for optimization of a SEMA-enabled flapping membrane. Furthermore, the SEMA is easily scalable to one or several flapping membranes where other configurations may yield desirable velocity gradients for pumping like in the CorWave. This fundamental study provides a fascinating introduction to the capabilities of a SEMA-enabled flapping membrane in the field of fluid dynamics. This study also provides particular insights into the emerging designs for pumping devices such as the CorWave pump for cardiovascular support.

REFERENCES

[1] G. M. Whitesides, "Soft Robotics," *Angewandte Chemie International Edition,* vol. 57, no. 16, pp. 4258-4273, 2018/04/09 2018, doi: https://doi.org/10.1002/anie.201800907.

[2] T. J. Wallin, J. Pikul, and R. F. Shepherd, "3D printing of soft robotic systems," *Nature Reviews Materials,* vol. 3, no. 6, pp. 84-100, 2018/06/01 2018, doi: 10.1038/s41578-018-0002-2.

[3] J. Z. Gul *et al.*, "3D printing for soft robotics – a review," *Science and Technology of Advanced Materials,* vol. 19, no. 1, pp. 243-262, 2018/12/31 2018, doi: 10.1080/14686996.2018.1431862.

[4] H. K. Balakrishnan *et al.*, "3D printing: an alternative microfabrication approach with unprecedented opportunities in design," *Analytical Chemistry,* vol. 93, no. 1, pp. 350-366, 2021/01/12 2021, doi: 10.1021/acs.analchem.0c04672.

[5] M. Enyan, Z. Bing, J. N. O. Amu-Darko, E. Issaka, S. L. Otoo, and M. F. Agyemang, "Advances in smart materials soft actuators on mechanisms, fabrication, materials, and multifaceted applications: A review," *Journal of Thermoplastic Composite Materials,* p. 08927057241248028, 2024, doi: 10.1177/08927057241248028.

[6] G. Mao *et al.*, "Ultrafast small-scale soft electromagnetic robots," *Nature Communications,* vol. 13, no. 1, p. 4456, 2022/08/09 2022, doi: 10.1038/s41467-022-32123-4.

[7] G. Mao *et al.*, "Soft electromagnetic actuators," *Science Advances,* vol. 6, no. 26, p. eabc0251, 2020, doi: 10.1126/sciadv.abc0251.

[8] T. N. Do, H. Phan, T.-Q. Nguyen, and Y. Visell, "Miniature soft electromagnetic actuators for robotic applications," *Advanced Functional Materials,* vol. 28, no. 18, p. 1800244, 2018/05/01 2018, doi: https://doi.org/10.1002/adfm.201800244.

[9] M. Li, A. Pal, A. Aghakhani, A. Pena-Francesch, and M. Sitti, "Soft actuators for real-world applications," *Nature Reviews Materials,* vol. 7, no. 3, pp. 235-249, 2022/03/01 2022, doi: 10.1038/s41578-021-00389-7.

[10] Z. Ma and D. Sameoto, "A review of electrically driven soft actuators for soft robotics," *Micromachines*, vol. 13, no. 11, doi: 10.3390/mi13111881.

[11] N. El-Atab *et al.*, "Soft actuators for soft robotic applications: A Review," *Advanced Intelligent Systems,* vol. 2, no. 10, p. 2000128, 2020/10/01 2020, doi: https://doi.org/10.1002/aisy.202000128.

[12] N. Bira, P. Dhagat, and J. R. Davidson, "A review of magnetic elastomers and their role in soft robotics," *Frontiers in Robotics and AI,* Review vol. 7, 2020. [Online]. Available: https://www.frontiersin.org/articles/10.3389/frobt.2020.588391.

[13] S. Chen, H.-Z. Wang, T.-Y. Liu, and J. Liu, "Liquid metal smart materials toward soft robotics," *Advanced Intelligent Systems,* vol. 5, no. 8, p. 2200375, 2023/08/01 2023, doi: https://doi.org/10.1002/aisy.202200375.

[14] S. Chen, Z. Cui, H. Wang, X. Wang, and J. Liu, "Liquid metal flexible electronics: Past, present, and future," *Applied Physics Reviews,* vol. 10, no. 2, p. 021308, 2023, doi: 10.1063/5.0140629.

[15] J. Ma, F. Krisnadi, M. H. Vong, M. Kong, O. M. Awartani, and M. D. Dickey, "Shaping a soft future: patterning liquid metals," *Advanced Materials,* vol. 35, no. 19, p. 2205196, 2023/05/01 2023, doi: https://doi.org/10.1002/adma.202205196.

[16] S. W. Jin *et al.*, "Stretchable loudspeaker using liquid metal microchannel," *Scientific Reports,* vol. 5, no. 1, p. 11695, 2015/07/16 2015, doi: 10.1038/srep11695.

[17] V. Bharambe, D. P. Parekh, C. Ladd, K. Moussa, M. D. Dickey, and J. J. Adams, "Vacuum-filling of liquid metals for 3D printed RF antennas," *Additive Manufacturing,* vol. 18, pp. 221-227, 2017/12/01/ 2017, doi: https://doi.org/10.1016/j.addma.2017.10.012.

[18] L. Teng, L. Zhu, S. Handschuh-Wang, and X. Zhou, "Robust, multiscale liquid-metal patterning enabled by a sacrificial sealing layer for flexible and wearable wireless powering," *Journal of Materials Chemistry C,* 10.1039/C9TC04876F vol. 7, no. 48, pp. 15243-15251, 2019, doi: 10.1039/C9TC04876F.

[19] T. Cole, K. Khoshmanesh, and S.-Y. Tang, "Liquid metal enabled biodevices," *Advanced Intelligent Systems,* vol. 3, no. 7, p. 2000275, 2021/07/01 2021, doi: 10.1002/aisy.202000275.

[20] X. Zhang, J. Ai, Y. Yue, Y. Shi, R. Zou, and B. Su, "Anti-stress ball energy harvester," *Nano Energy,* vol. 90, p. 106493, 2021/12/01/ 2021, doi: https://doi.org/10.1016/j.nanoen.2021.106493.

[21] X. Zhang, J. Ai, R. Zou, and B. Su, "Compressible and stretchable magnetoelectric sensors based on liquid metals for highly sensitive, self-powered respiratory monitoring," *ACS Applied Materials & Interfaces,* vol. 13, no. 13, pp. 15727-15737, 2021/04/07 2021, doi: 10.1021/acsami.1c04457.

[22] X. Zhang *et al.*, "Magnetoelectric soft composites with a self-powered tactile sensing capacity," *Nano Energy,* vol. 69, p. 104391, 2020/03/01/ 2020, doi: https://doi.org/10.1016/j.nanoen.2019.104391.

[23] S. Guo *et al.*, "Flexible liquid metal coil prepared for electromagnetic energy harvesting and wireless charging," *Frontiers in Energy,* vol. 13, no. 3, pp. 474-482, 2019/09/01 2019, doi: 10.1007/s11708-019-0632-0.

[24] R. P. Feynman, R. B. Leighton, and M. L. Sands, *1-1 Electrical forces*, New millennium edition ed. New York: Basic Books, 2010. [Online]. Available: http://site.ebrary.com/id/10753917.

[25] R. P. Feynman, R. B. Leighton, and M. L. Sands, *1-4 The laws of electromagnetism*, New millennium edition ed. New York: Basic Books, 2010. [Online]. Available: http://site.ebrary.com/id/10753917.

[26] R. P. Feynman, R. B. Leighton, and M. L. Sands, *13-4 The magnetic field of steady currents; Ampère's law*, New millennium edition ed. New York: Basic Books, 2010. [Online]. Available: http://site.ebrary.com/id/10753917.

[27] D. Bach, F. Schmich, T. Masselter, and T. Speck, "A review of selected pumping systems in nature and engineering—potential biomimetic concepts for improving displacement pumps and pulsation damping," *Bioinspiration & Biomimetics,* vol. 10, no. 5, p. 051001, 2015/09/03 2015, doi: 10.1088/1748-3190/10/5/051001.

[28] H. Sun, J. Zhao, Y. Zhang, and M. Xu, "Flexible pump for small-scale soft robotics: actuation, design and prospects," *Measurement,* vol. 237, p. 115299, 2024/09/30/ 2024, doi: https://doi.org/10.1016/j.measurement.2024.115299.

[29] E. A. Sideris, H. C. de Lange, U. Johanson, and T. Tamm, "Solid-state electromechanical Smart material actuators for pumps—A Review," *Actuators*, vol. 13, no. 7, doi: 10.3390/act13070232.

[30] E. A. Sideris and H. C. de Lange, "Pumps operated by solid-state electromechanical smart material actuators - A review," *Sensors and Actuators A: Physical,* vol. 307, p. 111915, 2020/06/01/ 2020, doi: https://doi.org/10.1016/j.sna.2020.111915.

[31] C. Botterbusch, T. Snyder, P.-P. Monticone, L. de Lillers, A. Schmidt, and C. Rasser, "CorWave LVAD: insight into device concept and stage of development," in *Mechanical Support for Heart Failure : Current Solutions and New Technologies*, J. H. Karimov, K. Fukamachi, and R. C. Starling Eds. Cham: Springer International Publishing, 2020, pp. 587-597.
[32] "What is Heart Failure?," (in en), *www.heart.org*. [Online]. Available: https://www.heart.org/en/health-topics/heart-failure/what-is-heart-failure.
[33] "Heart failure - Diagnosis and treatment - Mayo Clinic," ed.
[34] M. Martinolli, J. Biasetti, S. Zonca, L. Polverelli, and C. Vergara, "Extended finite element method for fluid-structure interaction in wave membrane blood pump," *International Journal for Numerical Methods in Biomedical Engineering,* vol. 37, no. 7, p. e3467, 2021/07/01 2021, doi: https://doi.org/10.1002/cnm.3467.
[35] M. Martinolli, F. Cornat, and C. Vergara, "Computational fluid–structure interaction study of a new wave membrane blood pump," *Cardiovascular Engineering and Technology,* vol. 13, no. 3, pp. 373-392, 2022/06/01 2022, doi: 10.1007/s13239-021-00584-1.
[36] T. A. Snyder *et al.*, "The CorWave LVAD - synchronized pulsatility with improved hemodynamics," *The Journal of Heart and Lung Transplantation,* vol. 41, no. 4, p. S103, 2022, doi: 10.1016/j.healun.2022.01.240.
[37] C. Botterbusch *et al.*, "Acute and chronic pre-clinical implants of the CorWave LVAD: hydraulic, hemocompatibility and hemodynamic Results," *The Journal of Heart and Lung Transplantation,* vol. 39, no. 4, Supplement, p. S190, 2020/04/01/ 2020, doi: https://doi.org/10.1016/j.healun.2020.01.781.
[38] A. J. Smits, "Undulatory and oscillatory swimming," *Journal of Fluid Mechanics,* vol. 874, p. P1, 2019, Art no. P1, doi: 10.1017/jfm.2019.284.
[39] G. V. Lauder, "Fish locomotion: recent advances and new directions," (in eng), *Ann Rev Mar Sci,* vol. 7, pp. 521-45, 2015, doi: 10.1146/annurev-marine-010814-015614.
[40] F. E. Fish and G. V. Lauder, "Passive and active flow control by swimming fishes and mammals," *Annual Review of Fluid Mechanics,* vol. 38, no. Volume 38, 2006, pp. 193-224, 2006, doi: https://doi.org/10.1146/annurev.fluid.38.050304.092201.
[41] M. S. Triantafyllou, F. S. Hover, A. H. Techet, and D. K. P. Yue, "Review of hydrodynamic scaling laws in aquatic locomotion and fishlike swimming," *Applied Mechanics Reviews,* vol. 58, no. 4, pp. 226-237, 2005, doi: 10.1115/1.1943433.
[42] M. S. Triantafyllou, A. H. Techet, and F. S. Hover, "Review of experimental work in biomimetic foils," *IEEE Journal of Oceanic Engineering,* vol. 29, no. 3, pp. 585-594, 2004, doi: 10.1109/JOE.2004.833216.
[43] T. Van Buren, D. Floryan, N. Wei, and A. J. Smits, "Flow speed has little impact on propulsive characteristics of oscillating foils," *Physical Review Fluids,* vol. 3, no. 1, p. 013103, 01/30/ 2018, doi: 10.1103/PhysRevFluids.3.013103.
[44] S. Shukla, A. Sharma, A. Agrawal, and R. Bhardwaj, "Fish-inspired oscillating and/or undulating hydrofoil in a free stream flow: a review on thrust generation mechanisms," *Journal of the Indian Institute of Science,* vol. 104, no. 1, pp. 147-179, 2024/01/01 2024, doi: 10.1007/s41745-024-00426-8.
[45] R. Godoy-Diana, J.-L. Aider, and J. E. Wesfreid, "Transitions in the wake of a flapping foil," *Physical Review E,* vol. 77, no. 1, p. 016308, 01/24/ 2008, doi: 10.1103/PhysRevE.77.016308.

[46] D. G. Bohl and M. M. Koochesfahani, "MTV measurements of the vortical field in the wake of an airfoil oscillating at high reduced frequency," *Journal of Fluid Mechanics,* vol. 620, pp. 63-88, 2009, doi: 10.1017/S0022112008004734.

[47] T. Schnipper, A. Andersen, and T. Bohr, "Vortex wakes of a flapping foil," *Journal of Fluid Mechanics,* vol. 633, pp. 411-423, 2009, doi: 10.1017/S0022112009007964.

[48] J. C. S. Lai and M. F. Platzer, "Jet Characteristics of a Plunging Airfoil," *AIAA Journal,* vol. 37, no. 12, pp. 1529-1537, 1999/12/01 1999, doi: 10.2514/2.641.

[49] M. A. Ashraf, J. Young, and J. C. S. Lai, "Oscillation frequency and amplitude effects on plunging airfoil propulsion and flow periodicity," *AIAA Journal,* vol. 50, no. 11, pp. 2308-2324, 2012/11/01 2012, doi: 10.2514/1.J051374.

[50] F. Paraz, L. Schouveiler, and C. Eloy, "Thrust generation by a heaving flexible foil: Resonance, nonlinearities, and optimality," *Physics of Fluids,* vol. 28, no. 1, p. 011903, 2016, doi: 10.1063/1.4939499.

[51] C. Marais, B. Thiria, J. E. Wesfreid, and R. Godoy-Diana, "Stabilizing effect of flexibility in the wake of a flapping foil," *Journal of Fluid Mechanics,* vol. 710, pp. 659-669, 2012, doi: 10.1017/jfm.2012.390.

[52] J. H. Arakeri and S. Y. Shinde, "Flexibility in flapping foil suppresses meandering of induced jet in absence of free stream," *Journal of Fluid Mechanics,* vol. 757, pp. 231-250, 2014, doi: 10.1017/jfm.2014.480.

[53] P. Deshpande and A. Vishwasrao, "Kinematics and dynamics of pitching flexible panels in a quiescent fluid," *Journal of Fluid Mechanics,* vol. 922, p. A13, 2021, Art no. A13, doi: 10.1017/jfm.2021.494.

[54] S. Y. Shinde and J. H. Arakeri, "Physics of unsteady thrust and flow generation by a flexible surface flapping in the absence of a free stream," *Proceedings of the Royal Society A: Mathematical, Physical and Engineering Sciences,* vol. 474, no. 2218, p. 20180519, 2018/10/31 2018, doi: 10.1098/rspa.2018.0519.

[55] S. Y. Shinde, "Creation of an orderly jet and thrust generation in quiescent fluid from an oscillating two-dimensional flexible foil," PhD. Thesis, Indian Institute of Science, Bangalore, India, 2018.

[56] F. J. Huera-Huarte, "Pitching foil propulsion performance decays near the free surface," *Ocean Engineering,* vol. 272, p. 113663, 2023/03/15/ 2023, doi: https://doi.org/10.1016/j.oceaneng.2023.113663.

[57] J.-T. Zhang and T. Nakamura, "Propulsive performance of a heaving and pitching foil with large amplitudes in unsteady ground effect," *Fluid Dynamics Research,* vol. 56, no. 4, p. 045503, 2024/07/25 2024, doi: 10.1088/1873-7005/ad628a.

[58] T. Han, Q. Zhong, A. Mivehchi, D. B. Quinn, and K. W. Moored, "Revealing the mechanism and scaling laws behind equilibrium altitudes of near-ground pitching hydrofoils," *Journal of Fluid Mechanics,* vol. 978, p. A5, 2024, Art no. A5, doi: 10.1017/jfm.2023.1004.

[59] D. B. Quinn, K. W. Moored, P. A. Dewey, and A. J. Smits, "Unsteady propulsion near a solid boundary," *Journal of Fluid Mechanics,* vol. 742, pp. 152-170, 2014, doi: 10.1017/jfm.2013.659.

[60] Q. Xiao and Q. Zhu, "A review on flow energy harvesters based on flapping foils," *Journal of Fluids and Structures,* vol. 46, pp. 174-191, 2014/04/01/ 2014, doi: https://doi.org/10.1016/j.jfluidstructs.2014.01.002.

[61] Q. Zhong *et al.*, "Tunable stiffness enables fast and efficient swimming in fish-like robots," *Science Robotics,* vol. 6, no. 57, p. eabe4088, 2021/08/11 2021, doi: 10.1126/scirobotics.abe4088.

[62] H. Meng *et al.*, "Cantilever-based micro thrust measurement and pressure field distribution of biomimetic robot fish actuated by macro fiber composites (MFCs) actuators," *Smart Materials and Structures,* vol. 30, no. 3, p. 035001, 2021/01/29 2021, doi: 10.1088/1361-665X/abdaa9.

[63] D. Wei *et al.*, "A magnetically actuated miniature robotic fish with the flexible tail fin," *IEEE Robotics and Automation Letters,* vol. 8, no. 10, pp. 6099-6106, 2023, doi: 10.1109/LRA.2023.3300283.

[64] M. Mohaghar, A. A. Connor, S. Wu, R. R. Zhao, and D. R. Webster, "Effects of symmetry-breaking mechanisms on the flow field around magnetic-responsive material appendages that mimic swimming strokes," *Physical Review Fluids,* vol. 9, no. 2, p. 023101, 02/13/ 2024, doi: 10.1103/PhysRevFluids.9.023101.

[65] "Amplified Piezoelectric Actuators, 220 µm to 2500 µm Travel," (in en). [Online]. Available: https://www.thorlabs.com.

[66] S. Bodkhe and P. Ermanni, "Challenges in 3D printing of piezoelectric materials," *Multifunctional Materials,* vol. 2, no. 2, p. 022001, 2019/03/27 2019, doi: 10.1088/2399-7532/ab0c41.

[67] "Ecoflex™ 00-30 Product Information," (in en), *Smooth-On, Inc.* [Online]. Available: https://www.smooth-on.com/products/ecoflex-00-30/.

[68] G. Jin *et al.*, "Bioinspired soft caterpillar robot with ultra-stretchable bionic sensors based on functional liquid metal," *Nano Energy,* vol. 84, p. 105896, 2021/06/01/ 2021, doi: https://doi.org/10.1016/j.nanoen.2021.105896.

[69] R. Guo, L. Sheng, H. Gong, and J. Liu, "Liquid metal spiral coil enabled soft electromagnetic actuator," *Science China Technological Sciences,* vol. 61, no. 4, pp. 516-521, 2018/04/01 2018, doi: 10.1007/s11431-017-9063-2.

[70] Y. Lin, O. Gordon, M. R. Khan, N. Vasquez, J. Genzer, and M. D. Dickey, "Vacuum filling of complex microchannels with liquid metal," *Lab on a Chip,* 10.1039/C7LC00426E vol. 17, no. 18, pp. 3043-3050, 2017, doi: 10.1039/C7LC00426E.

[71] Y. Xia and G. M. Whitesides, "Soft Lithography," (in eng), *Annual Review of Materials Science,* vol. 28, pp. 153-184, 1998.

[72] D. Therriault, R. F. Shepherd, S. R. White, and J. A. Lewis, "Fugitive inks for direct-write assembly of three-dimensional microvascular networks," *Advanced Materials,* vol. 17, no. 4, pp. 395-399, 2005/02/23 2005, doi: https://doi.org/10.1002/adma.200400481.

[73] V. Saggiomo and A. H. Velders, "Simple 3D printed scaffold-removal method for the fabrication of intricate microfluidic devices," *Advanced Science,* vol. 2, no. 9, p. 1500125, 2015/09/01 2015, doi: https://doi.org/10.1002/advs.201500125.

[74] J.-H. Low, P.-S. Chee, E.-H. Lim, and V. Ganesan, "Design of a wireless smart insole using stretchable microfluidic sensor for gait monitoring," *Smart Materials and Structures,* vol. 29, no. 6, p. 065003, 2020/04/28 2020, doi: 10.1088/1361-665X/ab802c.

[75] M. Cesaria, V. Arima, M. G. Manera, and R. Rella, "Protocol of thermal aging against the swelling of poly(dimethylsiloxane) and physical insight in swelling regimes," *Polymer,* vol. 139, pp. 145-154, 2018/03/14/ 2018, doi: https://doi.org/10.1016/j.polymer.2018.02.022.

[76] M. Cesaria, V. Arima, M. G. Manera, and R. Rella, "Practical strategy to realistically measure the swelling ratio of poly(dimethylsiloxane) without underestimation due to the

solvent volatility," *Polymer,* vol. 113, pp. 187-192, 2017/03/24/ 2017, doi: https://doi.org/10.1016/j.polymer.2017.02.049.

[77] C. V. Rumens, M. A. Ziai, K. E. Belsey, J. C. Batchelor, and S. J. Holder, "Swelling of PDMS networks in solvent vapours; applications for passive RFID wireless sensors," *Journal of Materials Chemistry C,* 10.1039/C5TC01927C vol. 3, no. 39, pp. 10091-10098, 2015, doi: 10.1039/C5TC01927C.

[78] M. M. Kim, Y. Huang, K. Choi, and C. H. Hidrovo, "The improved resistance of PDMS to pressure-induced deformation and chemical solvent swelling for microfluidic devices," *Microelectronic Engineering,* vol. 124, pp. 66-75, 2014/07/25/ 2014, doi: https://doi.org/10.1016/j.mee.2014.04.041.

[79] R. Dangla, F. Gallaire, and C. N. Baroud, "Microchannel deformations due to solvent-induced PDMS swelling," *Lab on a Chip,* 10.1039/C003504A vol. 10, no. 21, pp. 2972-2978, 2010, doi: 10.1039/C003504A.

[80] J. N. Lee, C. Park, and G. M. Whitesides, "Solvent compatibility of poly(dimethylsiloxane)-based microfluidic devices," *Analytical Chemistry,* vol. 75, no. 23, pp. 6544-6554, 2003/12/01 2003, doi: 10.1021/ac0346712.

[81] "Waveform Amplifier." [Online]. Available: https://accelinstruments.com/Applications/TS200/Waveform-Amplifier.html.

[82] R. J. Adrian and J. Westerweel, *Particle image velocimetry* (Cambridge aerospace series; 30). Cambridge: Cambridge University Press (in English), 2011.

[83] M. Raffel, C. E. Willert, F. Scarano, C. J. Kähler, S. T. Wereley, and J. r. Kompenhans, *Particle image velocimetry : a practical guide*, Third edition ed. Cham: Springer, 2018. [Online]. Available: https://search.ebscohost.com/login.aspx?direct=true&scope=site&db=nlebk&db=nlabk&AN=1770331.

[84] G. Di Labbio, "On left ventricular fluid dynamics associated with progressive chronic aortic regurgitation," PhD. Thesis, Concordia University, 2019. [Online]. Available: https://spectrum.library.concordia.ca/id/eprint/985895/

[85] B. E. A. Saleh and M. C. Teich, *Fundamentals of photonics*, Third edition ed. Hoboken, NJ: Wiley, 2019. [Online]. Available: https://search.ebscohost.com/login.aspx?direct=true&scope=site&db=nlebk&db=nlabk&AN=2037047.

[86] W. Thielicke and R. Sonntag, "Particle Image Velocimetry for MATLAB: Accuracy and enhanced algorithms in PIVlab," *Journal of Open Research Software,* 2021, doi: 10.5334/jors.334.

[87] W. Thielicke and E. J. Stamhuis, "PIVlab – Towards user-friendly, affordable and accurate digital particle image velocimetry in MATLAB," *Journal of Open Research Software,* 2014, doi: 10.5334/jors.bl.

[88] H. Kim and J. Bae, "Analysis of electrical resistance changes in liquid metal printed wires under strain for stretchable electronics," *Smart Materials and Structures,* vol. 30, no. 9, p. 095004, 2021/07/29 2021, doi: 10.1088/1361-665X/ac1562.

[89] T. Sato, K. Yamagishi, M. Hashimoto, and E. Iwase, "Method to reduce the contact resistivity between Galinstan and a Copper electrode for electrical connection in flexible devices," *ACS Applied Materials & Interfaces,* vol. 13, no. 15, pp. 18247-18254, 2021/04/21 2021, doi: 10.1021/acsami.1c00431.

[90] "Electric Generators and Back Emf," 2025/3/2/. [Online]. Available: https://phys.libretexts.org/@go/page/4433.

[91] M. D. Dickey, R. C. Chiechi, R. J. Larsen, E. A. Weiss, D. A. Weitz, and G. M. Whitesides, "Eutectic Gallium-Indium (EGaIn): a liquid metal alloy for the formation of stable structures in microchannels at room temperature," *Advanced Functional Materials,* vol. 18, no. 7, pp. 1097-1104, 2008/04/11 2008, doi: https://doi.org/10.1002/adfm.200701216.

[92] M. A. Eddings, M. A. Johnson, and B. K. Gale, "Determining the optimal PDMS–PDMS bonding technique for microfluidic devices," *Journal of Micromechanics and Microengineering,* vol. 18, no. 6, p. 067001, 2008/04/25 2008, doi: 10.1088/0960-1317/18/6/067001.

[93] D. Floryan, T. Van Buren, and A. J. Smits, "Swimmers' wake structures are not reliable indicators of swimming performance," *Bioinspiration & Biomimetics,* vol. 15, no. 2, p. 024001, 2020/02/24 2020, doi: 10.1088/1748-3190/ab6fb9.

[94] G. Gomit, L. Chatellier, and L. David, "Free-surface flow measurements by non-intrusive methods: a survey," *Experiments in Fluids,* vol. 63, no. 6, p. 94, 2022/05/26 2022, doi: 10.1007/s00348-022-03450-5.

APPENDIX

A1 Permanent Magnet Characterization

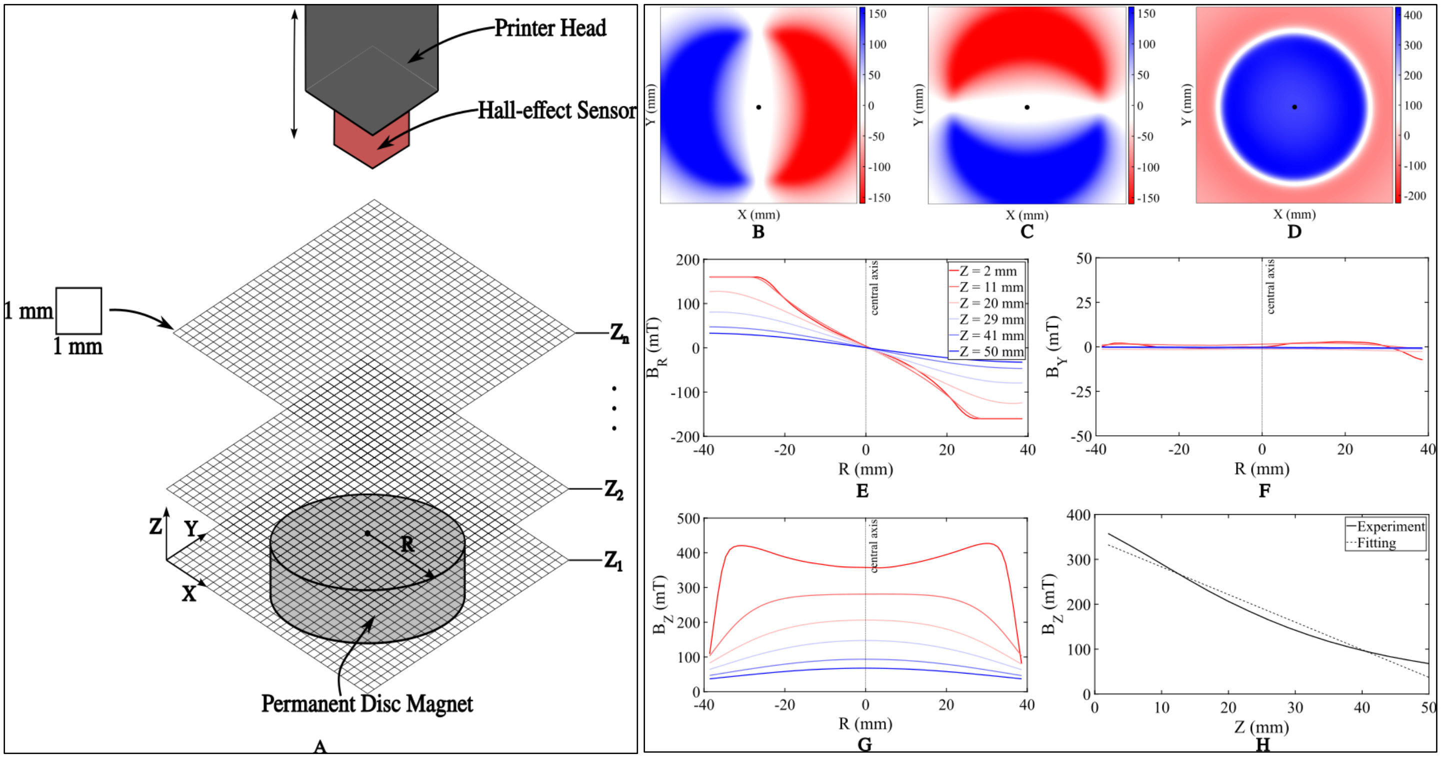

Figure A 1.1 Permanent (NdFeB) disc magnet characterization. The experimental procedure is depicted in A. and the findings are summarized in B. to H.

A Hall-effect sensor records the magnetic field strengths (B_X, B_Y, B_Z) which is attached to a 3D printer head travelling in a predefined, 2D grid (X, Y) for every height location $(Z = 2 - 110\ mm, \Delta Z = 3mm)$. Cartesian reference frames and magnet dimensions are used to establish sign conventions. Colormaps of B. B_X, C. B_Y and D. B_Z at $Z = 2\ mm$ show the distribution of magnetic field strengths in milliTesla (mT) in the XY-plane. The black marker represents the magnet's center. Magnetic field strength plots at increasing Z locations are shown relative to the magnet's radius (R) for E. B_R, F. B_Y and G. B_Z. Plot H shows the relationship of B_Z and Z for the measurements and a linear approximation $(B_Z(Z) = -6.15Z + 334.64)$ at magnet's center $(R = 0)$.

A2 3D Printing Settings and Dimensions of SEMA Channels

Table A 2.1 Custom 3D printing settings used to fabricate SEMA channels on FDM printer using Ultimaker Cura slicing software (v. 4.6.1). All other printing settings were left at the default or calculated values implemented by Cura.

Printing Material	ABS (1.75-mm dia)
Printing Temperature	250°C
Bed Temperature	90°C
Flow	95%
Line Width (= Nozzle Size)	0.25 mm
Layer Height	0.1 mm
Initial Layer Height	0.2 mm
Infill Density	50%
Fan Speed	10%
Support Type	Tree
Support Placement	Buildplate
Support Density	10%
Support Top Distance	0.3 mm
Overhanging Wall Speed	40%
Bridge Fan Speed	50%

Table A 2.2 (*CE = Channel Extension) Dimensions of horizontal segments and other design details of the SEMA channels extracted from CAD software (Solidworks 2023).

Segment	Height (H) [mm]	Length (L) [mm]	Current Polarity
1	3.75	26.00	-
*CE	5.63	6.50	-
2	7.50	31.75	-
3	11.25	24.25	-
4	14.00	16.75	-
5	16.75	9.25	-
6	19.50	1.50	-
7	22.25	5.50	+
8	25.00	13.00	+
9	27.75	20.50	+
10	30.50	28.00	+
11	33.25	35.50	+

A3 Estimation of Lorentz Forces

Table A 3.1 Estimation of magnitudes of Lorentz forces for SEMA actuation currents (I) based on linear approximation of resultant magnetic field strength ($B = B_Z$).

Actuation Current (A)	Magnitude of Lorentz Force (N)
1	0.005
2	0.010
3	0.014

A4 Arduino Pseudocode

SEMA_HBRIDGE_DRIVER.ino

```
BEGIN PROGRAM
IMPORT Cytron Motor Driver library functions from header file
CALL CytronMD motor(SET motor_type to PWM_DIR, SET DIO_pin_PWM to pin 3, SET DIO_pin_motor_direction to pin 2)
CALL routine void setup()
     INIT baud rate for serial data communication equal to 115200 Bd
END routine setup()
     CALL routine void loop()
     WHILE loop is always TRUE
     SET motor speed value to 65 for control of pwm duty cycle (+I)
     MAINTAIN previous command for 500 ms equal to half of actuator signal’s period
     SET motor speed value to -65 for control of pwm duty cycle (-I)
     MAINTAIN previous command for 500 ms equal to other half of actuator signal’s period
END routine loop()
END PROGRAM
```

Figure A 4.1 Pseudocode outlining program on Arduino UNO for Cytron H-Bridge motor driver in the control system when $I = 1\ A$ and $f = 1\ Hz$.